



HAL
open science

Contribution to the development of an experimental device based on a robotic platform for gait rehabilitation

Houssein Lamine

► To cite this version:

Houssein Lamine. Contribution to the development of an experimental device based on a robotic platform for gait rehabilitation. Biomechanics [physics.med-ph]. Ecole Nationale d'Ingénieurs de Monastir (Tunisie), 2016. English. NNT: . tel-02496096

HAL Id: tel-02496096

<https://hal.science/tel-02496096>

Submitted on 2 Mar 2020

HAL is a multi-disciplinary open access archive for the deposit and dissemination of scientific research documents, whether they are published or not. The documents may come from teaching and research institutions in France or abroad, or from public or private research centers.

L'archive ouverte pluridisciplinaire **HAL**, est destinée au dépôt et à la diffusion de documents scientifiques de niveau recherche, publiés ou non, émanant des établissements d'enseignement et de recherche français ou étrangers, des laboratoires publics ou privés.



**Contribution au développement d'une plate-forme robotisée
pour le contrôle et la Rééducation Fonctionnelle de la marche
humaine**

**Contribution to the development of an experimental device
based on a robotic platform for gait rehabilitation**

Thèse présentée en vue de l'obtention du diplôme de doctorat

Spécialité : **Génie Mécanique**

Présentée par: **Houssein LAMINE**

Soutenu le 23 /07/2016, devant le jury composé de:

M. Mnaouar CHOUCANE	Professeur, ENIM	Président
M. Mohamed HADDAR	Professeur, ENIS	Rapporteur
M. Zouhaier AFFI	Maitre de Conférences, ENIM	Rapporteur
M. Abdelfattah MLIKA	Maitre de Conférences, ENISo	Examineur
M. Lotfi ROMDHANE	Professeur, ENISo	Directeur de Thèse

Laboratoire de Mécanique de Sousse – INRIA Sophia Antipolis–Institut Pprime



Content

Content	1
Acknowledgement.....	3
Publications	4
Abbreviations	5
Abstract	6
1. Introduction	10
Summary:	10
1.1. Introduction to Gait Disorders.....	10
1.2. Biomechanical Background	11
1.2.1. Human movements.....	11
1.2.2. Anatomy of the lower limb	12
1.3. Understanding Spinal Cord Injury and Stroke	14
1.3.1. The nervous system.....	14
1.3.2. SCI and stroke pathologies.....	17
1.4. Gait Rehabilitation	19
1.4.1. Rehabilitation after a neural injury	19
1.4.2. Therapist-assisted rehabilitation of walking	20
1.4.3. Robotic-assisted rehabilitation of walking.....	22
1.4.4. Cable based system for gait rehabilitation	28
1.5. Design of the Cable-Based Gait Rehabilitation Machine	31
Conclusion:.....	34
2. Analysis of Human Walking	36
Summary:	36
2.1. Overview of Normal Walking.....	36
2.1.1. The Stance Phase.....	37
2.1.2. The Swing Phase	38
2.1.3. Gait parameters	39
2.1.4. Lower extremity angles.....	39
2.2. Quantitative Gait Analysis	40
2.2.1. Experimental setup.....	40
2.2.2. Data analysis	42
Conclusion:.....	48
3. Inverse Dynamic Simulation of the Rehabilitation Machine	50
Summary:	50
3.1. Dynamic Modeling.....	50
3.1.1. Human body modeling.....	50
3.1.2. Inertias and geometry of the different segments	52
3.1.3. Free-body diagram and Newton-Euler equations	53
3.2. Inverse Dynamic Simulation	56
3.2.1. Solving the Newton-Euler equations	56
3.2.2. SimMechanics dynamic simulation	57
3.3. Case Study.....	58
Conclusion:.....	62
4. Design of Cable-Driven Parallel Manipulators	64
Summary:	64
4.1. Workspace Analysis of Cable-Driven Parallel Manipulators	65

4.1.1. Tension condition and wrench feasibility	68
4.1.2. Cable interference	69
4.2. Introduction to Interval Analysis.....	70
4.2.1. Overview	70
4.2.2. Interval mathematic.....	71
4.3. Interval-Analysis-Based Design of CDPMs	75
4.3.1. Interval form of the equilibrium.....	76
4.3.2. Wrench Feasibility of the equilibrium	78
4.3.3. Design algorithm of CDPMs.....	80
4.4. Applications to the Design of CDPMs	82
4.4.1. Case 1: a planar CDPM.....	82
4.4.2. Case 2: a Spatial CDPM.....	83
4.4.3. Impact of overestimation problem on the design of CDPMs.....	85
Conclusion:.....	87
5. Design of the CDLT Rehabilitation Machine	90
Summary:	90
5.1. Design of the CDLM.....	90
5.1.1. Design requirements.....	91
5.1.2. Generation of optimal design parameters	94
5.1.3. Curves of simulated power requirements.....	97
5.2. Actuation Parts Selection of the CDLT.....	100
5.2.1. Actuators of the CDLM	100
5.2.2. Actuators of the BWSD	102
5.3. Presentation of the CAD Design of the CDLT	103
Conclusion:.....	105
6. Discussion and Concluding Remarks.....	106
6.1. Gait Experiment and Walking Data	106
6.2. Dynamic Simulation of Treadmill Walking.....	107
6.3. Design of CDMPs Using Interval Analysis	108
6.4. Design of the CDLT.....	109
6.5. Future Scope.....	109
Appendices	111
Appendix 1: Anthropometric data [127]	111
Appendix 2: dynamic and kinematic data	112
Appendix 3: Robot equilibrium equations	115
Appendix 4: Technical data.....	117
References	129
List of Figures	143
List of Tables.....	145

Acknowledgement

Firstly, I would like to express my sincere thanks to my advisor, Pr. Lotfi Romdhane, for his guidance, patience and encouragement. I am very grateful for his help in writing the papers and this manuscript. This work would not be finished without his support. Besides my advisor, I would like to thank Dr. Sami Bennour and Dr. Med Amine Laribi for their support and help.

My sincere thanks also go to Pr. Said Zaghoul who provided me an opportunity to join his team (ROBOISS team, Institut Pprime, France) in order to carry the gait experiment. Also, I thank Dr. Jean-Pierre Merlet for allowing me to join his team (HEPHAISTOS team, INRIA Sophia Antipolis, France). During this short stay I investigated the analysis of cables robots.

I would also like to thank, in advance, all the members of the committee for accepting to evaluate this PhD dissertation.

My thanks go to all of my colleagues of the Mechanical Laboratory of Sousse, for the sleepless nights before deadlines, and for all the fun we have had. Also, I thank the members of ROBOISS and HEPHAISTOS teams.

Last but not the least, I would like to thank my family: my parents and my brothers and sisters. I'm very grateful to my mother for supporting me spiritually throughout this thesis.

Publications

Journals papers

- [1] H. Lamine, S. Bennour, and L. Romdhane, “Design of cable-driven parallel manipulators for a specific workspace using interval analysis,” *Adv. Robot.*, vol. 30, no. 9, pp. 585–594, 2016.
- [2] H. Lamine, M. A. Laribi, S. Bennour, L. Romdhane, and S. Zaghoul, “Design study of a Cable-Based Gait Training Machine,” *Submitted*, 2016.

Conferences

- [3] H. Lamine, S. Bennour, and L. Romdhane, “Dynamic Simulation of a Cable-Based Gait Training Machine,” in *Robotics and Mechatronics*, Springer, 2016, pp. 199–207.
- [4] H. Lamine, S. Bennour, and L. Romdhane, “Design of cable driven robots for a desired workspace,” in *Conception et Modélisation des Systèmes Mécaniques*, 2015, p. 2. Hammamet, Tunisia.
- [5] H. Lamine, S. Bennour, J.-P. Merlet, and L. Romdhane, “Workspace evaluation for a cable based gait trainer robot,” in *Tunisian Congress on Mechanics*, 2014, p. 2. Sousse, Tunisia.
- [6] H. Lamine, M. A. Laribi, L. Romdhane, and S. Zaghoul, “Evaluation Of The Kinect Skeleton Tracking Performance Using A VICON Motion Capture System,” in *Conception et Modélisation des Systèmes Mécaniques*, 2013, p. 8. Djerba, Tunisia.

Abbreviations

AJC= Ankle Joint Center

BWS = Body Weight Support

BWSD= Body Weight Support Device

BWSTT = Body weight Support Treadmill Training

CAD= Computed-Aided Design

CDLM=Cable-Driven Leg Manipulator

CDLT= Cable-Driven Leg Trainer

CDPM= Cable-Driven Parallel Manipulator

CoG= Center of Gravity

CoM= Center of Mass

CoP= Center of Pressure

CoR= Center of Rotation

CVA =CerebroVascular Accident

DOF= Degree of Freedom

FCW = Force Closed Workspace

GC = Gait Cycle

NS= Nervous System

Rap=anterior-posterior Reaction

RoM=Range of Motion

rpm= revolute per minute

Rv =vertical Reaction

SCI = Spinal Cord Injury

TIA =Transient Ischemic Attack

WFW=Wrench-Feasible Workspace

Abstract

The presented work in this manuscript focuses on the development of a gait training machine based on a Cable-Driven Parallel Manipulator (CDPM) to move the legs and a Body Weight Support Device to suspend the body. Mainly, this research is focused on the design of the cable robot.

Persons attained by neurological injuries such as Spinal Cord Injury and Stroke, may lose their motor functions including the ability to walk. These injured patients can relearn walking through intense and task-oriented rehabilitation therapy, which consists in simulating the gait movement. Walking is the most crucial locomotion activity and is essential for daily life activities. Therefore, the first preoccupation of injured patients is the recovery of the gait function. Therapist-assisted gait training is physically demanding, thus we are limited by the performance of the rehabilitation assistants. In this context, robotic-based gait training machines overcome these constraints, alleviate the high workload of therapists and offer a long duration of rehabilitation. By relying on robotic-based training devices, improvement in locomotion recovery could be potentially enhanced.

Several complex robotized machines have been developed. Based on rigid links, market available gait trainers are heavy, bulky and expensive. In our case we are investigating a machine based on a cable robot. Such robots are well known for their lightweight structure, reconfigurability and low cost, and they can be an alternative to the existing machines. The proposed training machine is called Cable-Driven Leg Trainer (CDLT) and its design can be described as follows: On the one hand, the patient is kept in an upright position through the use of a Body Weight Support Device (BWSD). It is made out of an elastic spring allowing to select the unloading percentage of the patient's weight by setting the spring pretension. On the other hand, the posture of the lower limb is controlled by a cable robot called the Cable-Driven Leg Manipulator (CDLM). In fact, the end-effector of this robot consists of an orthosis, placed on the patient's leg, in the aim of reproducing a natural gait pattern. Further, a treadmill helps keeping the pace of the walking motion.

The main function of the rehabilitation machine is to simulate the gait walking by producing the kinematics of a normal gait. Consequently, a good understanding of the gait pattern is of utmost importance. A gait analysis is carried out using an optical motion capture system and a force platform. Details of the experimental setup and the protocol including markers placement and type of motions are provided. Further, data analysis methods such as

identification algorithm of joint centers and angle definitions are given. Thereby, the kinematics and dynamics of a normal gait are measured and then normalized, which will be employed to achieve a dynamic simulation of walking.

Thereafter, an inverse dynamic study of a body weight support treadmill walking is investigated. The target motion is the recorded kinematics and the output information is the required actuation wrench to be generated by the CDLM to drive the lower limb during ambulation. The human body is modeled as a multi-segment articulated mechanism. The addressed free-body diagram shows all exerting forces for each segment. The external forces on the human body are the unloading force and the ground reaction force. The dynamic model is simulated using two methods: the first one is the Newton-Euler formulation, and the second one is using Matlab SimMechanics toolbox. The two methods yielded similar results concerning the actuation wrench. The obtained results are used in the design of the CDLM through the calculation of the required external wrench of the CDLM and the cable tensions.

The rehabilitation machine is based on a cable-driven parallel manipulator (CDPM). The design of this CDPM is one of our main objectives. The design problem can be state as follows: given a prescribed workspace and a required external wrench, find the geometric parameters that ensure non-negative tensions in all the cables over all the desired workspace. An approach based on interval analysis is developed to solve this problem. Interval analysis is a method used to provide a reliable computing method when working with inaccurate and inexact data. Such uncertainties can be caused by mathematical rounding errors and manufacturing errors. In the context of designing CDPMs the workspace is discretized in a set of poses. However, the interval method examines the workspace as an entire range of poses.

The dynamic equilibrium of a CDPM is a linear set of equations. A pose is said to be wrench-feasible when the unknown cable tensions are in specific and non-negative ranges. Using interval analysis method, the equilibrium is written in its interval form. Then, by means of a strong feasibility theorem, its wrench-feasibility is checked by solving a finite number of classical linear set of equations.

The proposed algorithm receives as inputs: the desired workspace, the external wrench, a set of design parameters, their ranges and their discretization steps. Consequently, all possible designs of a CDPM's structure are generated. Wrench-feasibility of each one is checked for the specified workspace and with respect to the given external loads. Thereby, all feasible designs are found and saved. The best solution is selected according to a design criterion, to be specified by the user. The algorithm is illustrated by designing a planar and a spatial CDPMs. Based on

the list of all possible designs, feasible ones are found successfully and the optimal one is selected.

Based on a case study, it is observed that a solution may be overestimated if the required workspace is defined by a large grid size. This problem is known in interval analysis as dependence and wrapping effects. Bisectioning intervals into smaller ones can lessen the effect of overestimation. However, large computation time is required in this case.

Unlike discrete methods, where only a finite number of poses is examined, interval analysis method processes all the desired space for the wrench-feasibility. Thus, the major advantage of the developed algorithm is that it guarantees that all the desired space is free from singularities.

Lastly in this work, a design study of the CDLT is carried out. All the aforementioned findings are collected to get the optimal design parameters of the CDLM. Indeed, the gait kinematics and the dynamic simulation are used to calculate, respectively, the required workspace and the wrenches to be produced by the CDLM. Then, the algorithm of CDPMs design is used to calculate all feasible designs based on a specific search ranges of the design variables. Relying on a tensegrity analysis, an optimal design is selected. Power requirements for the cables are then computed and the specifications of actuators are determined. Moreover, actuation mechanisms included in the BWSD are also selected. Finally, a CAD model of the gait training machine is presented.

The organization of this manuscript is as follows. Chapter 1 gives an introduction to the context of gait training and the biomechanics of the lower limb. In addition, a review of rehabilitation methods and gait training machines is presented. This chapter ends with a description of the proposed rehabilitation machine.

Chapter 2 begins by describing the pattern of a normal walking cycle. Then, an experimental protocol and data processing steps of the quantitative gait analysis are provided. The required gait kinematic and dynamic data are obtained, which is then used as an input for the dynamic simulation of the CDLT.

In Chapter 3, the previous results, including angular trajectories of the hip, knee and ankle joints in addition to the measured ground reaction, are used to derive an inverse dynamic simulation. Initially, human body modelling, inertia data and length specifications are provided. Then, the dynamic simulation is carried out by solving dynamic equations and through a Matlab SimMechanics model. Finally, the obtained actuation wrenches are presented.

Chapter 4 focuses on giving an approach based on interval analysis to design a CDPM for a desired workspace and a specific external wrench. First, the analysis of the workspace of

the CDPMs is introduced, then an overview of the interval analysis method is presented. The wrench-feasibility of a CDPM's equilibrium in its interval form is discussed, and the design algorithm is described. Lastly, the algorithm is illustrated through two different designs of a cable robot.

In Chapter 5, we address the design of the CDLT machine based on the results of the previous chapters. Then, the actuation mechanisms of the CDLM and the BWSD are calculated and selected. This chapter ends by presenting the CAD model of the gait trainer.

A final chapter summarizes the main results obtained in this work.

1. Introduction

Summary:

In this first chapter, a presentation of the required background for gait disorders, fundamentals of human movements and the anatomy of the lower limb are given. Then, we provide a description of the anatomy and physiology of the nervous system. Major causes of functional impairment such as gait disorders are spinal cord injury and stroke. These pathologies affect directly the functioning of the nervous system. After an injury, gait training is essential for the injured person to restore the gait function. An overview of different rehabilitation protocols is given. Then, a review on the development of the existing walking rehabilitation machines is addressed and a classification of these machines is performed. Amongst various devices, we adopt an architecture based on a cable robot

1.1. Introduction to Gait Disorders

In the everyday activities, walking is the most vital action to satisfy the well-being of a person. Loosing this function, decreases the quality of life, rises the dependence on others and puts individuals at a risk of falls and injuries. Frequently, neurological injuries lead to a partial paralysis that causes walking deficits, hence injured persons will suffer from long-life locomotion impairments.

Worldwide, Spinal Cord Injury (SCI) and Stroke neurological injuries are major causes for disability [1][2][3]. From 1950 to 2012, the global incidence of SCI varied from 8 to 246 cases per million population per year [4]. In the United States, the reported rate is about 40 cases and in European countries the incidence varied from 13.9 to 19.4 per million [5]. Likewise, stroke has an important impact, approximately every 40 seconds a stroke occurs in the United States and the reported annual rate is 795 000 incidents [6]. In the UK, the estimated rate is around 150 000 strokes occurring every year [3]. Worldwide, the prevalence, i.e., the cumulative number of strokes, was 33 million in 2010 [7]. In addition to SCI and Stroke pathologies, ambulation disability can be caused by non-traumatic injuries, i.e., neurological diseases such as Parkinson's disease [8], multiple sclerosis and cerebral palsy [9].

It is thought that task-oriented, intensive and repetitive therapy have benefits in regaining walking ability [1][10] and hence enhance the patient's quality of life [11][12]. The first goal of disabled patients is the rehabilitation of walking, specifically early gait rehabilitation is fundamental for a faster and efficient locomotion recovery [13][14]. Conversely, immobility during hospitalization promotes the risk of mortality and encourages

impairments [15] in addition to other side effects such as bone acceleration, sensory deprivation, isolation delirium and incontinence [16].

1.2. Biomechanical Background

1.2.1. Human movements

Motions of body segments can be described using a set of planes and directions defined relatively to the human body taken in standing position (see Figure 1). The planes are three: the frontal, the transverse and the sagittal planes. The frontal (coronal) plane is positioned vertically and it divides the body in anterior and posterior parts. The transverse (horizontal) plane lies horizontally and splits the body into inferior and superior portions. The sagittal planes are situated vertically, dividing the body into right and left sides. The midsagittal plane is positioned at the midline of the body and the parasagittal plane is a midsagittal parallel plane [17][18][19]. Moreover, standard directions are described by the following paired terms: superior/inferior, anterior/posterior (ventral/dorsal) and left/right (medial/lateral) (see Figure 1).

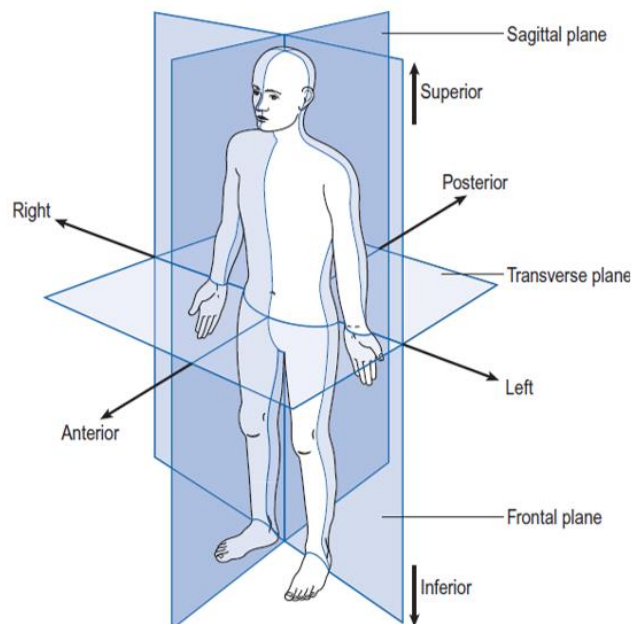


Figure 1: Planes of the human body [20].

The human body is characterized with a set of articulated segments, each segment has a proximal and a distal ends, which are, respectively, the closest and the farthest points to the segment's attachment point. Body parts are articulated to form joints rotational motions are classified according to the axis of rotation that passes through the articulation's center. The most common angular movements are: flexion/extension, abduction/adduction and internal/external rotations [17][18][19].

The flexion/extension are the movements that take place in the sagittal plane. Flexion occurs when bringing two segments closer to each other or when a limb moves forward (along

the anterior axis) and extension is the rotation in the opposite direction of flexion. Moving a joint backward beyond its normal range is called hyperextension (see Figure 2(a, b)).

Abduction/adduction are the movements of a segment in the frontal plane. Abduction is the motion when a part goes away from the body midline superior/inferior direction. Conversely, Adduction is defined when bringing two segments together (see Figure 2(c, d)).

Internal/external (medial/lateral) rotations occur when a segment revolves around its own longitudinal axis. Internal rotation is the movement when turning toward whereas external rotation is when turning away (see Figure 2(e)).

Yet, there are special movements that have specific names and occur only at certain joints, such as dorsiflexion/plantar flexion and inversion/eversion of the foot (see Figure 2(f)).

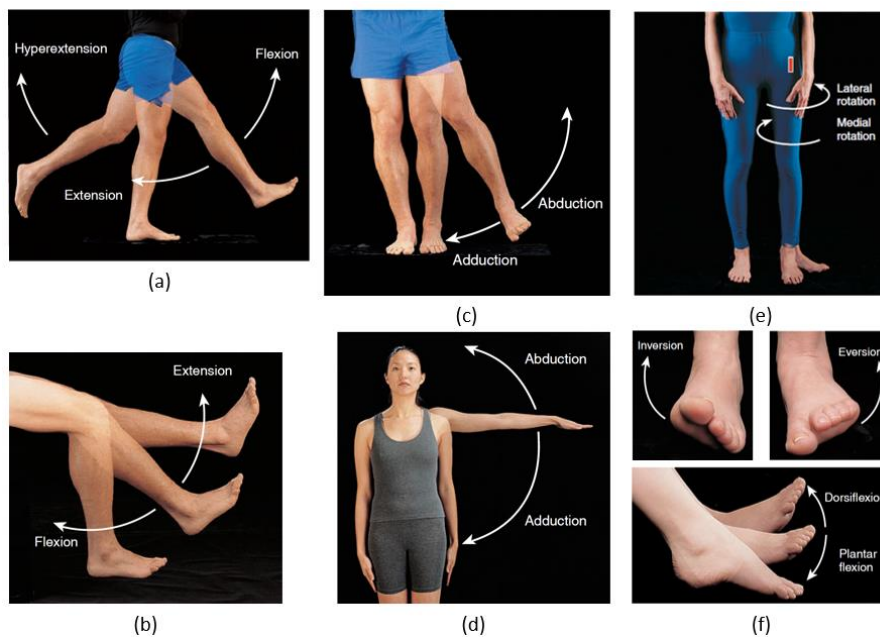


Figure 2: Types of angular movements [18][19].

1.2.2. Anatomy of the lower limb

The lower limb is the biomechanical mechanism that have two main functions: support of body weight and locomotion. It is composed of four main segments: the pelvis, the thigh, the leg and the foot (see Figure 3). Note, the leg is commonly known as the shank or the calf. The lower limb is a weight bearing system, then its bones are stronger than other bones of the skeleton system. Furthermore, its skeleton contains 31 bones per limb. The pelvis is formed of two hip bones called also coxals. The unique bone of the thigh is the femur which is the longest and strongest bone of the skeleton system. The leg contains two bones: the fibula and the tibia. Bones of the foot are in three rows: a first row of 7 tarsals, a second row of 5 metatarsals and a third row of 14 phalanges [21]. The forefoot consists of metatarsals and phalanges [21].

In anatomical terminology, while the superior face of the foot is called dorsum, the inferior face is named sole of the foot. Moreover, the posterior and the anterior parts of the foot are called, respectively, the heel and the toe [21].

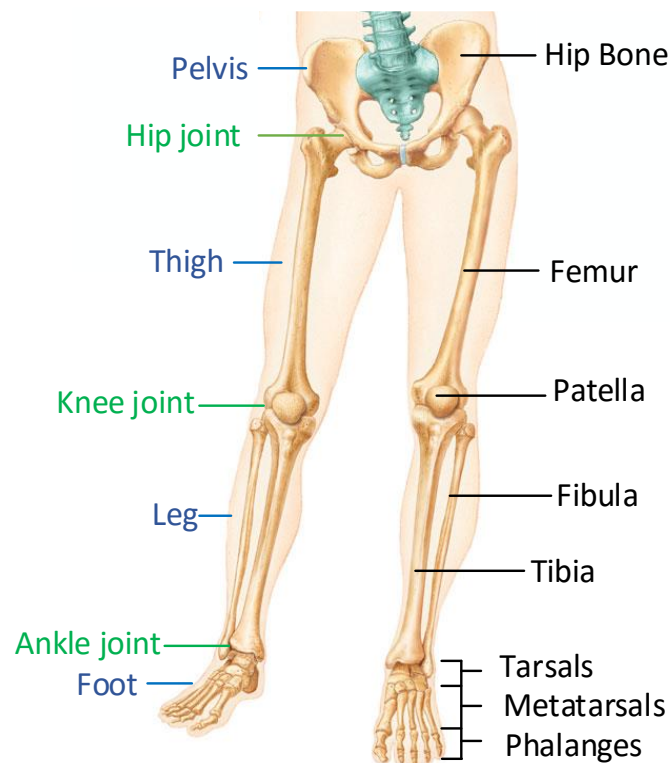


Figure 3: Anatomy of the lower limb [18].

Sites where skeleton rigid links meet each other are called joints or articulations. Several types of joints can be they are. Functionally, articulations of the lower extremities are classified as freely movable (diarthrosis), and structurally, they are known as synovial joints. Indeed, they contain a fluid-filled cavity, and ends of the bones are covered with an articular cartilage. The joint cavity is enclosed with two layers: a synovial member and a fibrous capsule. The fluid and the cartilage lubricate these freely movable joints [19].

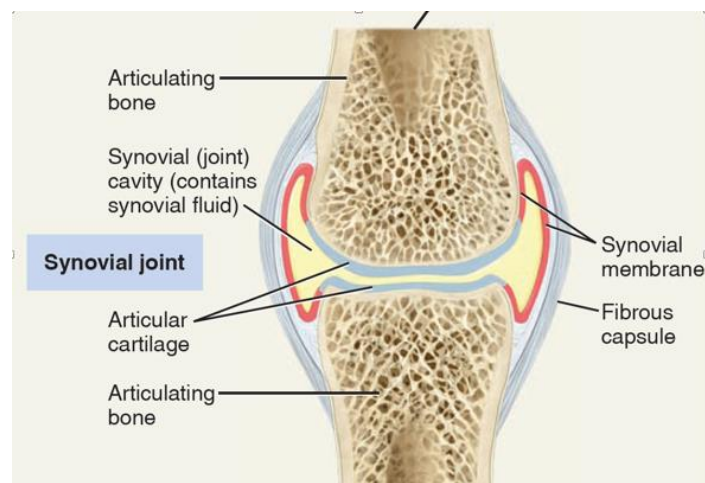


Figure 4: A typical synovial joint (the knee joint) [19].

The lower extremity includes 4 synovial joints: the hip, the knee, the ankle and the foot [21]. The hip joint is a ball and socket type of synovial joint formed by the acetabulum of the hip and the spherical head of the femur. The hip joint is a spherical joint then rotational movements occur in all axes. Figure 2(a), Figure 2(c) and Figure 2(e) show, respectively, Flexion/Extension, Abduction/Adduction and Medial/Lateral motions of the hip joint.

The knee joint is the most complex joint in the body, it is a modified hinge variety of a synovial joints. The knee includes surfaces of 4 bones: the femur, the tibia, the fibula and the patella. The patella bone (or knee cap) is placed in front of the joint (see Figure 3). The major occurring movement is the flexion/extension (see Figure 2(b)), but some medial/lateral rotations are permitted [18].

The ankle joint is a strong weight-bearing hinge joint. The inferior ends of the tibia and the fibula, and the talus of the foot meet to form this articulation. The only possible motion is the Dorsiflexion/ Plantar flexion (see Figure 2(f)).

In addition to all above joints, the various bones of the foot include numerous joints. Such articulations include intratarsal, tarsometatarsal, intermetatarsal, metatarsophalangeal, and interphalangeal joints [21]. For example, the intratarsal joint allows the Inversion/Eversion movement of the foot (Figure 2(f)).

1.3. Understanding Spinal Cord Injury and Stroke

1.3.1. The nervous system

An understanding of the anatomy and physiology of the nervous system (NS) is substantial to explain SCI and Stroke, since these neurological injuries affect directly the functioning of the NS.

Human body motions are controlled by the NS which have 2 parts: the Central Nervous System (CNS) and the Peripheral Nervous System (PNS) (see Figure 5) [19]. The CNS includes the brain and the spinal cord, and the PNS comprises nerves that extend from the brain and the spinal cord, i.e., located outside the CNS. The spinal cord and nerves consist of pathways to transmit information as an electrical signal between the brain and the sensory receptors/effector organs. Neuron or nerve cell is the basic structural unit of the NS. Further, a neuron is a cell that transmit information as electrical impulses between body parts [19].

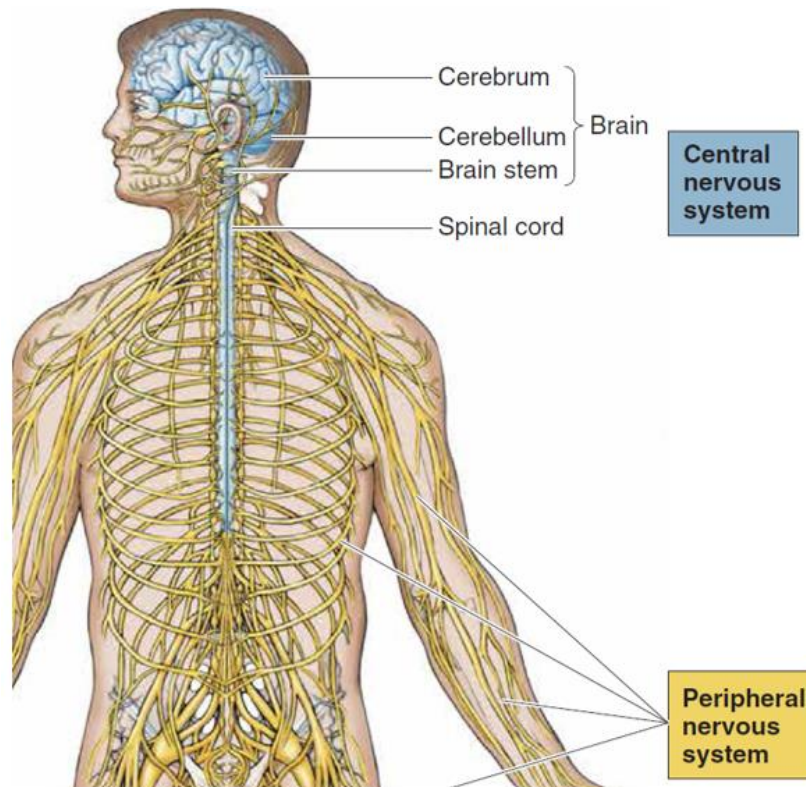


Figure 5: Main divisions of the nervous system [22].

The brain is located in the skull and has 4 parts: cerebrum, cerebellum, diencephalon and brain stem (see Figure 6) [19]. The cerebrum is the biggest part of the brain (83% of total brain mass) and is made up of two communicating hemispheres. Functionally, this part controls all sensory and motor functions, thought processes and memories. The left cerebral hemisphere is concerned with sensory/motor functions of the right side of the body and vice versa. Similarly to the cerebrum, the cerebellum has two hemispheres. Functionally, it initiates subconscious movements like walking and coordinates muscle movements of the human body, and hence helps in controlling posture and equilibrium. The diencephalon consists of a relay station that dispatches sensory/motor pathways to and from the brain. In addition, it has an area that controls: various vital functions (e.g. eating, drinking and temperature regulation), endocrine system and autonomic functions. The brain stem is a connection with the spinal cord and it controls: the movements of the neck and the head through cranial innervation and involuntary functions necessary for surviving like breathing and heart rate regulation. In summary, the brain has different identifiable regions [22], each one has a specific function (see Figure 7). An injury that may happen to the brain can disturb sensations, movements and thoughts, and even can cause death [22].

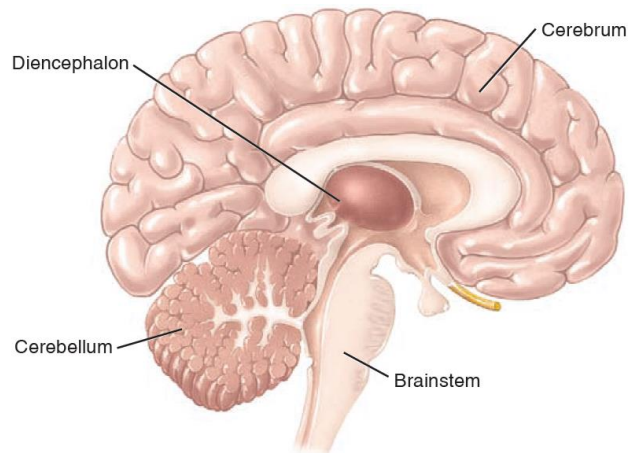


Figure 6: The brain and its main parts [19].

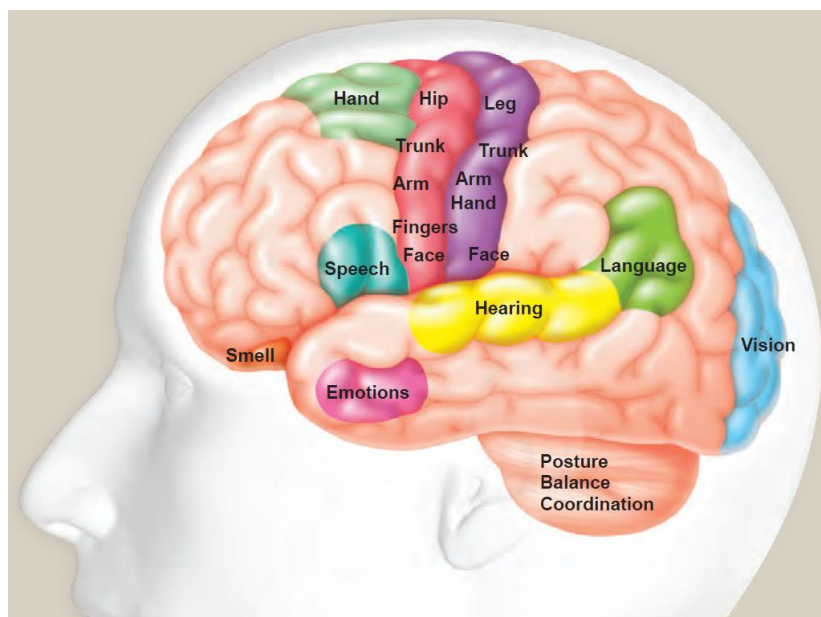


Figure 7: Main functions of the different areas of the brain [23].

The second part of the CNS is the spinal cord which lies within the vertebral column, it consists of a bidirectional pathway between the brain and the peripheries (i.e. skin, joints and muscles) of the human body via spinal nerves, which are part of the PNS. The spinal cord innervates the neck, limbs and trunk through 31 pairs of spinal nerves roots, they are divided into 5 regions: cervical, thoracic, lumbar and coccygeal. Each group of spinal nerves has a specific destination to a periphery, Figure 8 depicts the locations and the functions associated with spinal nerves, e.g. the movements of the lower limb are controlled through the L1-S1 innervations. Incoming sensed information is sent to the brain through ascending tracts (i.e. nerves), and outgoing motor information is carried to periphery via descending tracts [19]. Furthermore, the spinal cord acts as a reflex center, i.e., produces involuntary responses.

Transection of the spinal cord result in a permanent loss of sensation and paralysis of voluntary movements [18].

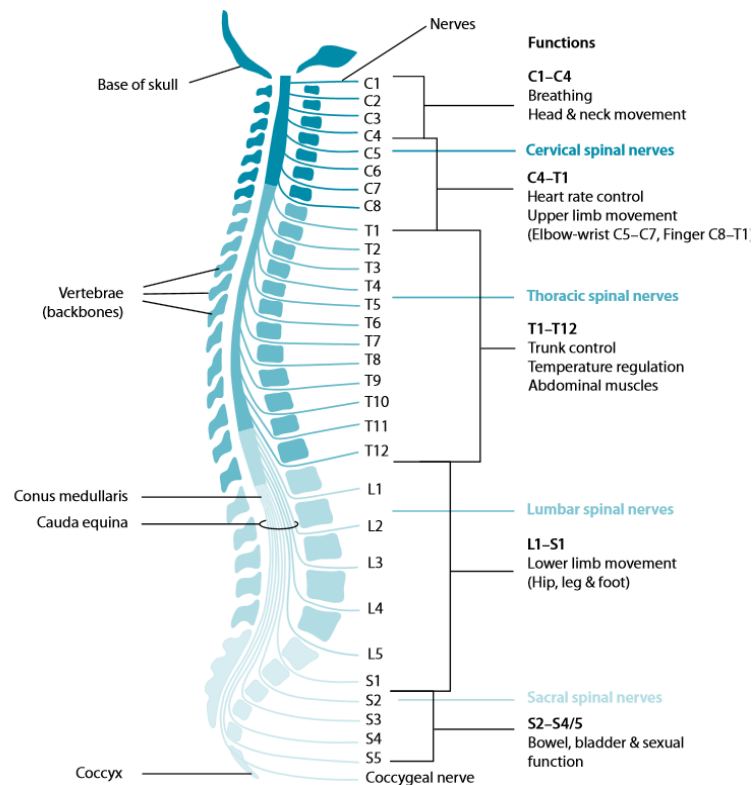


Figure 8: The spinal cord [24].

The PNS includes the parts of the NS that lies outside the brain and the spinal cord, i.e., the CNS. More precisely, the PNS consists mainly of both: cranial nerves and spinal nerves, i.e., nerves that extend from the brain and the spinal cord, respectively [18]. These nerves are the communication pathways between the peripheries and the CNS. The peripheries include sensory or afferent nerve receptors such as receptors found in the skin, joints and muscles, and motor or efferent motor nerves such as skeletal muscles and glands.

To sum up the physiology of the NS, sensory receptors of the PNS sense the internal and external environment (e.g. blood pressure and touch). Afferent signals are carried to the CNS that analyses information, makes decisions, and sends commands. Afferent signals from the CNS are carried away to the organ effectors (e.g. muscles and glands). Therefore, the NS is the communication and control system of the human body [19]. If this system is attained by an impairment or a damage, a disability may occur and a rehabilitation strategy is required to restore the lost functions.

1.3.2. SCI and stroke pathologies

SCI and stroke are neurological pathologies that disrupt the physiology or the functioning of the NS. They are damages that dysfunction, respectively, the spinal cord and the brain.

A SCI is a damage to the spinal cord that affects motor, sensory and autonomous functions of the human body [10][25]. It results from both traumatic and nontraumatic causes. Traumatic SCI happens due to a physical impact such as accidents, vehicle crashes, violence, falls and so on. A nontraumatic SCI results from poor health condition like infectious diseases and tumors that may affect the spinal cord [24].

Lesion (damage) to the spinal cord may destroy signals traffic to/from the brain and it can lead to a dysfunction of movement control even if muscles are valid. Lesions to the spinal cord are classified by the Neurological Standards Committee of the American Spinal Injury Association (ASIA), standardization is in the aim of providing rigorous information between clinicians and research fields [25]. A SCI may be complete if there is no preservation of sensory and motor functions at S4-S5 region of the spinal cord, whereas an injury is said to be incomplete if any sensory and/or motor function is preserved below the neurological level including the sacral segment (S4-S5) [25]. Moreover, lesions can be at different regions of the spinal cord. The higher the region of damage is, the greater impairment will be. Cervical SCI is defined as tetraplegia, it causes paralysis in the four limbs, the trunk and the pelvis. Damage in the thoracic, lumbar or sacral regions is called paraplegia. Where the trunk, legs and pelvis are involved with an impairment depending on the level of injury [25].

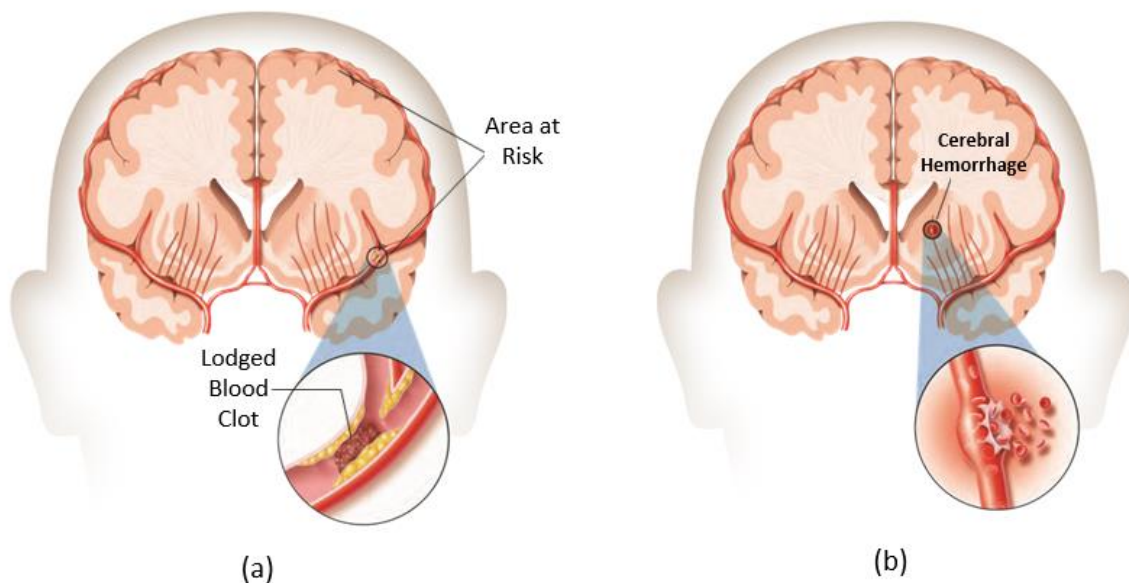


Figure 9: Illustration of stroke causes [23]: a) Ischemic stroke, and b) Hemorrhagic stroke.

Another important cause of long-term disability is Stroke, known also as CerebroVascular Accident (CVA). It occurs when blood supply to an area of the brain is blocked or burst [23][26]. Without oxygen and nutrients, brain cell starts to die within minutes. A Transient Ischemic Attack (TIA) called also mini-stroke takes place if blood supply

is disrupted for a short time, a TIA is a warning for a Stroke. There are two types of stroke: Ischemic Stroke and Hemorrhagic Stroke (see Figure 9). The first subtype is the most common, indeed about 85-90% of strokes are ischemic [3] and it happens when a blood vessel (artery) is occluded. The second one happens if a blood vessel is burst and blood spoils around the brain.

Depending on the function of the damaged location of the brain (see Figure 7), effects of a stroke are: pain, depression, decrease of sensory/motor function, memory problems, vision weakness ... Hence, walking ability may be deteriorated or lost. On a one side of the human body, a motor weakness is called hemiparesis, while a complete paralysis condition is called hemiplegia [27]. After a stroke, 20% of patients became dependent to wheelchair and about 70% are able to rewalk with a reduced performance [28].

After a SCI or a Stroke, on top of primary effects of injury, health condition degeneration such as cardiovascular disorders and musculoskeletal deterioration is another complication for disabled subjects. Therefore measures for an early and effective rehabilitation strategy is substantial [11][12].

1.4. Gait Rehabilitation

1.4.1. Rehabilitation after a neural injury

The fundamental truth for the foundation of rehabilitation is that the NS can acquire new skills and learn by experience [29]. However, rehabilitation can be explained by the mechanism of neural plasticity, which is the neural adaptations and changes in neural circuits to gain a motor skill or to manage a cognitive task [29]. After a CNS or PNS injury, this intrinsic biological evolving and adaptability within the NS, enhances motor function recovery and lessens impairment. Locomotor training is based on the principal “train like you walk”, neural plasticity is linked to the nature of the practiced activity. This approach is known as activity-dependent plasticity which is the enhancement of learning of the neural circuitry in response to the intensive practice of a specific movement which is in our case walking [27]. Patients who practice activity-dependent plasticity, can learn more potentially and hence, gain more effective functional recovery

Furthermore, the neurorehabilitation of walking is explained by the stimulation of neural circuits responsible of locomotion control [30] commonly called central pattern generator (CPG) which is an intrinsic capability of the spinal cord [31][32][33]. The CPG, located at the spinal cord, is a neural network that generates Spatio-temporal information of rhythmic or stepping movements such as walking or swimming. Thus, gait training consists in

stimulating neural activity, and consequently enhancing neural plasticity of neural center of locomotion.

In summary, for neurological deficits where motor/sensory functions are partially preserved, intense training program could encourage the restoration of ambulatory function. After an injury, regeneration and repair of the nervous system occur spontaneously and is enhanced by undergoing a training therapy [10]. Thus walking relearning or restoration of locomotion is gained naturally, and in response to a rehabilitation treatment.

After a neural injury, Task-specific rehabilitation should begin early as soon as possible in order to maximize the potential of gait restoration by accelerating neurological adaptations or neuroplasticity [34]. Developing effective gait training program is the first challenge of rehabilitation specialists. In general, after a neural injury onset, the overall gait rehabilitation process follows three phases: i) mobilized of inpatients into wheelchair as soon as possible, ii) restoration of walking function and, iii) improvement of gait quality [35][36]. To promote locomotion rehabilitation, many approaches have been developed: conventional over-ground training, body weight support (BWS) training, body weight support treadmill training (BWSTT) and robotic-assisted technology [27][29].

1.4.2. Therapist-assisted rehabilitation of walking

Conventional over-ground gait training can only begin if the patient has sufficient strength to stand up in parallel bars or in a hemibar [27][29]. Before being able to sustain in an upright position, therapy starts with some activities in a lying posture, such as passive rotation of the hip, knee and ankle joints. These activities aim to strengthen weak muscles and rise the range of motion of stiff joints. Further, developing various body postures such as sitting and standing balance is important to improve impaired balance [29]. Once enough endurance and stability for standing in parallel bars, therapists assist patients to control torso posture and lower limbs movement. Thereby, one aims the improvement of balance and weight-bearing during gait. In the meanwhile, the patient is asked to practise some single movement of the gait cycle, then as recovery progresses, more complex movements are introduced [37]. Beside physical help, providing verbal instructions is also essential to shape the pattern of gait [29]. For both: stroke and SCI patients, intensive training has promoted walking function recovery [38][39][40][41]. However, conventional treatment requires large assistance of physiotherapists due to the important workload of the rehabilitation task. As a consequence, duration of training is limited which may reduce the effectiveness of walking recovery process.

To help patients to stay in upright position, a BWS system was introduced [42]. Thanks to BWS, patients who are unable to fully weight bear, can benefit for an early training in secure and safe condition, consequently far from the risk of falls. A basic BWS device includes an overhead harness to be worn by a patient and a mechanical frame with a counterweight system [43][44] (Figure 10(a)). The BWS provides an easy balance control and reduces gravitational forces which facilitates the practice of stepping movements. Thereby therapists focus only on assisting leg's motion more than assisting balance control.

BWS can be used for overground training [43] (Figure 10(a)), but for a more practical rehabilitation, BWS is usually carried out using a treadmill (Figure 10(b)). This method is known as Body Weight Supported Treadmill Training (BWSTT) which is the technical translation of task-oriented training. Severely injured patients with limited voluntary motor function can benefit from an intensive gait training resulting in enhancement of training-induced neural plasticity of the CNS [27]. One shall note that the word partial is often used with BWSTT since the amount of unloading can be adjusted [45]. The amount of BWS is high in the beginning of therapy and as walking capacity evolves, the amount is decreased gradually [46].

For a hemiparetic person, while be suspended through a harness over a treadmill (see Figure 10(b)), one clinician provides assistance to pelvic rotation movements and another clinician guides foot placement [27]. In the meanwhile, various parameters can be adjusted such as the level of weight support, walking speed and temporal specifications of the gait cycle [29]. The action of the BWS can be cancelled if the patient reaches a full weight bearing, then treadmill speed is gradually increased as walking ability progresses.

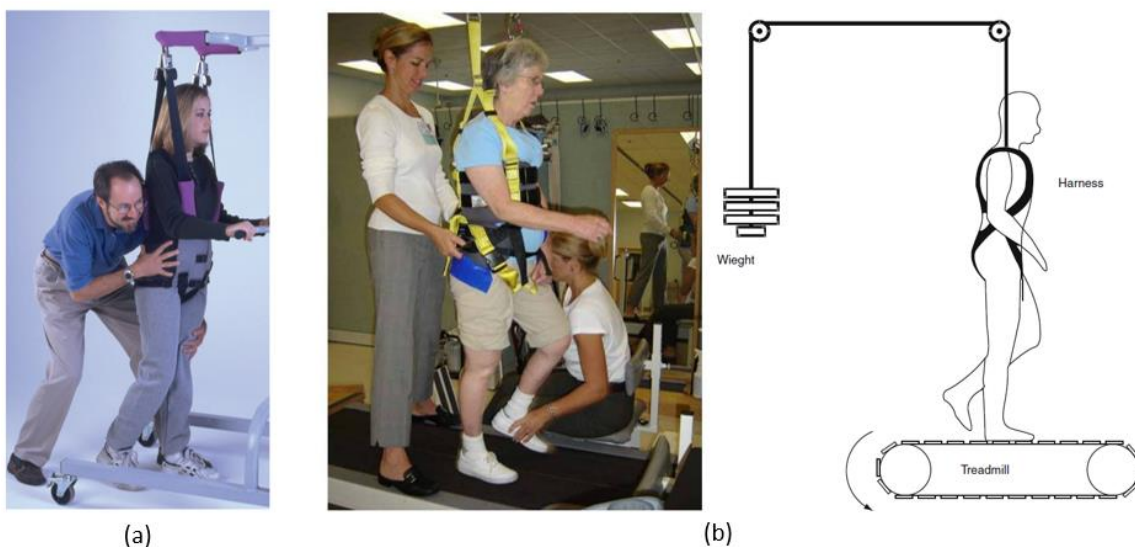


Figure 10: Therapist-assisted training [27]: (a) Overground BWS training, and (b) BWSTT.

The BWSTT facilitates the task of clinicians to provide a regular gait pattern, as close as possible to the natural gait pattern. Moreover, acute SCI and chronic Stroke patients can benefit for an early and safe training. Postural stability is given by the BWS and the regularity of gait pattern is promoted by the treadmill. Viewed as a task-specific practice, BWSTT has been demonstrated a good improvement of motor function for overground locomotion compared to conventional treatment [47][48][49][50].

Furthermore, therapist-assisted BWSTT is a secure and effective strategy for gait training. Many studies has confirmed improvement of walk speed, endurance and walking ability [27][51][52]. However, this approach is still limited by the performance of assistants and physically-demanding due to intensive labour work. Depending on the severity of injury, up to 3 assistants may be needed to ambulate disabled persons [45].

1.4.3. Robotic-assisted rehabilitation of walking

During a BWSTT, the use of assistive devices such as robotic systems is very helpful by giving prolonged and regular task-oriented training, thereafter enhancing motor recovery. Compared to Therapist-assisted BWSTT, robotic-assisted training promotes recovery of ambulation by increasing the total duration of therapy and decreasing the labor and intensive workload [45]. For Manual-assisted training, sessions are limited by the physical performance of the trainers, and further, spatio-temporal specifications of the gait cannot be reproduced faithfully. On the contrary, automated machines replicate the task of therapy continuously, accurately, and consistently. Further, gait parameters can be adjusted precisely. All these advantages contribute to enhance learning capacity and should lead to a more effective gait recovery [45][53][54][55][56].

Design and development of rehabilitation robots have been began since the 1960s [57]. For gait training, Several types of robotic-assisted systems have been developed, their design outlines focus on suspending patients and assisting the motion of legs [36]. Mainly, such system are made out of: i) a mechanized BWS with controllable body weight unloading [46][58][59][60][61][62][63], ii) actuated orthoses with programmed gait trajectories, to be attached to the lower limbs, and iii) with or without a treadmill to emulate the overground walking. These machines aim to provide a physiological gait pattern with both: a minimum intervention of therapists, and adjustable gait parameters such as walk speed and the amount of unloading.

The basic control strategy of gait training consists on reproducing the walking pattern regardless of the participation of patients, i.e., guiding movement on fixed gait trajectories. This

position control strategy is largely implemented in robot-assisted gait trainers, it consists of a control system that tracks joint angles and applies motor torques with reference to normative gait trajectories obtained from experiments [64][65]. Conversely, an important determinant in gait training of a wide range of neurological injured patients is the voluntary effort and the active participation of a subject to achieve a movement [64][66]. Control strategies that take into account forces produced by patients are known as patient-cooperative approaches. In the literature, the terms: patient cooperative, assist as needed, compliant, force-controlled, adaptive and interactive robots are used to design patient's involvement in gait training [66][67][68]. Cooperative approaches are introduced by employing impedance and adaptive control systems [64][66].

Structurally, robotic devices can be distinct into 2 forms: first there are the powered exoskeletons: a serial robot attached to the thigh and the leg, and second ones are devices that use movable footplates to drive the feet. Another possible form is similar to the first one, but powered orthosis are substituted with flexible elements such as cables.

Among various trainers from the first form we cite: The Lower Extremity Powered Exoskeleton (LOPES) [67], the Ambulation-assisting Robotic Tool for Human Rehabilitation (ARTHUR) [69], the Active Leg Exoskeleton (ALEX) [70], the Pelvic Assist Manipulator and the Pneumatically Operated Gait Orthosis (PAM /POGO) [71], Lokomat [72], LokoHelp [73], ReoAmbulator [74]. And from the second type, we mention: The Gait Trainer (GT) [75], the haptic Walker [76] and the gait robot G-EO [77].

The LOPES system designed in the University of Twente (Enschede, The Netherlands) combines a 3 DOF pelvic support, and a 3 DOF exoskeleton for each leg [67]. The pelvic support has two actuated horizontal motions along posterior/anterior and medial/lateral directions. However, the superior/inferior displacement is kept for free motion. The vertical displacement of the pelvis is weight compensated using a spring mechanism, i.e., a suspension system. Connected to the pelvis support, each leg's exoskeleton has two rotations at hip joint (flexion/extension and Abduction/ adduction), and one rotation at the knee. The ankle joint is left free Thus the mechanism has a total of 8 actuated joints and one passive DOF. In addition, the LOPES includes a treadmill to achieve walking. Upright standing and balance control have to be carried out by the patient.

Interaction between the LOPES and the patient is achieved through an impedance control. For that, the active joints consist of elastic actuators made out of Bowden cables. Indeed, two operational modes can be selected: "patient-in-charge" and "robot-in-charge". For the first, the LOPES follows patient in unconstrained movement and for the second, the system

guides the patient for a prescribed gait pattern. The Evaluation of the LOPES with healthy persons in “patient-in-charge” mode during a free walking showed a pattern close to a free treadmill walking [67]. A new LOPES system (Figure 11(a)) was designed including a BWS system [65][78], a clinical trial has showed positive therapeutic outcomes in training four out of five stroke subjects [78].

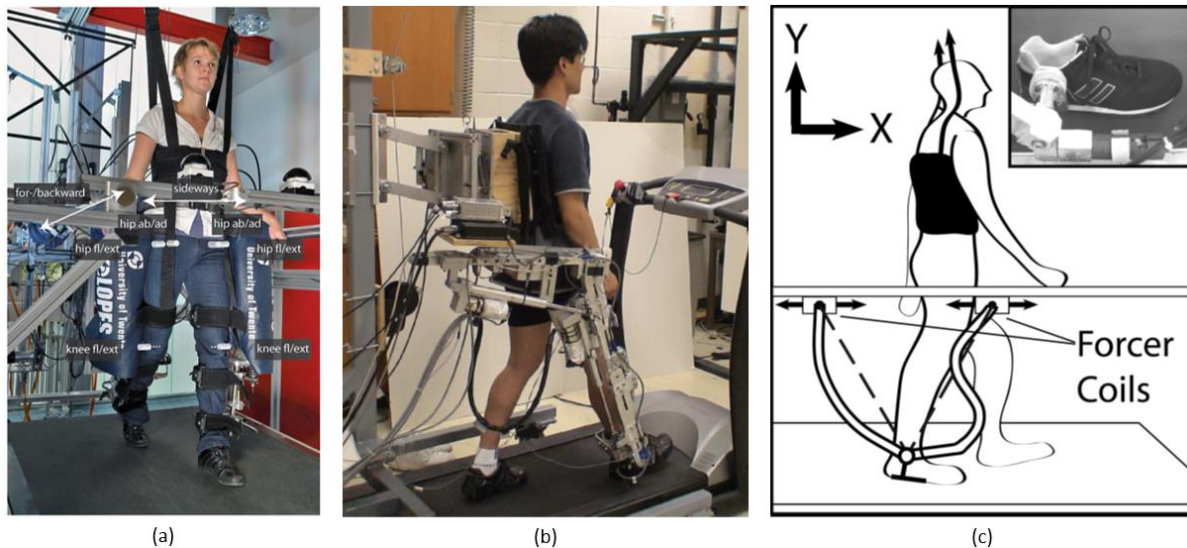


Figure 11: (a) The new LOPES system [65], (b) The Alex prototype [70], and (c) Diagram of the ARTHuR gait trainer [69].

The active leg orthosis ALEX (University of Delaware, Newark, The USA) [70], conceptually based on the passive Gravity Balancing Leg Orthosis [79][80], combines a trunk orthosis and a leg orthosis (Figure 11(b)). The first part is a partial weight support device that keeps the patient stable on a treadmill through a harness system and it has 4 passive DOF held with springs. The second part embodies two linear actuators to actuate the hip and knee joints in the sagittal plane. To allow interaction with patients, the ALEX relies on the use of a force-field controller. In contrast to the LOPES, ALEX uses friction compensation method in place of series elastic actuation to achieve backdrivability of the device [81]. Thereby, training is based on the “assist as needed” approach in which the robot assists or resists the leg’s motion on a desired trajectory [70]. By training two stroke patients, improvement of gait pattern including walking speed and joint excursion was reported [82].

The ARTHuR consists of two horizontal linear motors that drive two linkages connected at their ends [69] (Figure 11(c)). The end-effector can be attached at the knee or the ankle in order to move the lower limb. Interaction with legs is possible through the use of linear motors that have low backdrive friction and can exert substantial force. Training is based on teach and replay technique, consisting in recording motion during manual assistance and then replaying

it during robotic-assisted training. Evaluated on SCI patients, ARTHuR has demonstrated a reliability to replay trainer-induced stepping movement [83].

Designed at the University of California (Downey, USA), The PAM/POGO is a pneumatic trainer able to be compatible for full range of natural gait movement of both: the pelvis and the legs (see Figure 12(a)) [71]. The Pelvic Assist Manipulator (PAM), used to assist the pelvic motion, is a two 3-DOF robotic segments, each one has three pneumatic cylinders assembled in a tripod configuration. Compliant with the PAM, the Pneumatically Operated Gait Orthosis (POGO) is a pneumatic device (2 cylinders per leg) that actuates the hip and knee joints in the sagittal plane. The PAM/POGO is a force controlled system, in fact it is capable of producing large force with a lightweight moving parts, .i.e., the system is backdrivable. Therefore, the system is able to drive the patient through a reference trajectory. Initial experiments with SCI patient were achieved successfully [71].

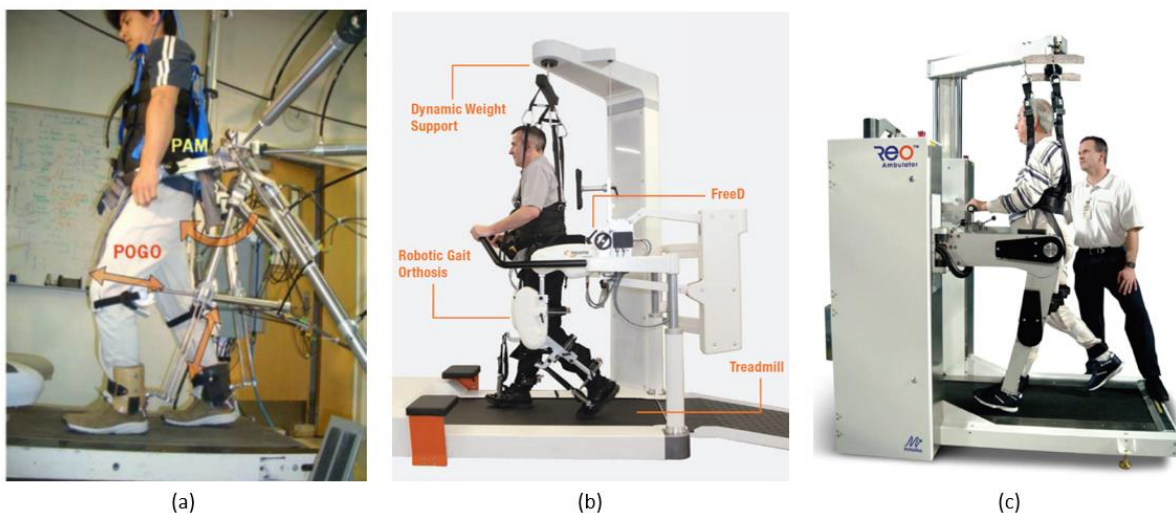


Figure 12: (a) Experimental setup of the PAM/POGO [71], (b) Lokomat system (picture courtesy of Hocoma AG [84]), and (c) ReoAmbulator (picture courtesy of Motorika Ltd. [85]).

The Lokomat trainer (Hocoma AG, Volketswil, Switzerland) is made out of a Driven Gait Orthosis (DGO), a counterweight BWS and a treadmill [72]. On one hand, the suspension system combined to a rotatable parallelogram mechanism, stabilises the movement of patient's torso in vertical direction and produces a weight unloading. On the other hand, The DGO drives the thigh and the leg, respectively, at the hip and the knee. Joints actuation is conducted through DC motors and linear ball screws. The ankle joint is stabilized using a foot-lifter made of elastic straps. The controller of the Lokomat synchronizes the speed of the treadmill and the speed of the DGO to generate a gait-like pattern. The extended version of the Lokomat (see Figure 12(b)) includes advanced features such as: i) impedance-control allowing assist as needed training

[66][86], ii) optional module allowing pelvis lateral displacement and hip abduction/adduction, and iii) augmented visual feedback [87].

The electromechanical gait device Lokohelp operates with a double side levers device , a BWS system and a motor-driven treadmill [73]. The treadmill plays a double function: emulation of overground walking and a driver for the levers device. For each leg, an orthosis stabilizes the ankle joint and has to be connected to one lever that transmits the gait pattern by following a mechanical track. Thereby, gait simulation is produced by guiding the ankles' orthoses. The feasibility of the Lokohelp is confirmed by training patients with different neurological injuries, in fact likewise manual BWSTT, same improvement is observed using the LokoHelp machine [73][88]. A main limitation of this device is that generated gait shape is constrained mechanically, and hence cannot be adjusted.

Similar to the Lokomat, The ReoAmbulaotr/Autoambulator (Motorika Ltd., USA /HealthSouth Corp., USA) [74] is a BWSTT powered gait orthosis (see Figure 12(c)). Simulation of walking is carried out using two robotic arms (i.e., exoskeleton). Each arm has two DOF (for hip and knee joints) and has to be strapped at the thigh and the ankle. Moreover, a lifting mechanism (i.e., a BWS) suspends and holds the patient over the treadmill [74]. Significant improvement was reported following the treatment of hemiparetic stroke patient [89].

Now moving to the second type (movable footplates) of gait restauration systems. The Gait Trainer I (Reha-Stim GmbH /Free University, Berlin, Germany) drives the lower limb by moving the sole of the foot [75]. The patient is secured by a harness system and positioned over footplates (Figure 13(a)). The gait pattern is produced by a planetary gear system, simulating foot motion during a gait cycle. In addition, vertical and horizontal motions of the patient's CoM are controlled via ropes attached to the harness. Advantages of such system is that no constraints are putted on the hip and knee joints. Further, physical therapists can apply corrections to the motion of the knee (Figure 13(a)). Although operating in position control with the lack of any force control [90], multiple evaluations including the largest clinical study DEGAS [91] have confirmed the effectiveness of the Gait Trainer I [91][92][93].

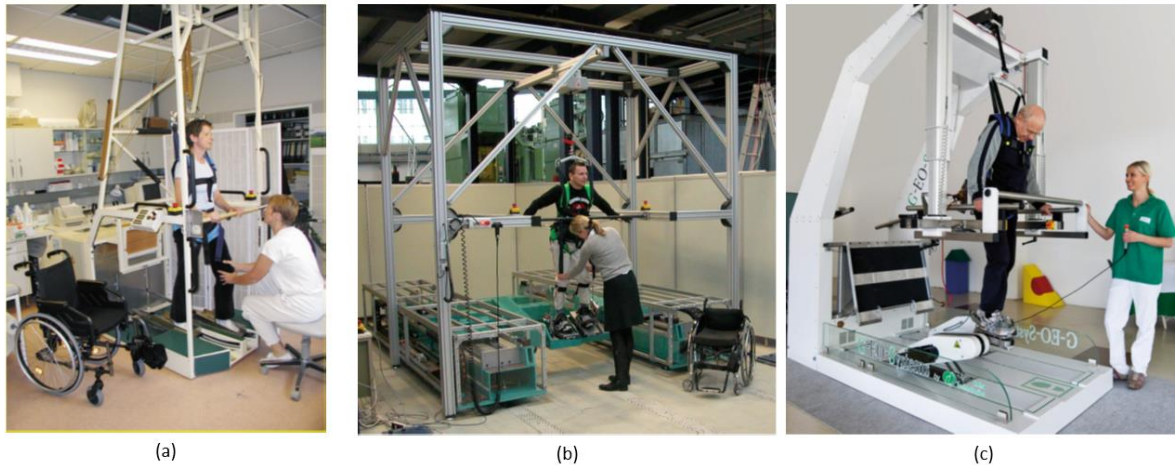


Figure 13: (a) the Electromechanical Gait Trainer [90], (b) The HapticWalker walking simulator [90], and (c) the gait robot G-EO [94].

In contrary to the Gait trainer which provides pure passive guiding, the HapticWalker [76] and the gait robot (G-EO) [77] have two freely programmable 3 DOF footplates. This feature allows training patients for repetitive daily life walking situations such as stair climbing.

The HapticWalker is a redesign of the Gait Trainer I aiming the achievement of high dynamics and arbitrary motions [76]. This machine is a heavy robot manipulator driven by powerful electric drives to reach high speed movements. Each foot platform includes a six DOF force/torque sensor allowing the measure of the interaction with a patient. Preliminary trials with stroke and SCI subjects are encouraging. Further, evaluations are under-going [90][95].

The G-EO (Reha Technologies, Bozen, Italy) was designed to train stroke patients [95], its mechanical structure is smaller than the HapticWalker. In addition to feet actuation, the patient's CoM is controlled in vertical and lateral translations. Tests with simulated floor walking and stair climbing showed comparable muscle activation between real and simulated movements, which confirms the feasibility of the G-EO in training stroke patients [77]. Moreover, an adaptive control strategy is implemented by measuring foot reaction forces via a pair of overshoes [96]. Seeing that main drawback of footplates-based trainer is the lack of true swing phase since the foot is in permanent contact with the machine [96], the adaptive algorithm allows a natural gait simulation by controlling the resistive force of the footplates.

Amongst all above described training machines, only five of them are commercially available: the Lokomat, the ReaAmbulator/AutoAmbulator, the Lokohelp, the Gait Trainer I and the G-EO. Clinical trials in stroke patients reported the superiority of the Lokomat and the Gait Trainer I in gait function recovery [77].

1.4.4. Cable based system for gait rehabilitation

Aforementioned exoskeleton type and movable footplates form machines have been largely studied and evaluated. Further, they are effective and reliable for gait training [36][57][64]. However, such systems are heavy, bulky and potentially dangerous, consequently they require complex safety techniques. Since rehabilitation is based on a pure interaction with patients, development of patient-friendly rehabilitation robots is substantial [97]. Safety, reliability and flexibility are high-demanding standards for robot-aided rehabilitation devices.

Widespread of current rehabilitation machine is hindered by their expensiveness. For example only 600 Lokomat units have been sold since 2001 [84], the price is about 300 000 \$ per unit [98]. As consequence, many patients will be unable to receive an adequate therapy and conversely by using low cost gait trainers' multiple machines may be installed within a clinic. Consequently, development of rehabilitation devices should make a priority for simple and cost-effective designs.

In this context, cable robots have promising features including lightweight structure, large reachable space, low cost and easy setup. Thus, integration of cable robots into rehabilitation machine could be very advantageous [99][100].

Moreover, features such as lightweight and high dynamics [101] promote the backdrivability of the machine, thus assist-as-need approach can be easily implemented. One shall note that compliance paradigm is essential with hemiparetic stroke subjects since patient has one valid leg and one paretic leg. Patient-cooperative training appears to be more suitable than fixed trajectory control strategy since the first one encourages active and voluntary involvement of patients during gait training [99].

Another possible advantage of cable robots is the simplification of the setup procedure to start a training session. For the exoskeleton type machine, an alignment of patient's joints and the robotic arm joint is substantial which is not required for cable robot, thus the setup is easier and shorter using CDPM [99].

Based on wire technology, the first system that addresses rehabilitation of walking is the STRING-MAN [102], developed at Fraunhofer Institute IPK (Berlin, Germany). STRING-MAN is a dynamically controlled weight-suspension and posture control support for the practice of treadmill gait training. The first design had a mechanical configuration of 7 cables (see Figure 14(a)) that drive the trunk and the pelvis by mean of a harness worn by the patient. Thus, the robot can be described as a 6 DOF system for posture control and partial weight bearing. Each wire is connected to the patient via a pulley and is actuated by a linear drive. The STRING-MAN is equipped with a powerful sensory system allowing its interaction with

subjects. Such sensors are: foot gait phase detection sensor, reaction force sensing (foot forces) and zero-moment point (ZMP) estimation sensor, knee-goniometer, wire force and linear actuator position sensors, as well as pulley rotation sensors [102].

Wire sensors are used to measure Cartesian body position and Cartesian body forces including the amount of weight bearing. Further, integrated sensors allow detection of different gait phases, and possibly an abnormal walking.

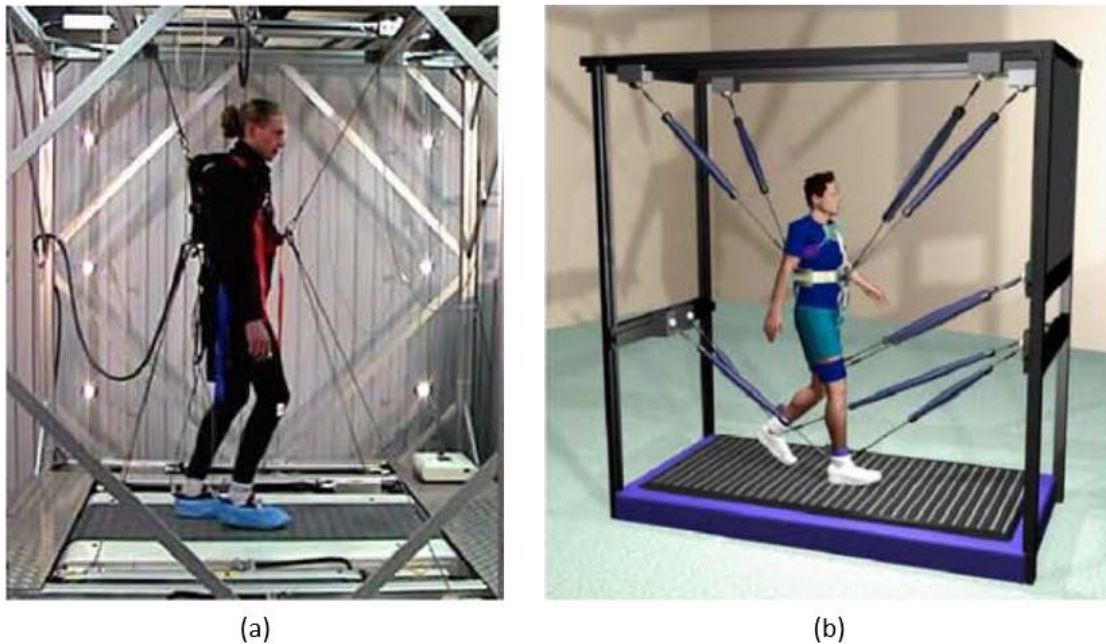


Figure 14: (a) Experimental setup of the STRIN-MAN system [100], and (b) Concept of the SMART-STRING system [100].

The control algorithm includes a robust position-based impedance controller and a force controller. These controllers are substantial to control the robot-human interaction allowing the support of patient voluntary initiative. Further, the system can be tuned from totally passive to completely active. However, human body motion cannot be well estimated due to geometric uncertainties, harness elasticity, flexibility of wire's attachment point. In fact the robot is never controller in position mode [100]. Moreover, safety measures are critical and require improvement.

First experiments have been performed with dummies and healthy subjects. For weight balancing reasons, it was observed that satisfactory results could be obtained using a 3 DOF/4 wires configuration. Besides, to actuate the lower limb 3 wires per leg may be added. To improve the actuation technology, it was proposed to actuate wires using a Pneumatic Artificial Muscle (PAM). This concept is called SMART-STRING (see Figure 14(b)).

As a second system, the Cable-driven Locomotor Trainer (CaLT) is a compliant robot, i.e., generates controlled forces on the legs [103]. This device uses the technique of counterweight BWSTT combined to a cable robot to drive the lower limbs. Each leg is driven by two cables through an attachment around the ankle (Figure 15). Four spools coupled to motors drive the 4 cables via pulleys. Torque load cells are inserted between motors and spools to record the applied torques. Further, to get the position of the ankle, a custom three dimension sensor is used. This architecture allows to control the assistance/resistance force during locomotor training. In fact, the cable robot can be moved with minimal resistance force, i.e., the system is highly backdrivable. Therefore, the robot can assist stepping movement if patient is unable to step forward during treadmill walking. Feasibility of the CaLT was carried out by training fourteen stroke subjects and nine SCI individuals. Results have showed significant changes in walking capacities with both type of patients. It was found that the CaLT system is feasible in training people with stroke and chronic SCI people [99].

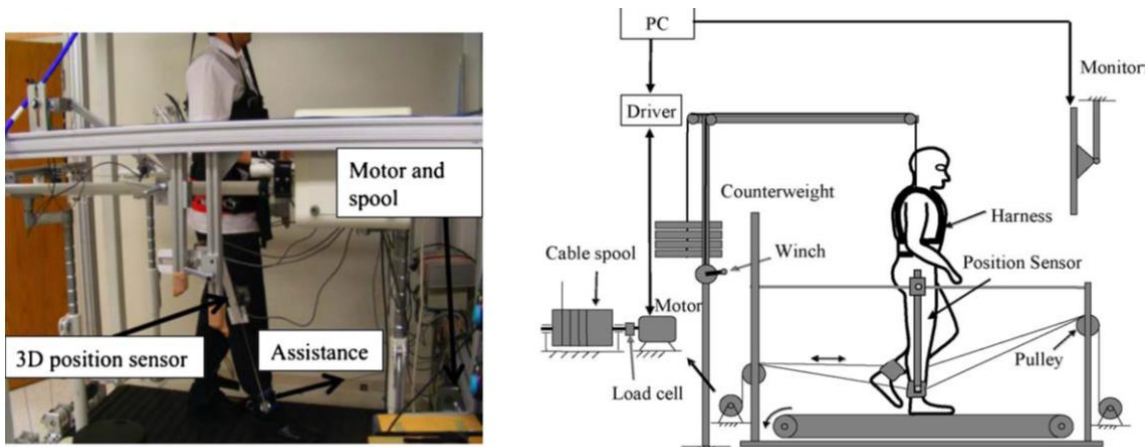


Figure 15: Description of the CaLT gait trainer [103].

Eventually, based on rigid links, classical rehabilitation devices are heavy, expensive and fairly ergonomic. Conversely, Cable robots have various promising features including low inertia, ability to reach high speeds, low fabrication costs and easy to setup. Moreover, such robots are highly backdrivable and compliant which allows to implement assist-as-needed training paradigm. Up to now, there are no market available wire-based gait training machines. Ongoing developments aim to exploit benefits of wire robots while overcoming some limitation such as various geometric uncertainties and tensionability constraints [99][101].

1.5. Design of the Cable-Based Gait Rehabilitation Machine

In this work, we propose a machine based on a CDPM, called the CDLT. It includes: a Body Weight Support Device (BWSD), a Cable-Driven Leg Manipulator (CDLM) and a treadmill (T). A new orthosis was designed to be attached to the leg and it is controlled by a cable system to move the lower limb. The number of cables was chosen in a way to totally restrain the movement of the orthosis in the sagittal plane. This design comes with all the benefits of cable driven robots. Hereby, a diagram of the CDLT is presented in Figure 16.

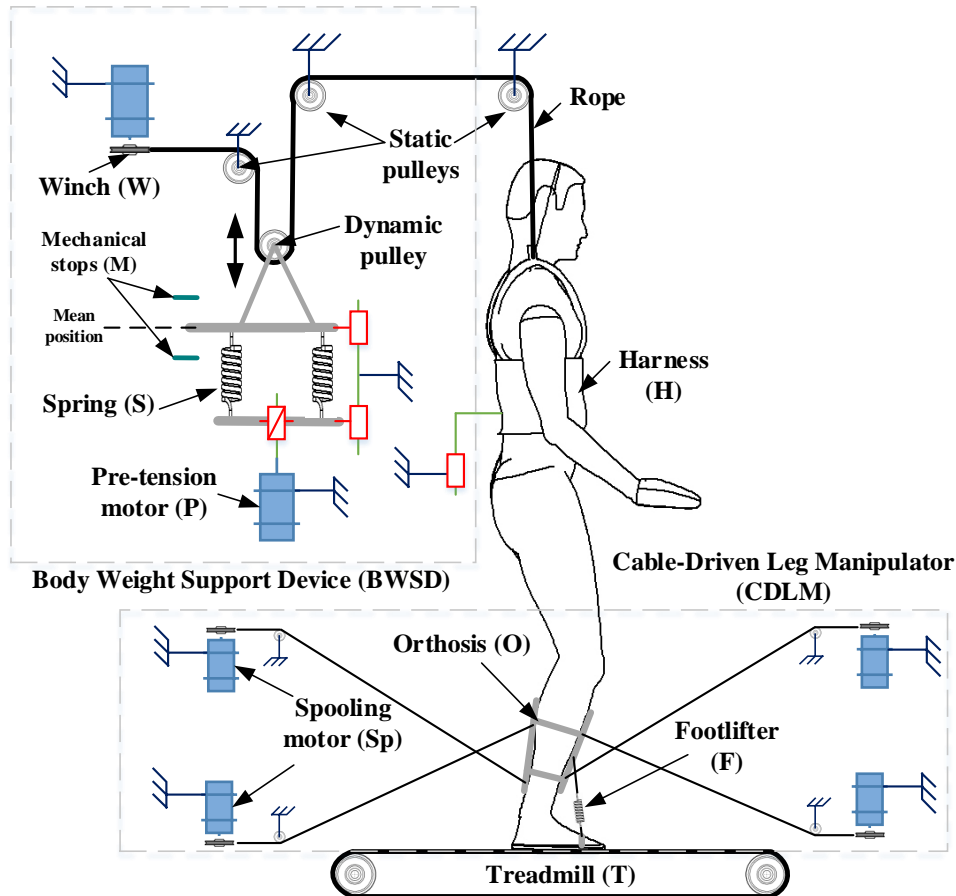


Figure 16: Mechanical description of the proposed gait training machine.

As included in all gait rehabilitation devices, this design comprises a BWSD made out of elastic springs. In the literature, there are various architectures for BWS [46]:

i)-Static System (Figure 17(a)): in such mechanisms, the harnessed patient is lifted using a basic winch (Figure 17(a)). The spooling action can be made manually or using an electric motor. The desired unloading is proportional to the lifted distance. More sophisticated systems integrate a force sensor to help in adjusting the amount of unloading. Irregularity of the weight support and restrictions of the pelvic vertical displacement are the major drawbacks of static devices.

ii)-Passive Dynamic Counterweight System (Figure 17(b)): unlike static systems, in this case, the patient is unloaded by means of a mass that produces a gravitational counterforce. During a gait, changes in counterweight acceleration yield inconsistent unloading.

iii)-Passive Dynamic Elastic System (Figure 17(c)): The suspension force is generated by a set of springs or other elastic elements. Thus, the amount of unloading is proportional to the tension in the springs, when the inertia of the moving parts is neglected. The unloading force is relatively stable since it follows the variation in the spring length. The use of long springs with low stiffness can lessen force rippling. A patented design [104] showed that more suitable results are provided by adding an extra elastic force exerting element in a way to compensate the deviation in the main force.

iv)-Active Dynamic System (Figure 17(d)): Similar to the previous system, the integration of an active force generating mechanism allows to eliminate the variations in the suspension force. As an example, the active Lokolift system [46] produces this compensation force through a closed loop between a force sensor and an electric drive. Such system produces a relatively constant unloading, further it performs a rapid change between different BWS values. Compared to the aforementioned BWS devices this one is relatively more complex.

The passive elastic BWS is widely used in training machines, it offers good results with respect to a simple and basic mechanism. A similar mechanism called the BWSD is included in The CDLT (Figure 16).

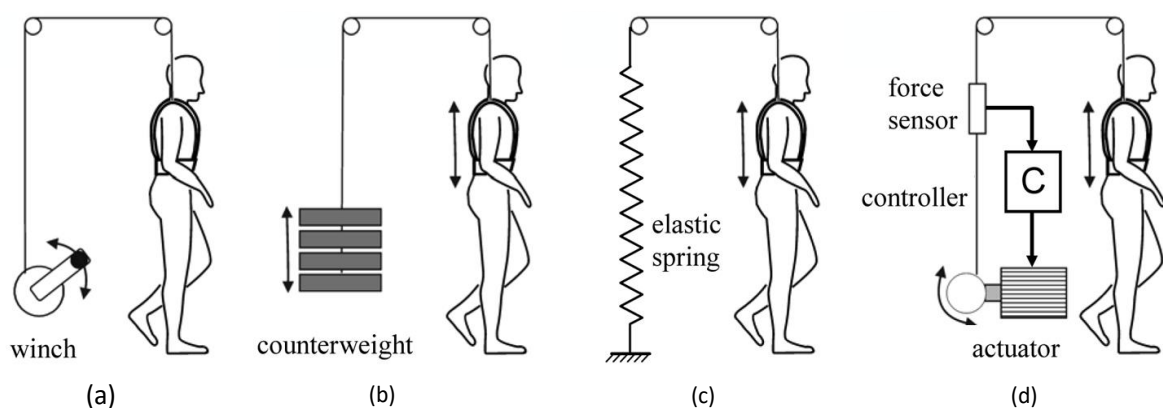


Figure 17: Common body weight support systems [46]: (a) Static BWS: a simple winch, (b) Passive dynamic BWS with adjustable counterweight, (c) Passive dynamic BWS with elastic spring, and (d) Active dynamic BWS with force-control loop.

The unloading force is transmitted from the BWSD to the patient through a cable, which is guided via a series of pulleys and attached to the harness (H). Major parts of the BWSD are two translational guided parts (see Figure 16). The first is equipped with a dynamic pulley to transfer the unloading force from the springs to the rope. Note that the movement of this part is

limited by two mechanical stops. The second one is coupled to a power screw driven by a motor (P). The two sliding parts are connected with springs (S). The pre-tension motor (P) controls the position of the lower sliding part, and hence adjusts the springs pre-tension. Thereby, the amount of unloading is selected. The electric winch (W) spools the rope to lift the patient from a sitting to a standing position, further it allows the springs to work in a specific range.

The operational procedure of the BWSD is as follows:

i) The patient is secured by the harness in a sitting position, then we apply the desired amount of unloading through the pre-tension motor (P). In such position, the upper sliding part is in contact with the lower mechanical stop.

ii) The patient is lifted until there is no contact between the patient's feet and the treadmill. Here, the upper sliding part is in contact with the upper mechanical stop,

iii) The patient is lowered until the upper sliding wagon is lying in the middle of the two mechanical stops.

During walking training, the dynamic pulley moves alternatively around a mean position (Figure 16) following the variation of the vertical position of the patient. Meanwhile, the suspension force is produced by the springs' tension, which is proportional to the instantaneous position of the dynamic roller added to the selected spring offset. One notes that a force sensor is required to measure the instantaneous unloading, and hence to adjust the desired amount around a mean value.

The second subsystem of the CDLT, which is CDLM, includes a 4-cables robot (see Figure 16). The moving platform is an orthosis (O) placed around the leg. In addition, a foot-lifter (F) is positioned between the orthosis and the foot in order to stabilize the ankle joint when the foot is off the ground (similar to the Lokomat system [72]).

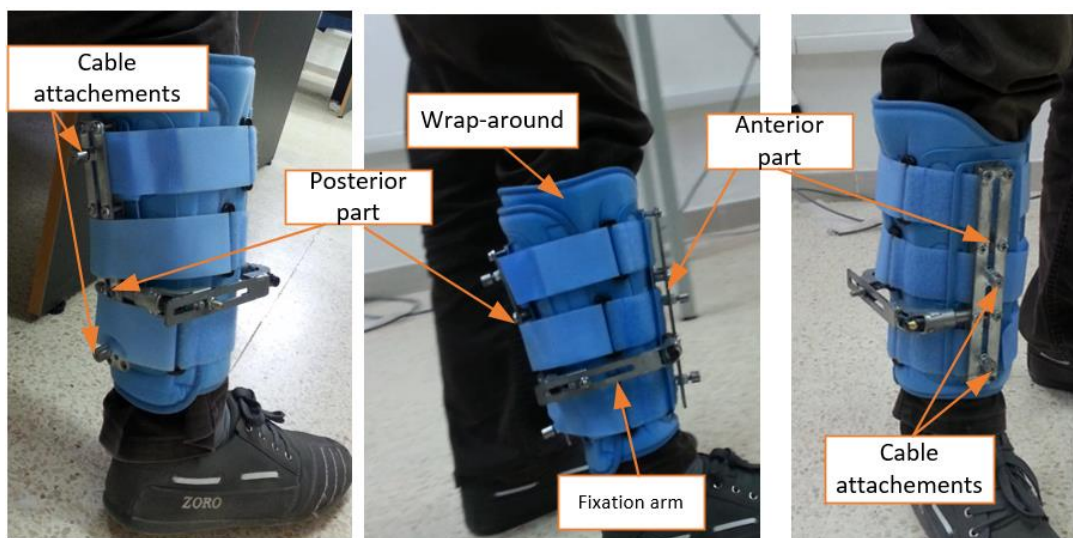


Figure 18: Prototype of the leg's orthosis.

The design of the leg's orthosis is inspired from commercially available motion control knee splint. On one hand, the design involves the use of a wrap-around part that provides stability and comfort to the patient's leg. On the other, the orthosis comprises two parts positioned at the anterior and the posterior sides (i.e., front and back) of the leg (Figure 18). Once, the two parts are placed around the leg, they are blocked using a fixation arm. This element has 3 passive DOF (2 rotations and one translation) to be tightened when the orthosis is mounted. The fixation arm allows to assemble the two parts as one unit and hence to keep the distances between the cable attachments as constant as possible. If these distances vary, the position control of the mobile platform will be erroneous since its geometry is not consistent.

Viewing that important ranges of motion are occurring in the sagittal plane, and for the sake of simplicity, the cable robot moves the leg in this plane using a set of 4 cables. In general, for a cable robot with n DOF, $m=n+1$ cables are required to totally restrain the movement of its effector [105]. The leg has 3 DOF in the sagittal plane, therefore, the orthosis is controlled by 4 cables. This will help to keep the orthosis in a given position and minimizes its sliding movement along the leg. Compared to the CaLT system (see Section 1.4.4.), the lower limb is moved using only two cable (see Figure 15), in a such configuration an upward force will be produced, pushing the ankle's attachment to move along the leg.

The overground walking is emulated by employing a treadmill (T), producing the walk forward movement and applying the ground reaction force on the feet.

Conclusion:

A literature review on gait rehabilitation was given in this chapter. Robotized gait trainers enhance therapeutics outcomes when compared to the manually-assisted therapy. In fact, they are the technical translation of task specific and intensive training, which is substantial for an effective recovery of the gait function. Commercially available gait training machines are heavy and very expensive, which is an impediment to provide an adequate therapy for subjects with gait impairment. Cable driven robots could be a good candidate to achieve the task of rehabilitation, they are simple and less expensive. However, their design is challenging, since the tension in the cables has to be maintained positive at all times and cable interference has to be avoided during the motion.

An essential and required information in designing the CDLT is the kinematics and the dynamic of a normal gait. In the next chapter, a gait experiment will be carried out in order to get this information.

2. Analysis of Human Walking

Summary:

Evaluating and studying the performance of the CDLT requires the knowledge of the kinematics and dynamics of the lower limbs during a walk cycle. A quantitative gait experiment is performed to get this valuable information. A subject equipped with a set of reflective markers achieves a walking movement. The trajectories of the markers are recorded using cameras. This information is then used to calculate the orientation of the lower limb segments. A force platform is used to measure the reaction forces of the ground. Before giving the details of the experiment, a description of the gait cycle and its related terminology is given.

2.1. Overview of Normal Walking

A gait cycle (GC) is defined as a sequence of repetitive events, starting and ending with the same event. The two legs have the same series of events, with a phase shift of one half cycle [20]. A normal walk cycle has two main phases: Stance phase and Swing phase (see Figure 19). During stance time the foot is on the ground, over the swing time the foot is no longer in contact with the ground [106]. Further, the GC is also described with 7 successive events resulting in 7 periods: four of them occur during the stance phase and the three remaining make the swing phase (see Figure 19).

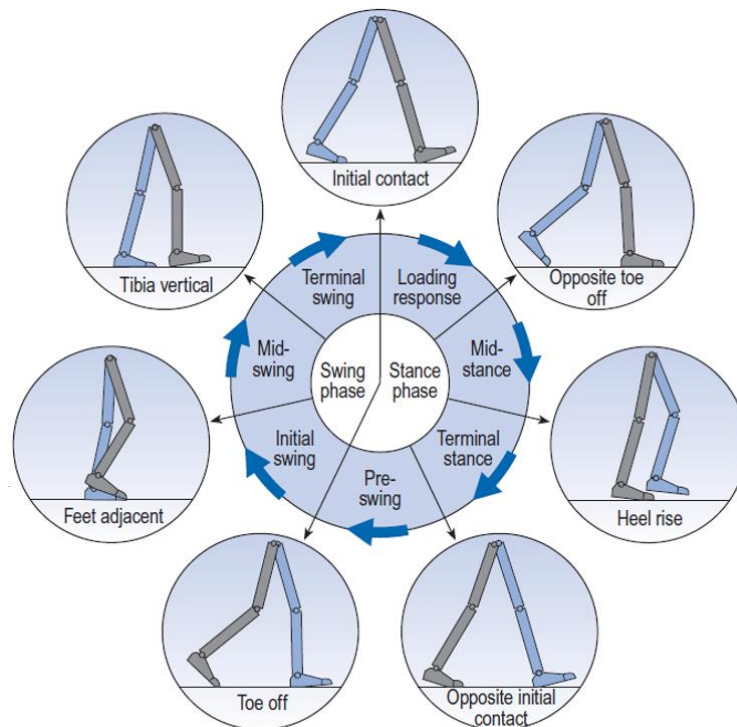


Figure 19: Walk events of the right limb (in gray) during a gait cycle [20].

2.1.1. The Stance Phase

The stance phase represents about 60% of the GC, it has 4 periods: i) Loading response, ii) Mid-stance, iii) Terminal stance and iv) Pre-swing. Moreover, depending on the position of the feet over the ground, the stance phase can be characterized by three successive phases: i) First double support, both feet are on the floor, ii) Single limb support (also called double limb stance), when the current limb is on the ground and the other limb is in the air, and iii) Second double support, once again the two feet are in contact with the ground (see Figure 20).

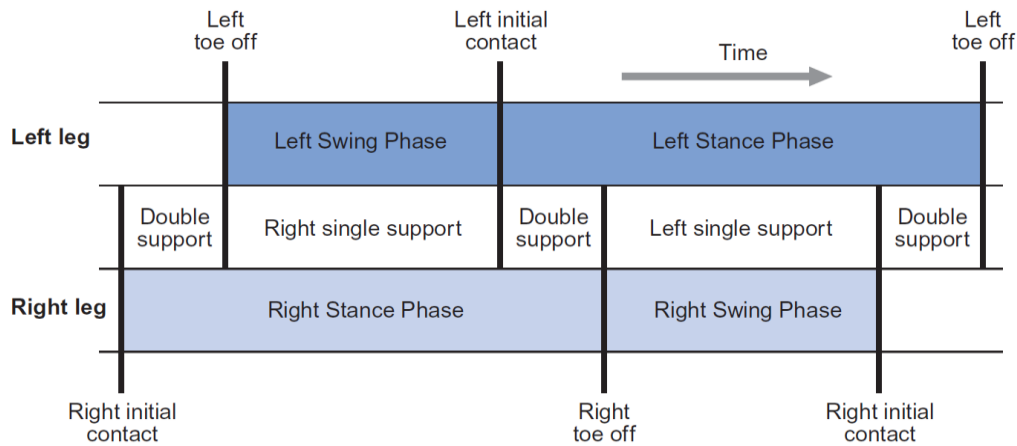


Figure 20: Timing of single and double support periods [20].

The initial period of the stance is the loading response (Figure 19), beginning with an initial contact called also heel strike, in which the foot touches the ground at the heel (see Figure 21(a)). The loading response is the first double support period that occupies 10% of the GC. It ends with an opposite toe off when the opposite foot is going to leave the ground out of the toe (see Figure 21(b)). In the meanwhile, the direction of the ground reaction force is upward and backward.

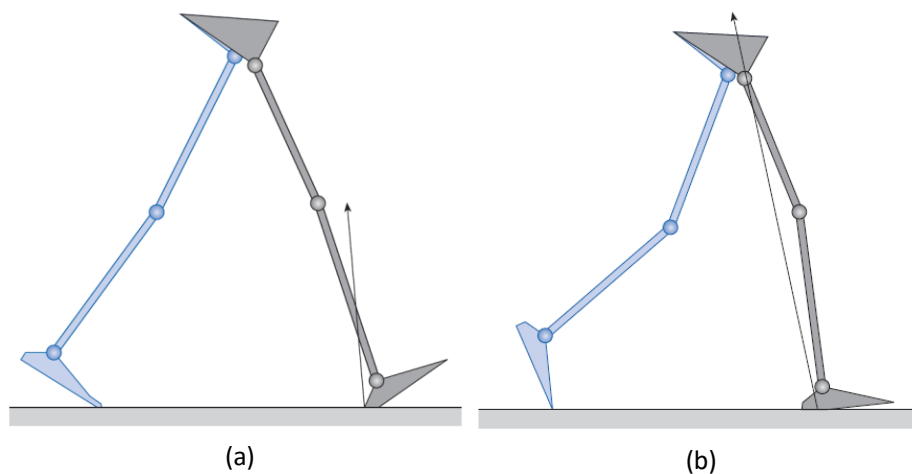


Figure 21: Right leg (in gray) at [20]: (a) Initial contact, and (b) Opposite toe off.

The Mid-stance is the time (approximately from 10% to 30%) between the opposite TO and a heel rise. In addition, it represents the first part of the single support phase. The heel rise event (see Figure 22(a)) known also as heel off is identified when the foot is flat on the ground and the heel begins to lift the floor, further the ground reaction lies vertically.

The Terminal stance is the third sub-phase of stance that ends with an opposite initial contact at 50 % of the GC (see Figure 22(b)). The terminal stance and the single support period terminate at the same time.

The Pre-Swing is the last period of the stance (approximately from 50% to 60% of the GC) between the initial contact of the opposite foot and a toe off of the current one (see Figure 22(c)). Ending of this sup-phase points also the end of the second double support. During terminal stance and pre-swing, the ground reaction is upward and forward.

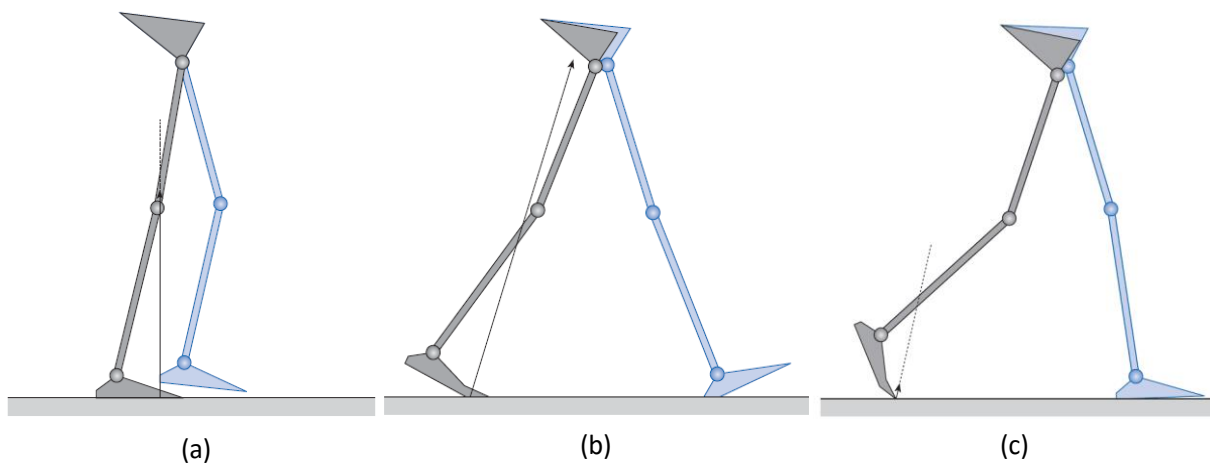


Figure 22: Right leg (in gray) at [20]: (a) Heel rise, (b) Opposite initial contact, and (c) Toe off.

2.1.2. The Swing Phase

The swing phase lasts 40% of the gait cycle and is often subdivided into 3 sub-periods: i) Initial swing ii) Mid-swing and iii) Terminal swing. The initial swing varies from 60% to 73% of the GC. It is terminated with a Feet adjacent event (called also feet clearance), in which the swinging foot is adjacent to the stance foot (see Figure 23(a)). Tibia vertical event is the transient between the Mid-swing and the terminal swing occurring at 87% of the GC. Here, the tibia is in vertical posture (see Figure 23(b)). The GC ends when the current leg reaches the ground again, i.e., the next initial contact.

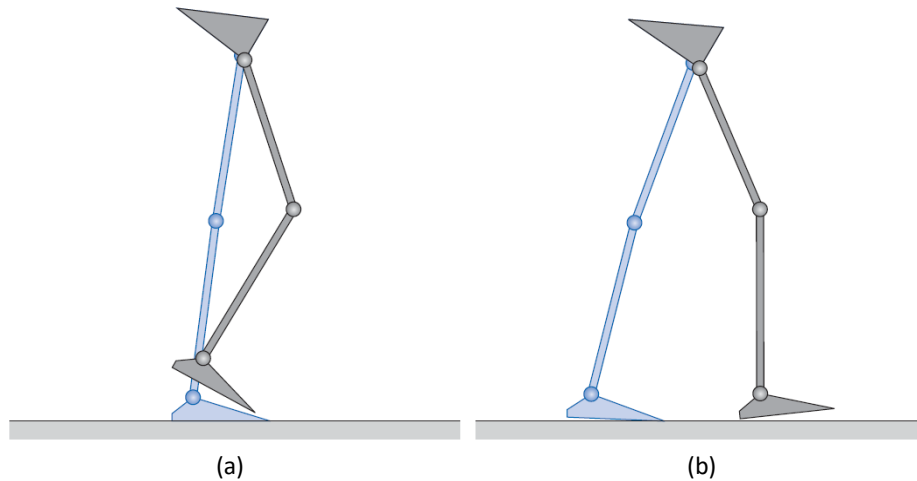


Figure 23: Right leg (in gray) at [20]:(a) Feet adjacent, and (b)Tibia vertical.

2.1.3. Gait parameters

During a GC, foot placements provide some useful distance parameters (see Figure 24). The stride length is the distance travelled by the same foot during a GC, further it includes two equal forward distances: the right and left step lengths. Each step is the distance between the two feet, left and right, taken at initial contact. Thus a stride can be defined as one step for each foot. Thereby, the speed of walking known also as stride time is the stride length divided the cycle time. In addition, the step width (called also walking base) is the left/right distance between the feet. Finally, the foot angle describes the internal /external rotation of the foot with reference to the direction of progression [20][106].

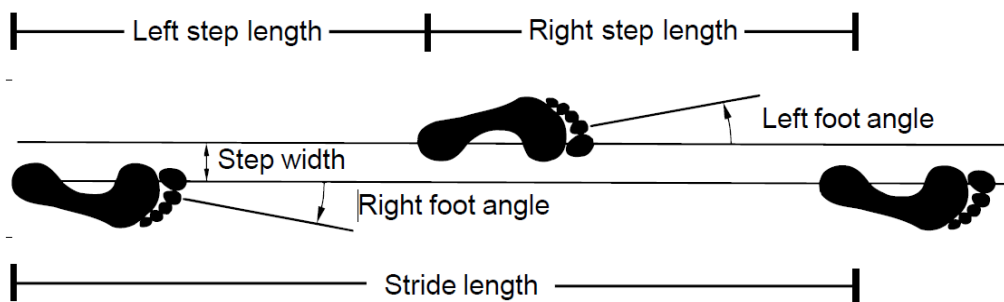


Figure 24: Distance parameters of the gait cycle with reference to feet footprints [106].

2.1.4. Lower extremity angles

From one laboratory to another, measurement protocols of joint angles may differ. Further, in biomechanics, two types of angles are used: absolute angles and relative angles. The first are the angles between a body segment and a fixed coordinate system. Conversely, relative angles or intersegmental angles are taken between longitudinal axes of two adjacent body segments. Therefore, giving definitions of angles when examining joint motions is substantial. When examining motion of the lower limb [20][107], the hip rotation is the angle between the femur

and either the vertical or the pelvis. Positive values are viewed as flexion and negative amounts as extension. Next, the knee angle is often the angle between femur and tibia that is always positive. The ankle angle is the measure between the tibia and a chosen line in the foot, conventionally this angle is equal to zero when the leg is in vertical position or perpendicular to the floor. Thus dorsiflexion and plantarflexion are, respectively, positive and negative angular movements. Note that during walking, important rotational motions take place in the sagittal plane, consequently, gait motion is usually studied in this particular plane.

2.2. Quantitative Gait Analysis

The gait analysis has been performed in the biomechanics laboratory of PPRIME institute (Poitiers University, France), using an optical motion capture system and a force platform. Despite the fact that gait data can be found in the literature, this information is far from being unified due to various dispersing problems [108]. First, as mentioned above (see Section II.1.4), angle definitions may vary from one research unit to another [20]. Second, many errors may be encountered in model calibration, i.e., computation of segment lengths and determination of joint center locations. Indeed, these data may differ based on the applied approach, further marker placement on anatomical landmarks cannot be reproduced accurately [108]. For the carried analysis, different steps of the experimental protocol and data examination details are provided. However, major addressed points are: i) Markers placement, ii) The selected type and range of motions during trials, and iii) Used algorithms for data analysis.

2.2.1. Experimental setup

Simultaneously, gait capture implies both: position tracking of a set of reflective markers placed on a moving subject, and recording of the ground reaction force. The motion measurement device is the Vicon MX infrared optical system (Oxford Metrics Ltd, Oxford, UK), a typical configuration is shown in Figure 25. All cameras are connected to a network controller (MX Ultranet), which sends information to a Host PC for processing. In our case, the system is made of 12 MX cameras (4 megapixel @ 370 fps). Each camera is positioned in a way that its field of view covers as much as possible the captured volume. Each marker must be seen at least by 2 cameras during the capture. In fact, the position of a marker is computed by the Vicon Nexus software based on triangulation process [109]. Moreover, 7 force plates (Kistler Instruments AG, Winterthur, Switzerland) are placed on the floor of the capture volume in order to record the reaction force of the ground at a sampling frequency of 1000 Hz (see Figure 26). Both position and force information are synchronized by the MX system.

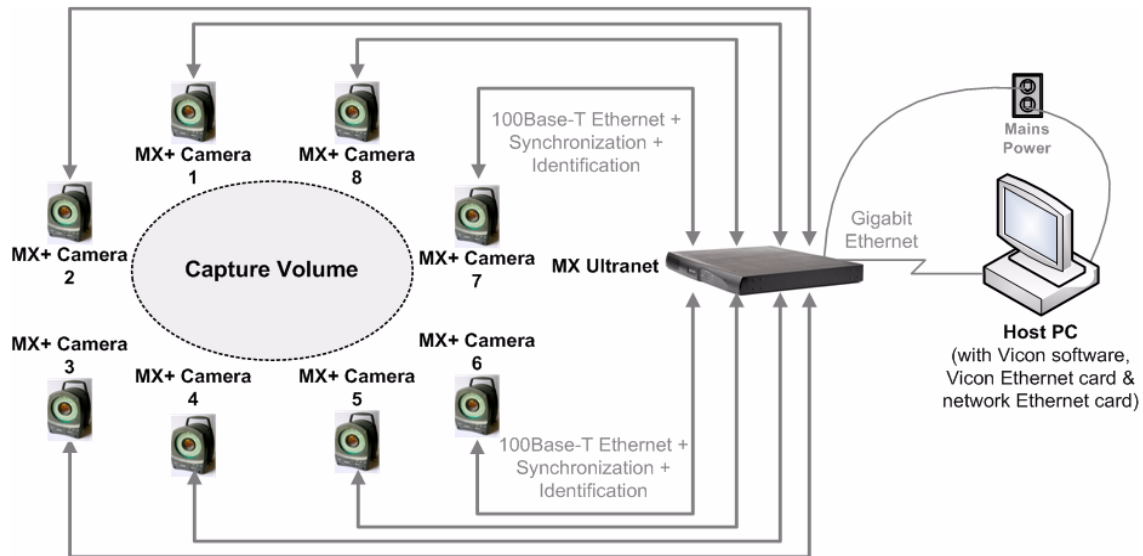


Figure 25: Basic Vicon MX configuration.

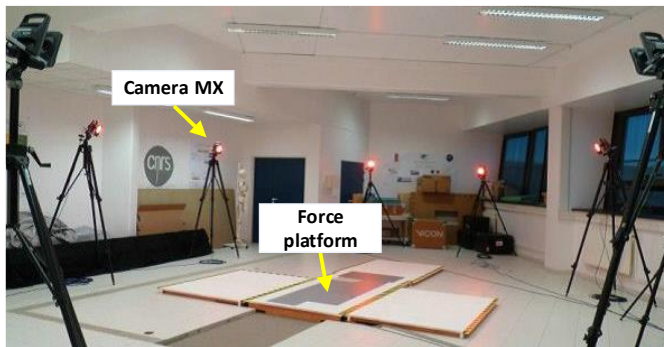


Figure 26: The experimental setup.

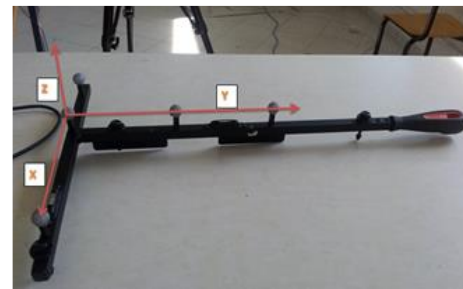


Figure 27: Calibration wand of the Vicon system.

The recruited subject is 1.75 m tall and has a mass of 70 kg. As Figure 28 depicts, a set of 14 markers are placed on each limb. Note that R and L prefix are used to distinguish, respectively, the markers of the right and left limbs. For example, at the right side: i) The pelvis has 3 markers (RPSI, RILC and RASI), ii) The thigh includes 4 markers (RTHIANT, RTHINT, RTHIPOS and RTHIEXT), iii) The leg segment has 4 markers (RLEGANT, RLEGINT, RLEGPOS, RLEGEXT), and finally 3 markers are attached to the foot (RTOE, RFOOT and RHEEL). Note that these reflective markers are placed in anatomical locations that have less important soft tissue artefact, i.e., the movement of the skin relative to the bones [108].

Setting the global coordinate system in the capture scene requires the use of a calibration wand (see Figure 27). In fact, the motion capture begins with a static calibration process in which the calibration tool is placed in a user defined position. Thereby, the position of each marker is given relative to the defined reference frame. The known location of each marker on the limb, allows the post processing of the acquired data as a function of time to determine the joint trajectories.

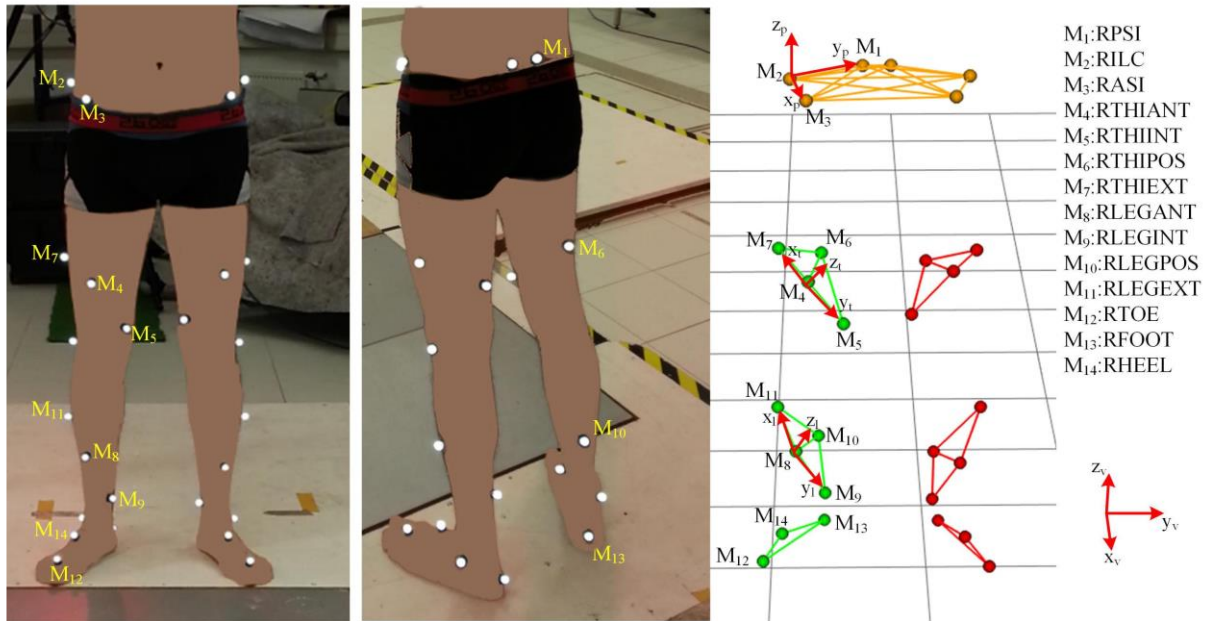


Figure 28: Marker placement model.

At the beginning of the performance, the candidate was asked to perform 4 minutes of free walking along the captured walkway. Then a static trial (i.e., motionless subject) is recorded, in fact a full view of all markers is required by the Nexus software in order to identify and label each marker. Hereafter, to locate joint centers, the candidate achieved 10 cycles of flexion/extension of each joint of the lower limbs resulting in 6 motion trials. These motions are in close angular ranges to those occurring during a normal walking (see Table 1). Finally, 6 walking trials are achieved and the one having a mean performance is selected.

Table 1: Sagittal angular range of motion during flexion/extension motion trials [107].

	Hip joint	Knee joint	Ankle joint
Flexion (dorsiflexion)	30	50	15
Extension (plantarflexion)	-20	10	-10

2.2.2. Data analysis

2.2.2.1. Kinematic data

The Nexus software allows us to get the markers' trajectories over time. Further computing and analysis were achieved using Matlab software (MathWorks, Inc., Natick, USA). By examining the flexion/extension motion trials, the first step of the post-processing is to locate the center of rotation (CoR) of the hip, knee and ankle joints. Various approaches have been developed to identify the CoR of the hip joint known as the hip joint center (HJC). These approaches are

divided into two groups: predictive approaches [110][111] and functional methods [112][113][114]. The predictive approaches compute the HJC by relying on the position of palpated anatomical landmarks, and regression equations obtained from medical imaging or cadaveric studies [115][116], i.e., the joint center is an empirical relation between bone landmarks. In contrast, functional methods use kinematic and geometric proprieties to locate the CoR between the pelvis and the thigh. Such methods are of two types: sphere fitting methods and transformation techniques [112]. The first method fits the trajectory of a marker on the thigh to a sphere, consequently the sphere's center is the CoR. Here, it is essential to apply a transformation from a global frame to a pelvic local frame, in order to write the motion of a thigh marker in relation to the pelvis. Thereby, the path of such marker will describe the surface of a sphere. To fit a cluster of points to a sphere, several optimization procedures have been proposed: geometric, algebraic, bias compensated algebraic and Pratt sphere fit methods [112][117]. The second type (transformation techniques) involves the determination of transformations between local frames attached to the moving segments and a global coordinate system. Here the CoR is viewed as the point of this rigid transformation. To get this point, different methods have been developed: the center transformation technique, the Holzreiter approach, the helical pivot technique, the Schwartz transformation techniques, the minimal amplitude point method, Stoddart approach, and the SCoRE method [112].

The superiority of the sphere fitting functional methods is confirmed for healthy subjects in [115] and [116]. Furthermore, it is recommended by the International Society of Biomechanics [118] and its effectiveness and accuracy is confirmed in several works [112][113][119]. Consequently, the sphere fit method is selected for HJC identification.

To illustrate how the functional method is implemented, let's consider the case of the right HJC. Three markers (M_1 , M_2 and M_3) are placed on the pelvis to form a local coordinate system $\{F_p\}$ centered at the marker M_2 (see Figure 28). The homogenous transformation matrix pT_v given by (1) yields the position of any marker attached to the hip, in relation to the local reference frame $\{F_p\}$.

$${}^pT_v = \begin{bmatrix} {}^vR_p^{-1} & -({}^vR_p)^{-1} \cdot M_2 \\ 000 & 1 \end{bmatrix} \mid {}^vR_p = \begin{bmatrix} x_p & y_p & z_p \end{bmatrix} \quad (1)$$

Where x_p , y_p and z_p are the coordinates of $\{F_p\}$ frame axes and M_2 is the coordinates of its origin.

During the hip flexion/extension tests, when we apply the rigid transformation pT_v , the paths of markers M_4 and M_6 yield the surface of a sphere centered at the HJC (see Figure 29).

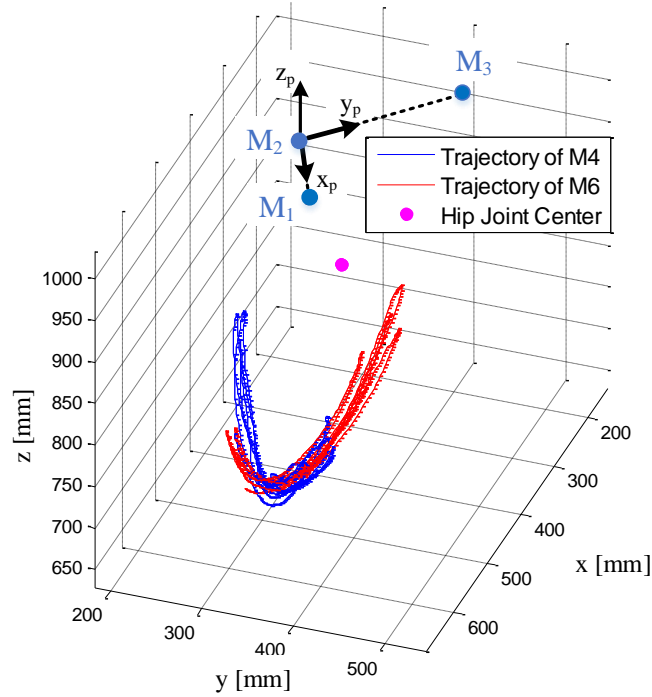


Figure 29: Identification of the right Hip Joint Center using geometric sphere fitting.

Three different sphere fitting algorithms, i.e., geometric, algebraic and Pratt methods, are implemented. Eq (2) describes the objective function to be minimized for each method [112]:

$$\begin{aligned}
 & \sum_{i=1}^n (\|M_i - C_{hip}\| - R)^2 : \text{Geometric} \\
 & \sum_{i=1}^n (\|M_i - C_{hip}\|^2 - R^2)^2 : \text{Algebraic} \\
 & \frac{1}{R^2} \times \sum_{i=1}^n (\|M_i - C_{hip}\|^2 - R^2)^2 : \text{Pratt}
 \end{aligned} \tag{2}$$

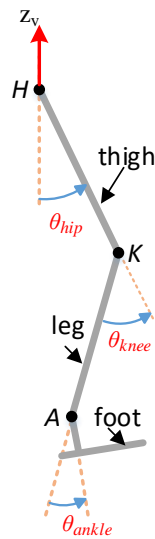
Such that: $R = (1/n) \times \sum_{i=1}^n \|M_i - C_{hip}\|$

Where C_{hip} is the center of the sphere described by the motion of the marker M_i . Here, The HJC is the mean value between the centers obtained from M_4 and M_6 . Table 2 shows the computed coordinates of the right HJC in the local pelvis frame $\{F_p\}$. All values are close, this remark is also confirmed in [112]. Therefore, all sphere fit technics yield comparable results and any one may be chosen.

Table 2: Local coordinates of the right Hip Joint Center using different algorithms.

	x coordinate [mm]	y coordinate [mm]	z coordinate [mm]	Norm [mm]
Geometric	99.13	31.8	-119.2	158.13
Algebraic	98.64	30.40	-120.11	158.12
Pratt	98.87	31.08	-119.58	158.23

During the walk motion trial, the global position of the HJC denoted H (see Figure 30) is computed by mapping the C_{hip} from the local frame $\{F_p\}$ to the global frame $\{F_v\}$: $H = {}^vT_p \cdot C_{hip}$. For the knee and ankle joints, in contrast to the methods presented in [120] and [121], which estimate the CoR as a mean position between two markers, we used the sphere fitting method to locate the CoR. Since the knee and ankle joints are revolute joints, the knee joint center (KJC) and the ankle joint center (AJC) may be computed in a similar way as the HJC. In fact, for the knee, a reference frame $\{F_t\}$ is defined by markers M_4 , M_5 , and M_7 , and the KJC is identified by fitting trajectories of markers M_8 and M_9 . Considering the ankle, a reference frame $\{F_l\}$ is defined by markers M_8 , M_9 and M_{10} , and the AJC is located by fitting paths of markers M_{13} and M_{14} .

**Figure 30: Angle definitions for the lower limb.**

During the walk motion testing, once all the global CoRs (H , K and A) are computed as a function of time, the angles are defined using Eq (3) or Figure 30.

$$\begin{aligned}
 \theta_{hip} &= \angle(-Z_v, HK) \\
 \theta_{knee} &= \angle(KA, HK) \\
 \theta_{ankle} &= \angle(KA, M_{13}M_{12}) - (\pi / 2)
 \end{aligned} \tag{3}$$

The resulting angular trajectories are shown in Figure 31. Hereafter, curves were smoothed using a 5th order lowpass digital Butterworth filter. The selected frame rate of cameras is 100 fps, therefore, based on Nyquist theorem the cut-off frequency must be less one half of the sampling frequency, which is 50 Hz. Besides, curves were cut for one gait cycle. Lastly, the duration is normalized to 100% of one GC, yielding the trajectories of Figure 32. Note that the obtained gait kinematics is consistent with common gait databases [20][122]. In addition, the vertical displacement of the pelvis is obtained based on the vertical position of any marker that belongs to the pelvis, this curve is shifted by its mean value (Figure 33).

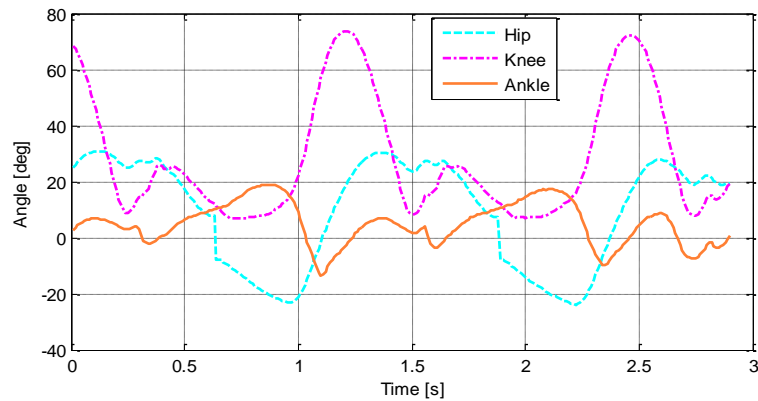


Figure 31: Angular trajectories of the lower limb in function of time.

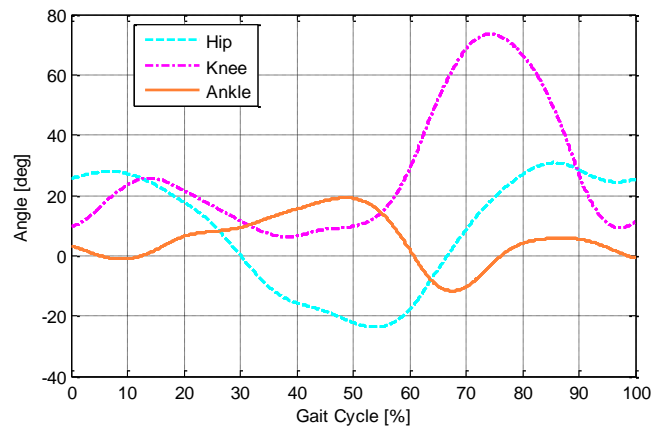


Figure 32: Angular trajectories of the lower limb against percentage of one gait cycle.

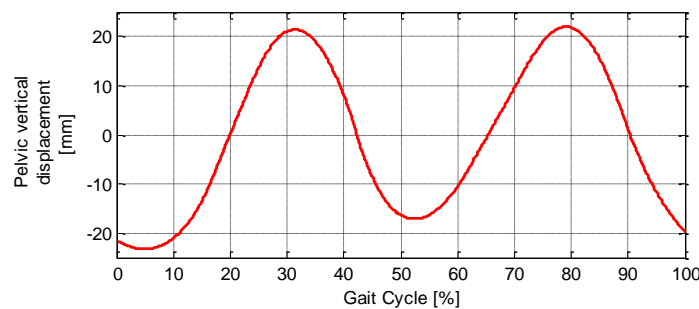


Figure 33: Vertical displacement of the pelvis against percentage of one gait cycle.

2.2.2.2. Ground reaction force

The ground reaction force is recorded using the force platform running at a frequency of 1000 Hz. The platform gives the reaction force in the form of a 3 dimensional vector. Figure 34 shows the graph of components included in the sagittal plane of both feet: the vertical reaction (R_v) and the anterior-posterior reaction (R_{ap}), which are positive when directions are upward and forward, respectively. During the stance phase, the support of the body weight is marked with a positive R_v showing a double hump shape (Figure 34). The first and second peaks describe, respectively, upward acceleration and deceleration of body's CoM. The R_{ap} is negative during the first half of the stance phase resulting in braking and positive for the second half describing propulsion. Obviously, both components (R_v and R_{ap}) are null when the foot is swinging. Note that the position of the Center of Pressure (CoP) for each foot can be provided, which is the location of the point of application of the resultant force on the ground.

Recorded signals are smoothed using a 5th order lowpass digital Butterworth filter with a cut-off frequency of 500 Hz. Selecting a one GC, the time axis was scaled to 100% and forces were normalized in relation to the body weight [123][124]. Figure 35 visualizes the new curves for one foot. To obtain those of the other foot, the first must be shifted by a phase of a half cycle.

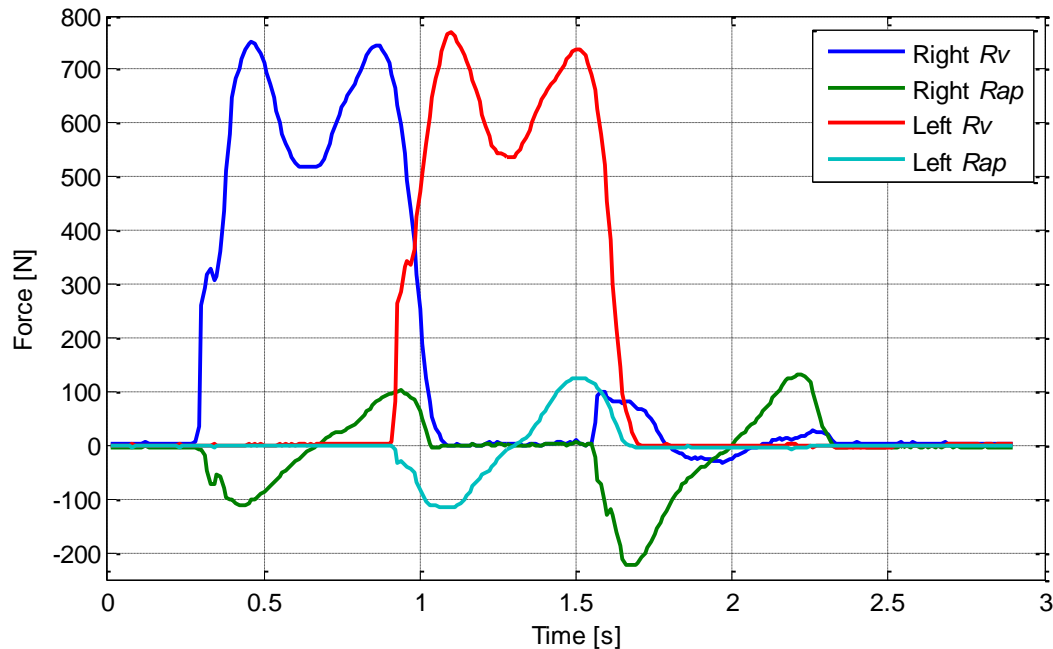


Figure 34: Ground reaction of both feet in function of time.

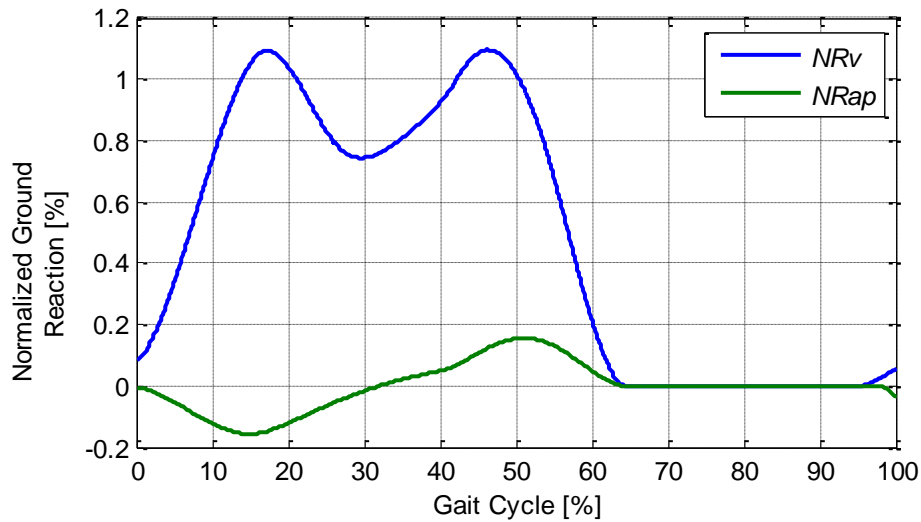


Figure 35: Normalized ground reaction during a gait cycle.

Conclusion:

The conducted analysis of overground walking yielded the joint trajectories of the lower extremity, in addition to the reaction forces between the feet and the ground. Further, it developed our understanding of the gait stepping movement. The obtained kinematics can be seen as a target performance of the CDLT. Moreover, since our main objective is to reproduce the gait pattern, the kinematic and dynamic data will be employed to achieve an inverse dynamic simulation of a treadmill walking within the CDLT.

3. Inverse Dynamic Simulation of the Rehabilitation Machine

Summary:

The dynamic study aims at solving the inverse dynamic problem of a partially unloaded person during a treadmill walking. The analysis is based on data obtained from the gait experiment. The human body is modeled as a multi-segment articulated mechanism. The target performance is the kinematics of the recorded normal gait, which is used as the motion input for the dynamic model. A free-body diagram is used to show all exerting internal and external forces. Both, the measured ground reaction and the unloading force, are considered as external forces applied to the body. The dynamic simulation is carried out using two methods: using Newton-Euler equations and using a Matlab SimMechanics model. The results of the dynamic simulation are the required actuation wrench to be produced by the cable robot in order to drive the leg during a treadmill ambulation.

3.1. Dynamic Modeling

3.1.1. Human body modeling.

As depicted in Figure 36, the body is represented by a planar four-link mechanism: the upper body (known also as head, arms and trunk (HAT) segment [125]), the thigh, the leg and the foot. The linkage between the trunk and the fixed frame is modeled as a prismatic joint. For the hip, knee and ankle, they are modeled as revolute joints. Thus the body is characterized by 4 DOF. The angles are zero when the lower limb is in a vertical posture. The flexion and extension correspond, respectively, to positive and negative values of the angles. It is worth mentioning that the proposed model is based on the following assumptions:

- All the segments are considered rigid
- All the joints are considered frictionless [125], The joints of the lower extremity are passive, thus muscles contribution is ignored which can be viewed as the most disadvantageous case,
- No relative motion between the orthosis and the leg,
- Lower limb kinematics are the same as during normal walking. Further, even when the ankle joint is not actuated, the same general trajectory is observed [126].

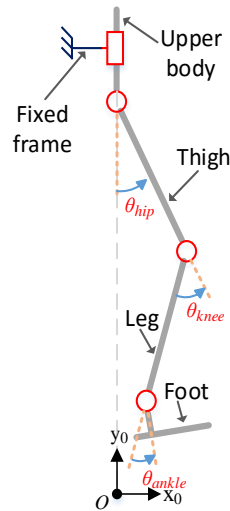


Figure 36: Human body 4 segment kinematic model for treadmill walking.

For the treadmill walking, Figure 37 shows the external loads applied on the body:

- F_{un} , the unloading force produced by the springs included in the BWS and applied at the upper body through the harness system,
- R_{gr} , the ground reaction force applied at the sole of the foot,
- F_{lr} , the footlifter force acting between the leg's orthosis and the foot in order to stabilize the ankle joint during the swing phase of the GC,
- The resultant force and moment (F_{cdr} and M_{cdr}), which are the actuation unknowns to be generated by the cable robot in order to achieve walking.

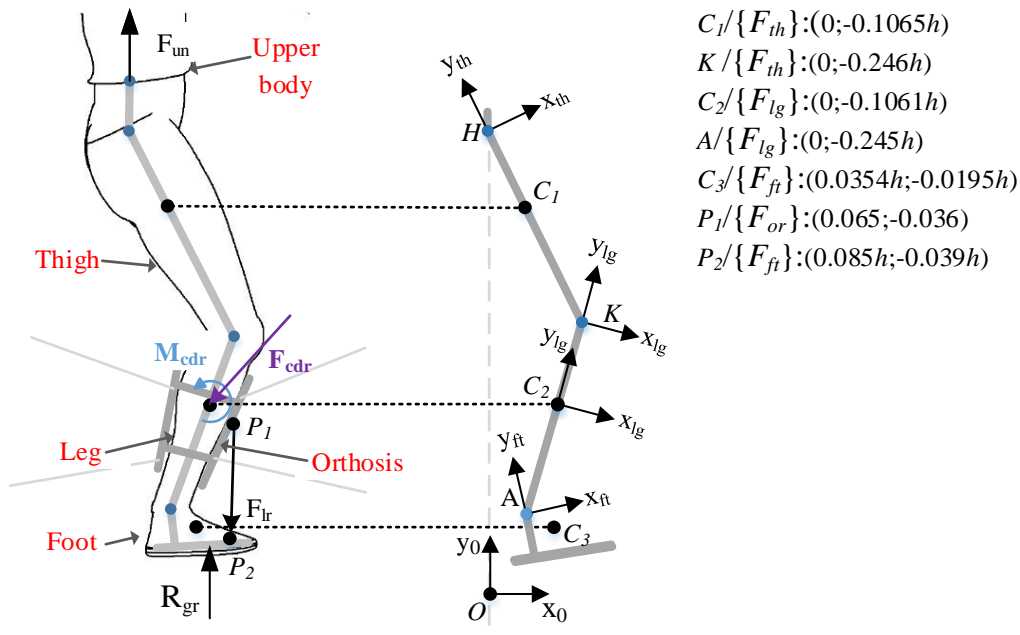


Figure 37: External loads acting on the lower limb and kinematic specifications.

To describe the kinematics of the lower limb, 5 frames are defined (see Figure 37):

- A global reference frame $\{F_0\}=\{O, x_0, y_0\}$ is placed on the treadmill such that the HJC H and the point O are vertically aligned.
- A frame $\{F_{th}\}=\{H, x_{th}, y_{th}\}$ is attached to the thigh segment and centered at the HJC H .
- A frame $\{F_{lg}\}=\{K, x_{lg}, y_{lg}\}$ is attached to the leg segment and centered at the KJC K .
- A frame $\{F_{or}\}=\{C_2, x_{lg}, y_{lg}\}$ is centered at the leg's CoM C_2 , in which F_{cdr} and M_{cdr} are evaluated.
- A frame $\{F_{ft}\}=\{A, x_{ft}, y_{ft}\}$ is attached to the foot segment and centered at the AJC A .

Here, C_1 , C_2 and C_3 are the CoMs of the thigh, the leg and the foot, respectively. P_1 and P_2 are the placement points of the footlifter.

3.1.2. Inertias and geometry of the different segments

Based on anthropometric measurements, the geometric and inertia proprieties of body segments can be written as a fraction of the mass and/or the height of the body. Hereby, reference [127] is used to get the body anthropometric specifications. Segment lengths of the human body are shown in Figure 38 as a percentage of the body height.

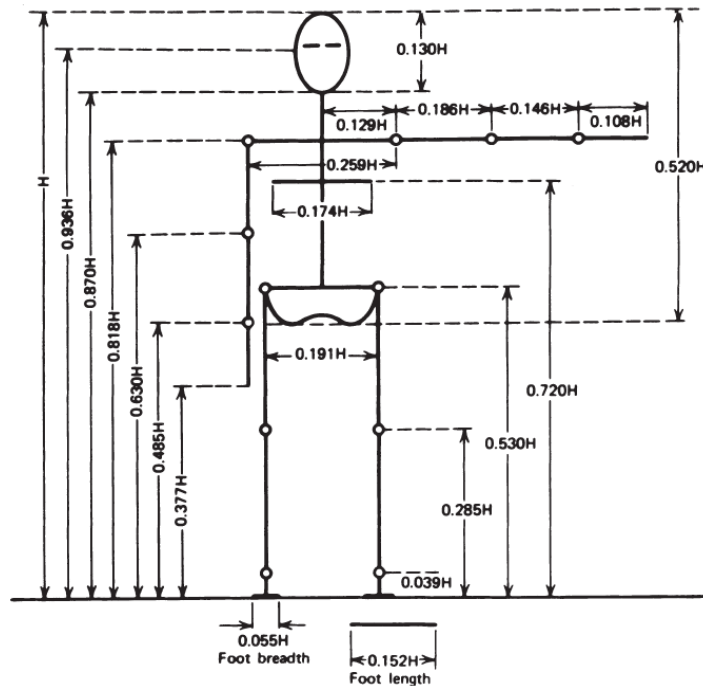


Figure 38: Body segment lengths expressed as portion of the body height [127].

Based on Appendix 1, coordinates of C_1 , K , C_2 , A , C_3 and P_2 are defined in relation to their local frames as a fraction of the body height h (see Figure 37). In addition, the mass of segments are given in the first row of Table 3 as a percentage of the total body mass.

Table 3: Inertia and length data [127].

	Upper body	thigh	Leg	foot
Mass (m) [%]	67.8	10	4.65	1.45
Radius of Gyration (RoG) [%]	**	32.3	30.2	47.5
Length (L) [m]	**	$0.245h$	$0.246h$	$0.085h$

The moments of inertia of the different segments are computed based on the following equation:

$$I = m \times (RoG \times L)^2 \quad (4)$$

Where m , RoG and L , are the mass, the radius of gyration, and the length of the involved segment, respectively [127]. RoG of the lower limb segments are given in the second row of Table 3 as a percentage of the segment length L . Note that the length of the foot segment is taken from the AJC to the midpoint between the 1st and 5th metatarsal heads [128]. For more details on anthropometric data, the reader is referred to [127] and [128].

The inertia of the orthosis is: a mass of 1.2 kg and a moment of inertia of 0.0153 kg.m² computed at the leg's CoM C_2 (see Figure 37).

3.1.3. Free-body diagram and Newton-Euler equations

The fundamental step in analyzing the dynamic behavior of a mechanical system is to draw a free-body diagram of each segment, showing inter-segmental and external forces [17][129]. In our case, the entire body is subdivided into 4 rigid bodies. Figure 39 depicts exerting forces on the upper body, the thigh, the leg and the foot. One shall note that the equilibrium equations are written in relation to the CoM of each segment, thus moments of the weight forces are zero. Furthermore, the transmitted torque from one segment to another is regarded as zero since the joints are assumed to be passive.

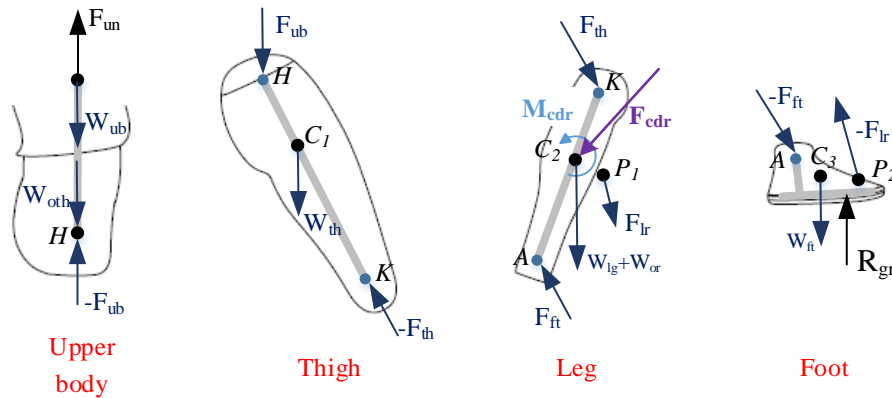


Figure 39: Free-body diagrams of body segments

The dynamic model of the body segments can be obtained through Newton law applied to each segment.

3.1.3.1. The upper body

During the treadmill walking, the upper body is assumed to be translating along the vertical direction. Therefore, the dynamic model is restricted to only the vertical forces:

$$F_{un} - (1/\alpha) \cdot F_{ub} + W_{ub} + W_{oth} = (m_{ub} + m_{th}) \cdot a_{ub} \quad (5)$$

where W_{ub} , m_{ub} and a_{ub} are, respectively, the weight force, the mass and the acceleration of the upper body. To add the effect of the opposite limb, the thigh mass m_{th} and weight W_{oth} should be added. Here, we consider that the opposite leg and foot are balanced by the opposite orthosis. The unloading force F_{un} applied by the suspension system on the upper body through the harness is:

$$F_{uny} = (k/2) \cdot (y_0 + \Delta y/2) \text{ such that } y_0 = (BWS \cdot g \cdot m) / (k/2) \quad (6)$$

$k=4 Nm$ is the total springs constant, $g= 9.81 m/s^2$ is the gravity acceleration, m is the body mass, and the instantaneous position Δy follows the pelvic displacement curve (see Figure 33). The springs offset y_0 is calculated based on the desired amount of unloading BWS , therefore the springs pre-tension force is the mean value of unloading.

The term $(1/\alpha) \cdot F_{ub}$ is the force transmitted from the upper body segment to the current limb. α is a factor that defines the participation of one limb to support the body weight: α is equal to 1 during single limb stance and zero during swing time. Throughout double support phases it varies from 0 to 1, and is calculated based on the vertical normalized ground reaction NRv of the two foot: $\alpha = (Right\ NRv + Left\ NRv) / Right\ NRv$. Figure 40 shows the change of this factor along with the variation of NRv of the feet over one GC.

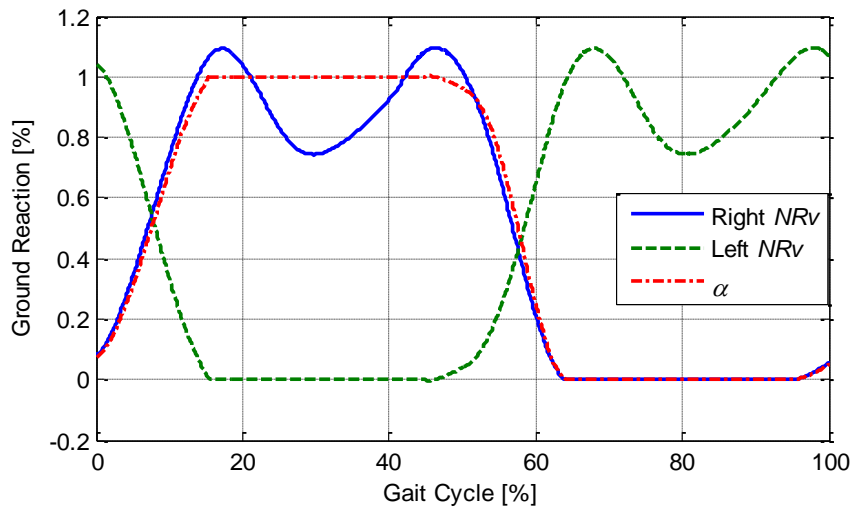


Figure 40: Curve of α coefficient.

3.1.3.2. The thigh

The dynamic model of the thigh segment is given as follows:

$$\begin{aligned} F_{ub} - F_{th} + W_{th} &= m_{th} \cdot a_{th} \\ M_{ub} - M_{th} &= I_{th} \cdot \dot{\omega}_{th} \end{aligned} \quad (7)$$

where W_{th} , m_{th} , I_{th} , a_{th} and $\dot{\omega}_{th}$ are, respectively, the weight, the mass, the moment of inertia, the linear acceleration, and the angular acceleration of the thigh segment, written in relation to its CoM. F_{th} is the force exerted by the thigh on the leg.

3.1.3.3. The foot

For the foot segment, we have the following equations:

$$\begin{aligned} -F_{ft} - F_{lr} + R_{gr} + W_{ft} &= m_{ft} \cdot a_{ft} \\ -M_{ft} - M_{lr} + M_{gr} &= I_{ft} \cdot \dot{\omega}_{ft} \end{aligned} \quad (8)$$

here W_{ft} , m_{ft} , I_{ft} , a_{ft} and $\dot{\omega}_{ft}$ are, respectively, the weight, the mass, the moment of inertia, the linear acceleration, and the angular acceleration of the foot segment, written in relation to its CoM. The F_{ft} force is the force between the foot and the leg.

The ground force R_{gr} is obtained by multiplying the normalized ground reaction (see Figure 35) and the new body weight. This latter is computed by subtracting the unloading force from the body weight:

$$R_{gr} = W_n \cdot NR_{gr} \text{ such that } W_n = m \cdot g - F_{uny} \text{ and } NR_{gr} = (NR_v \quad NR_{ap})^T \quad (9)$$

F_{lr} is the footlifter force involved to stabilize the ankle joint during the swing period.

3.1.3.4. The leg

For the leg segment, the equilibrium is marked by the term of the actuation wrench F_{cdr} and M_{cdr} :

$$\begin{aligned} F_{th} + F_{ft} + W_{lg} + W_{or} + F_{lr} + F_{cdr} &= (m_{lg} + m_{or}) \cdot a_{lg} \\ M_{th} + M_{ft} + M_{lr} + M_{cdr} &= (I_{lg} + I_{or}) \cdot \dot{\omega}_{lg} \end{aligned} \quad (10)$$

Later, the defined dynamic data and equations will be used to solve the inverse dynamic problem of the proposed machine.

3.2. Inverse Dynamic Simulation

In this section, we describe the way in which the inverse dynamic model is solved. First, relying on Newton-Euler equations, and secondly by mean of a Matlab SimMechanics model. Results of the dynamic simulation employing the two mentioned methods are presented.

3.2.1. Solving the Newton-Euler equations

The inverse dynamic problem consists in computing the required forces to cause a desired motion of a mechanism having specific inertias. In gait simulation, the traditional Newton-Euler approach is widely adopted to get the actuation forces capable of driving the lower limb during ambulation [125]. The investigated Newton-Euler equations in the first section are solved recursively to get the required forces.

Here, our goal is to get the wrench applied by the cable robot to the leg. For that purpose, Newton-Euler equations are solved as follows:

Eq (5) is solved for a given amount of unloading *BWS* to get the upper body force F_{ub} :

$$F_{uby} = \alpha \cdot (- (m_{ub} + m_{oth}) \cdot g + K \cdot (\frac{m \cdot g \cdot BWS}{K} + \Delta y / 2) - (m_{ub} + m_{oth}) \cdot a_{uby}) \quad (11)$$

Then Eq (7) is used:

$$\begin{aligned} F_{ubx} - F_{thx} &= m_{th} \cdot a_{thx} \\ F_{uby} - F_{thy} - m_{th} \cdot g &= m_{th} \cdot a_{thy} \\ C_1 H \times F_{ub} - C_1 K \times F_{th} &= I_{th} \cdot \dot{\omega}_{th} \end{aligned} \quad (12)$$

To determine F_{th} the inter-segmental force, we solve the Eq (12), which is made of 3 linear equations and has 3 unknowns: F_{thx} , F_{thy} and F_{ubx} . The expressions of the unknowns F_{thx} and F_{thy} are given in Appendix 2.

The analysis of the foot equilibrium is then discussed depending on the GC periods. First, during the stance phase, only Eq (8) is taken into account. Further, the F_{lr} force is eliminated since the foot is balanced by the ground. Therefore, the F_{ft} force is calculated as follows:

$$F_{ft} = -m_{ft} \cdot a_{ft} + (m \cdot g - F_{uny}) \cdot NR_{gr} - m_{ft} \cdot g \cdot y_0 \quad (13)$$

Second, throughout the swing period, the R_{gr} force is zero and the F_{lr} is active. Therefore Eq (8) becomes:

$$\begin{aligned} -F_{ft} - F_{lr} + W_{ft} &= m_{ft} \cdot a_{ft} \quad \text{such that } F_{lr} = \|F_{lr}\| \cdot (P_1 P_2 / \|P_1 P_2\|) \\ -C_3 A \times F_{ft} - C_3 P_2 \times F_{lr} &= I_{ft} \cdot \dot{\omega}_{ft} \end{aligned} \quad (14)$$

to a desired unloading amount “BWS” using Eq (6). Knowing the position of placement points P_1 and P_2 , The footlifter force F_{lr} is computed using Eq (14). Based on the normalized ground reaction, the “ R_{gr} ” force is computed using Eq (9) and it is applied on the foot segment. Lastly, by inputting the curve of the α factor (Figure 40), the action of the upper body force F_{ub} is computed inside the block “Upper body”.

A “3 DOF planar joint” placed at the leg CoM is used to simulate the required trajectory. This custom joint has two linear and one rotational DOFs. The data of the block “Lower limb kinematics” are fed to the block “leg pose trajectory”, in which the leg trajectory is computed and then sent to the leg segment for actuation.

By running the simulation of the developed model, the actuation wrench (F_{cdr} , M_{cdr}) is computed “3 DOF planar joint” block and the information is collected from the block “Actuation wrench (F_{cdr} , M_{cdr})”.

3.3. Case Study

It is worth mentioning that for gait training, two scenarios are involved: the off-ground and the on-ground walking. The first happens at the beginning of a training session when the patient is lifted from the wheelchair and he is maintained off the ground in an upright posture. Some cycles of an off-ground walking are achieved, in order to check if the setup procedure is properly performed, and also for familiarization with gait training. The second case occurs when the vertical position of the patient is lowered until touching the treadmill and the desired amount of unloading is reached.

For illustration, we consider the example of a body having a mass $m=100$ kg and a tall $h=1.7$ m. Based on anthropometric specifications presented in Section 3.1.2., all the geometric and inertia data are computed and summarized in Table 4.

Table 4: Dynamic simulation data

h [m]	m_{ub} [kg]	m_{th} [kg]	m_{lg} [kg]	m_{ft} [kg]	m_{or} [kg]	BWS [%]
1.7	67.8	10	4.65	1.45	1.2	50
I_{th} [kg.m ²]	I_{lg} [kg.m ²]	I_{ft} [kg.m ²]	I_{or} [kg.m ²]	k [kN/m]	t_{gc} [s]	
0.181	0.0742	0.0068	0.0153	4	1.4	
g [m/s ²]	C_1 [m; m]	C_2 [m; m]	C_3 [m; m]	P_1 [m; m]	P_2 [m; m]	
9.81	(0 ; -0.1803)	(0 ; -0.1811)	(0.0613 ; -0.0331)	(0.065; -0.036)	(0.1445; -0.0663)	

During the on-ground simulation, curves of different external and internal forces are presented. The unloading force F_{un} (Figure 42) varies inversely proportional to the pelvic displacement (Figure 33) and it oscillates around the desired unloading force (490.5 N i.e. $100 \times 50\% \times 9.81$). The upper body force F_{ub} (Figure 43) is the force transmitted from the upper body to the current limb, this force shows an upside down double hump shape similar to the measured vertical reaction R_v of the ground (Figure 35). The ground reaction force R_{gr} (Figure 44) is obtained by multiplying the normalized ground reaction and the new body weight, this latter is equal to the patient weight minus the unloading amount, which is $(100 - 100 \times 50\%) \times 9.81 = 490.5\text{N}$. The foot force F_{ft} (Figure 45) has a similar shape as the one for R_{gr} . The Thigh force F_{th} (Figure 46) varies inversely proportional to the foot force. For the footlifter force F_{lr} , which is active only during the swing period (Figure 47), its effect is quite small and can be neglected.

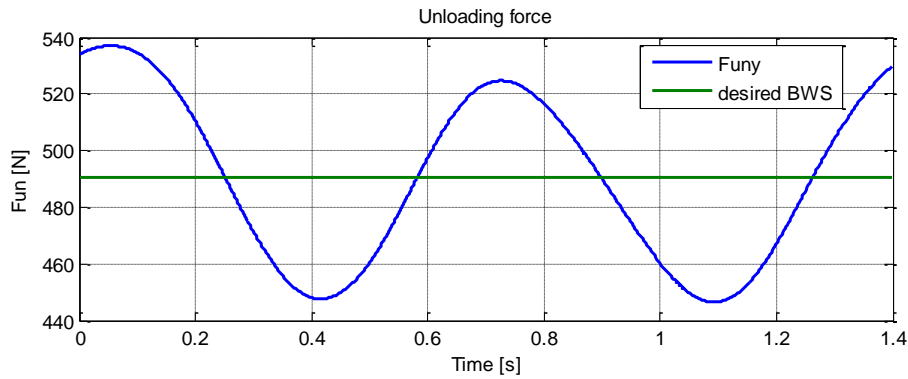


Figure 42: Unloading force F_{un} during the on-ground walking.

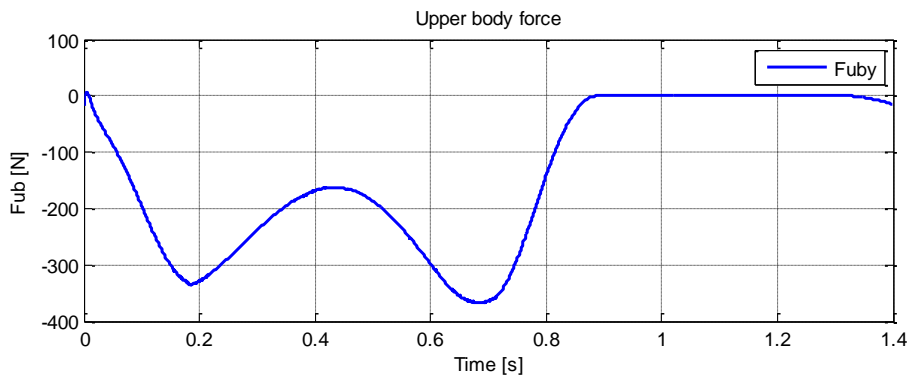


Figure 43: Upper body force F_{ub} during the on-ground walking.

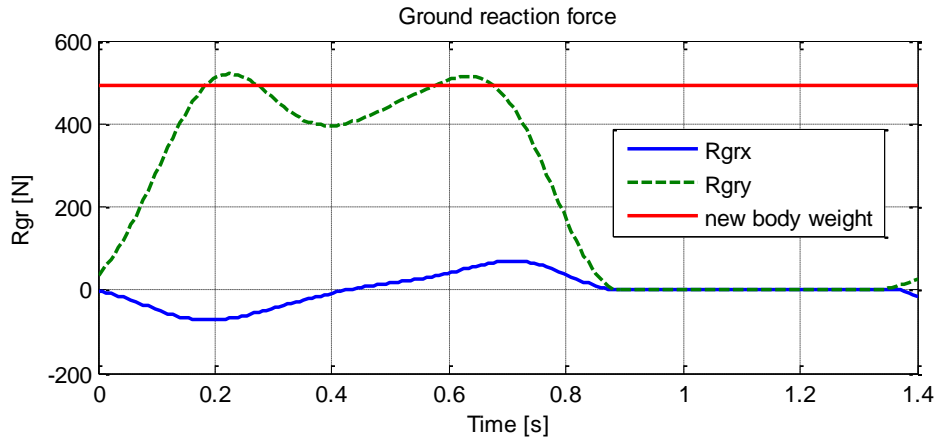


Figure 44: Ground reaction force R_{gr} during the on-ground walking.

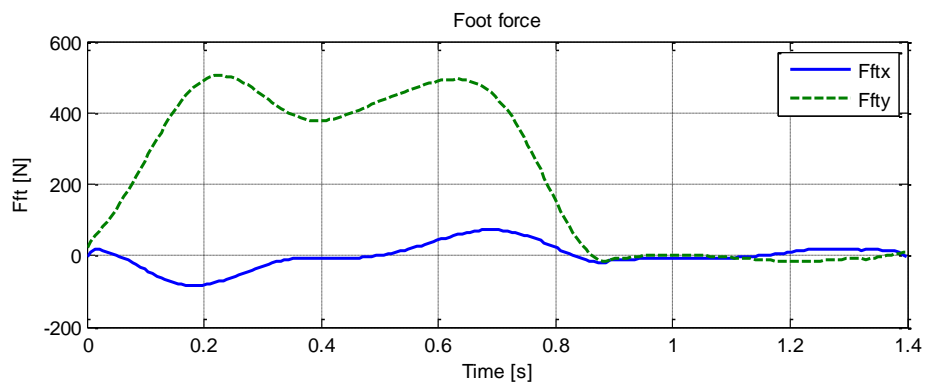


Figure 45: Foot force F_{ft} during the on-ground walking.

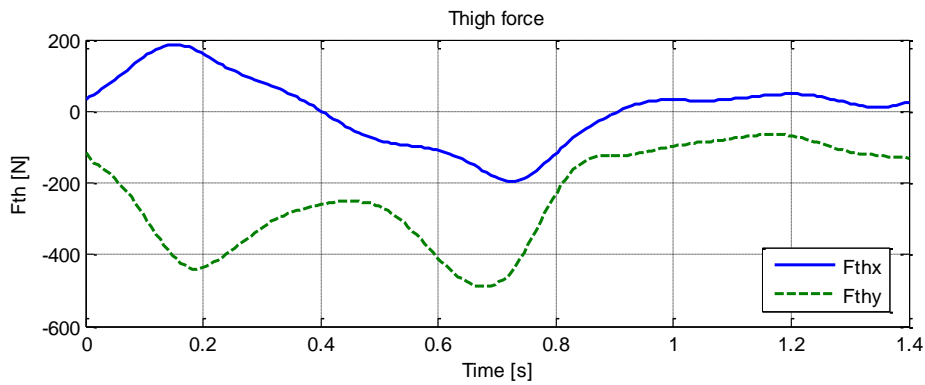


Figure 46: Thigh force F_{th} during the on-ground walking.

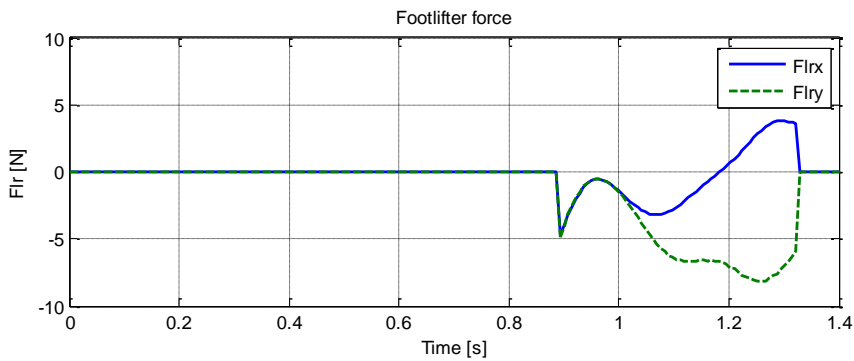


Figure 47: Footlifter force F_{lr} during the on-ground walking.

For the two case studies, Figure 48 and Figure 49 show the curves of the actuation wrench using the two solving approaches, i.e., Newton-Euler equations and SimMechanics model. Results of both approaches are consistent, only few differences between the two curves exist. This observation confirms the validity of the investigated dynamic study.

When examining the differences between the on-ground (Figure 48) and the off-ground (Figure 49) cases, one can note that, over the swing phase, from 0.88s to 1.32s approximately, curves have almost the same behavior since in both simulations the limb is above the ground. The pelvic motion, which is only active for the on-ground case, induces a small difference between the two curves. Throughout the stance period, when comparing both actuation moment M_{cdr} , it is clear that the required torque is higher for the on-ground walking. This fact is due to the need to resist the effect of the ground reaction. Moreover, for the off-ground case, the F_{cdry} component is always positive over the GC. An upward force is required to maintain the leg in the air.

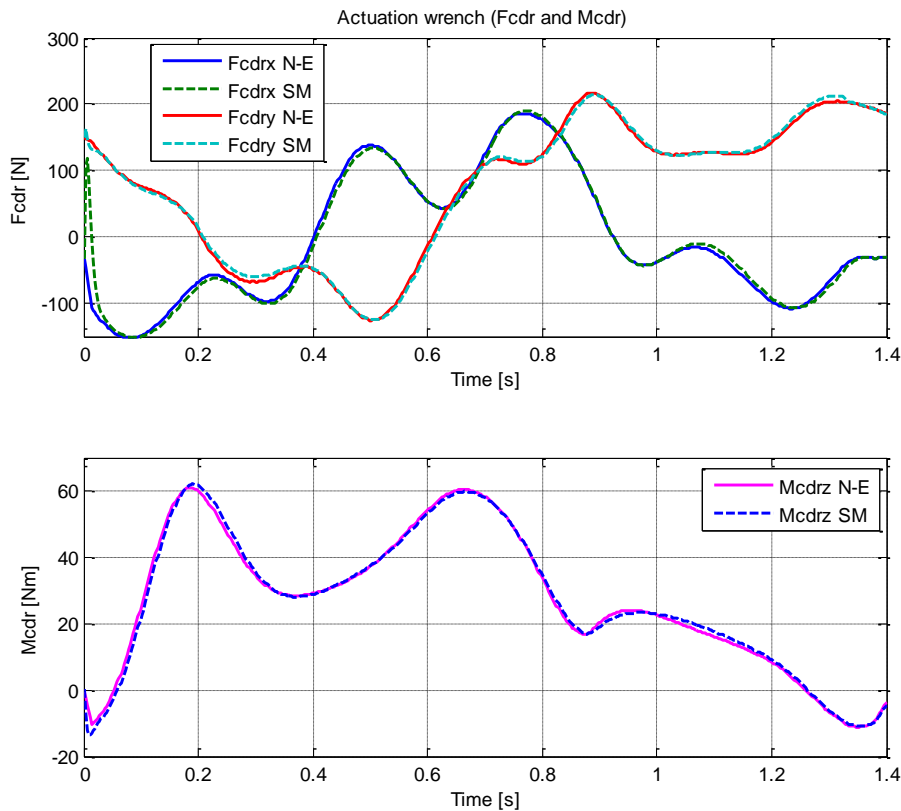


Figure 48: Variation of the actuation wrench (F_{cdr} , M_{cdr}) during the on-ground walking.

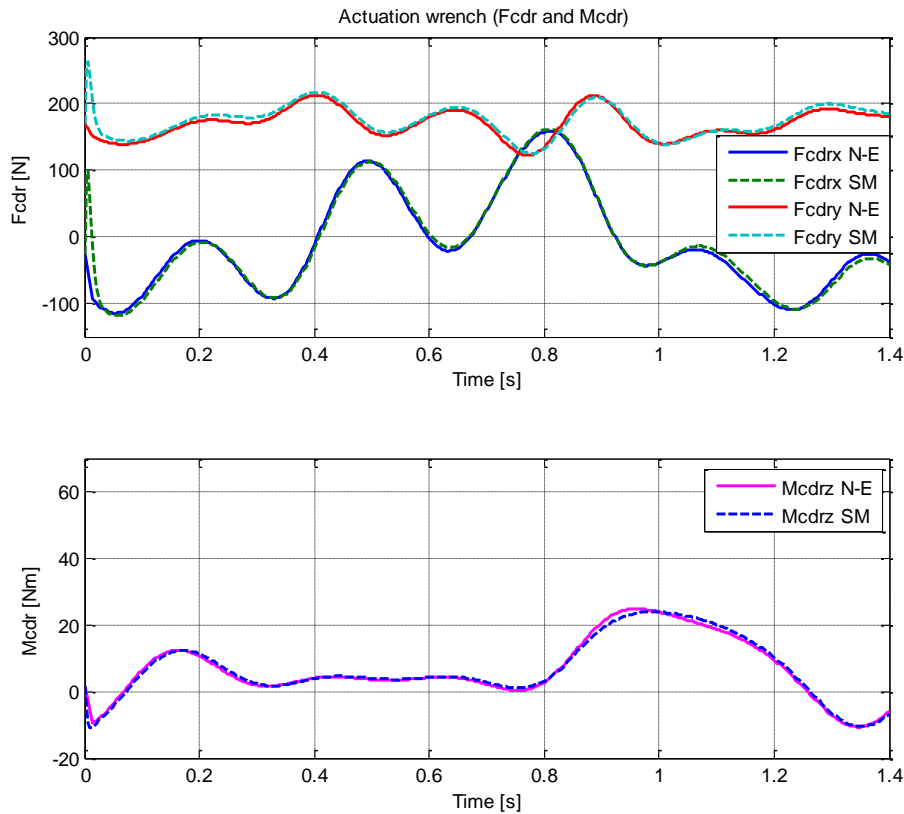


Figure 49: Variation of the actuation wrench (F_{cdr} , M_{cdr}) during the off-ground walking.

Conclusion:

A dynamic analysis of a treadmill walking using the CDLT was investigated in this chapter. The human body was modeled as a 4 segment mechanism. Based on anthropometric data, the inertia and the geometry of the body segments were obtained. Experimental results of Chapter 2 including the gait trajectories and the ground reaction were used as inputs. The unknown of the dynamic problem was the required actuation wrench to drive the lower limb during locomotion. The inverse dynamic problem was solved using Newton-Euler equations and a Matlab SimMechanics model, results were found to be consistent using both methods. The wrench computed in this chapter will be exploited later in Chapter 5 to design the CDLT.

4. Design of Cable-Driven Parallel Manipulators

Summary:

Our gait training machine includes a cable robot to assist the movement of the lower limb. Thus, topics on the design of cable robots are our main interest. In this chapter, we address the problem of designing cable-driven parallel manipulators (CDPMs) for a desired workspace.

Due to the fact that a cable can only exert a pulling force, workspace analysis of CDPMs is mainly limited by the constraint of keeping non-negative tensions in all the cables at all times. The constraint of having both: non-negative and bounded tensions for all the reached poses, defines the so-called Wrench-Feasible Workspace (WFW). For the design of CDPMs, this condition has to be satisfied within the given workspace.

The equilibrium analysis is carried out using the interval analysis method, which is one of the most efficient methods in handling uncertain data. Conversely to classical approaches in which the workspace of a CDPM is viewed as a grid of points, the interval approach allows covering the entire workspace and hence guarantees a singularity free workspace. Based on interval mathematical tools, such as interval arithmetic and interval linear equations, the equilibrium is written in its interval form and then its feasibility is guaranteed.

An interval-analysis based design algorithm of CDPMs is provided; this algorithm is capable of finding all possible sets of solutions for a CDPM structure while guaranteeing the access to a particular workspace with respect to a given external load. The obtained solutions are then analyzed to select the “best” one according to a user defined criterion.

Two examples are selected to show the efficiency of the developed algorithm in solving this complex problem. The first one deals with the design of a planar CDPM and the second one considers a spatial CDPM. In both cases, the algorithm succeeded to find all possible designs from which the designer can select a solution that fits best his application.

While the obtained results using intervals are certified and reliable over all the desired space, the drawback of this approach is that the accuracy of the solutions is sensitive to the intervals overestimation problem. For that, a bisection technique of the prescribed workspace is applied.

One shall note that in our analysis the weight of the cables is neglected. Further, in this chapter, cable interferences are ignored.

4.1. Workspace Analysis of Cable-Driven Parallel Manipulators

In contrast with classical parallel manipulators, cable-driven parallel manipulators CDPMs (Figure 50) substitute rigid links with cables in order to move the end-effector. Based on this particular actuation scheme, a CDPM has a set of benefits mainly light-weight structure, large reachable workspace, low inertia, low cost, and ease of reconfiguration.

A well-known CDPM called the Falcon robot [130], made out of 7 cables, is shown in Figure 50. The main components of a CDPM are the base frame, the mobile platform, the cables connecting the effector to the base in a given number of points, and finally the actuators, which are usually made of winches. Figure 51 visualizes an example of an actuation system, the cable is spooled via a winch coupled to an electric motor, and then is directed to the exit point part through a series of pulleys.

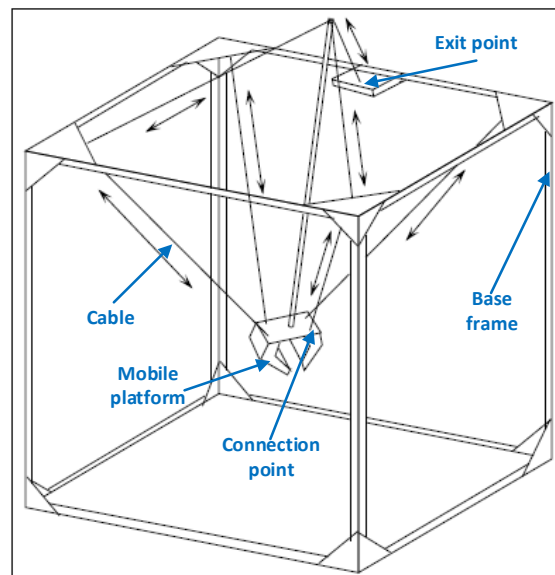


Figure 50: Example of a CDPM: 7 cables Falcon Robot [130].

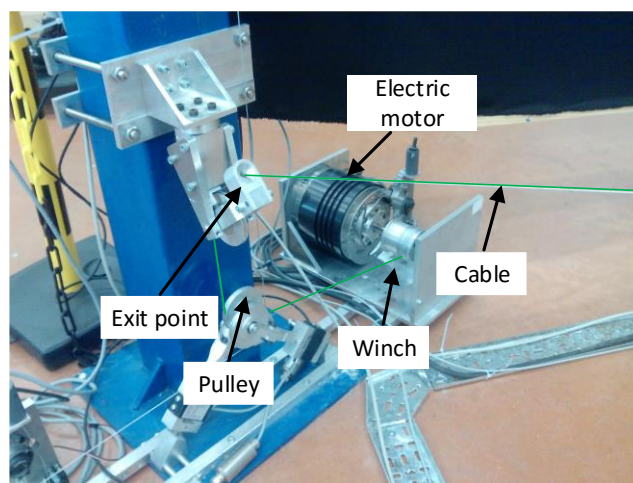


Figure 51: Actuation system of cables [131].

CDPMs are widely used in multiple applications, e.g., rescue, rehabilitation, maintenance (Figure 52(a)), Video recording (Figure 52(b)), high speed manipulator... For more details on CDPM applications, the reader is referred to [132].

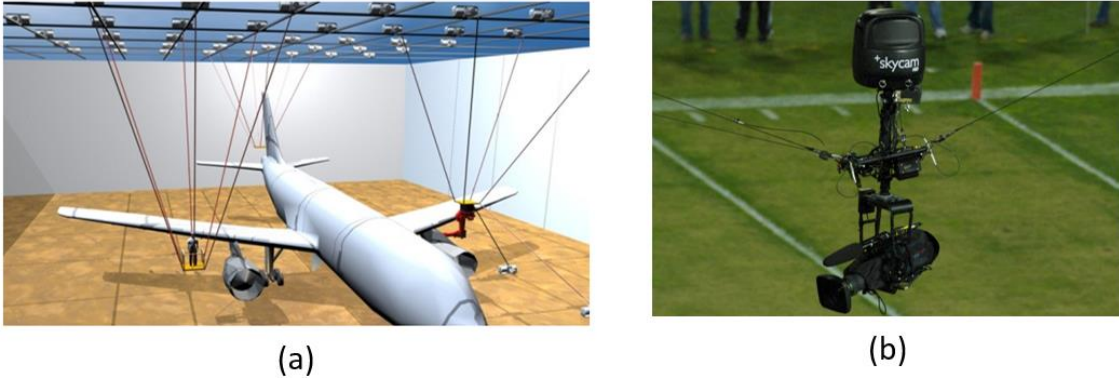


Figure 52: Applications for CDPMs: (a) Maintenance: CABLEBOT [133], and (b) Video recording: Skycam [134].

In the general case, an n -DOF CDPM controlled by m cables is said to be: incompletely restrained (or under restrained) if $m < n+1$, completely restrained if $m = n+1$ and redundantly restrained if $m > n+1$ [105].

While a CDPM has several advantageous properties, its applications are limited by the unilateral driving nature of a cable. Therefore, the study of the CDPM workspace is limited by generating only configurations with non-negative cable tensions.

Based on equilibrium analysis, several types of approaches have been developed. Ebert-uphoff [135] introduced the definition of the force closed workspace (FCW) and the wrench-feasible workspace (WFW). The main difference between FCW and WFW is the unlimited cable tensions for the FCW. Riechel and Ebert-Uphoff [136] determined the force feasible workspace of the particular case of point mass CDPMs. Krut [137] computed the largest isotropic force as a performance index of the workspace of a wire robot. Bosscher [138], Stump [139] described an analytical method for workspace calculation while Bouchard [140] used a geometric method. Diao [141] studied the force closure workspace of 6 DOF manipulators through a Jacobian matrix examination. Pham [142] calculated FCW and WFW through a dimension reduction of the equilibrium system of equations. He also evaluated the quality of the workspace via a tension factor and a global tension index. Lim [143] developed a force closure analysis through a convex analysis for fully and under constrained CDPMs. Gouttefarde [144] implemented a non-discrete method based on interval analysis to determine the WFW.

All these cited works do not address several design considerations, but they mainly focused on the method to determine the workspace of a CDPM for a given mechanical structure.

However, investigating the mechanical structure of a CDPM in order to optimize its workspace could lead to more effective solutions.

In the special case of suspended platforms, several authors [145][146][147] compared different robot's geometries via a global condition index. Hiller et al. [148] analyzed a Tendon-Based Stewart Platform based on several aspects, i.e., controllable workspace, forward kinematics, and trajectory planning. Alikhani et al. [149] investigated a geometrical synthesis of a large scale translational CDPM in addition to cables and actuators seizing. Du [150] studied large workspace CDPM structural parameters while taking into account the cable curvature effect. Leclerc [151] optimized the geometry of a flight simulator based on a multi objective algorithm that maximizes the total orientation of the end-effector and minimizes the risk of cable interferences. Using interval analysis, Bruckmann [152] introduced the outlines for a multiple criteria optimization for CDPMs. These criteria are: equilibrium, stiffness, specific workspace, robot task, and number of cables. Ouyang [153] locally maximized the total orientation of the WFW based on a grouped coordinate descent method.

Most of the cited works do not consider explicitly the design of a CDPM for a prescribed workspace. However, this problem was widely investigated for classical parallel mechanisms [154][155].

The design of CDPMs has to take into account two constraints, i.e., non-negative tensions in all the cables and no cable interference.

4.1.1. Tension condition and wrench feasibility

In the case of an n -DOF CDPM with m cables, an external wrench, f , applied to the mobile platform, is balanced by the non-negative tensions in the cables. The i^{th} cable is attached to the base in point A_i and attached to the mobile platform in B_i . The pose of the end-effector, q , and the external wrench, f , are written at the mobile platform's center P (see Figure 53).

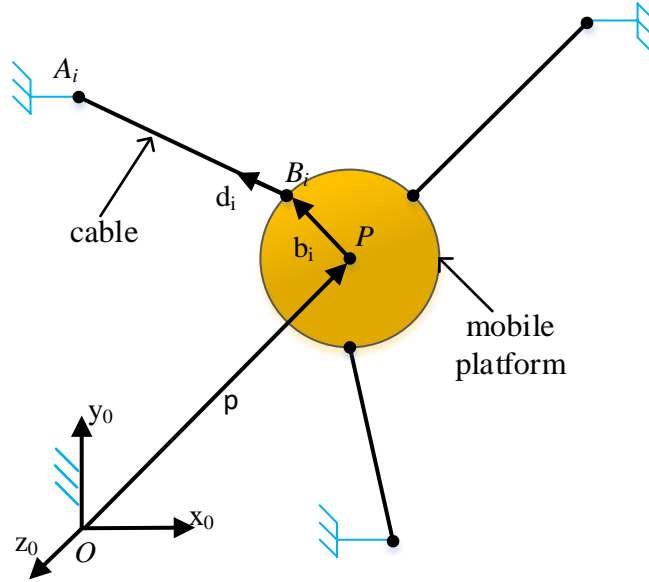


Figure 53: Kinematic diagram of a CDPM.

The equilibrium of the end-effector can be expressed by the following set of linear equations:

$$W t = f$$

where

$$W = \begin{pmatrix} d_1 & \cdots & d_m \\ b_1 \times d_1 & \cdots & b_m \times d_m \end{pmatrix} \quad (16)$$

and

$$d_i = B_i A_i / \|B_i A_i\|, \quad b_i = P B_i$$

$t = (t_1, \dots, t_m)^T$ is the column vector of cable tensions and f is the column vector that represents the external loads (forces and moments).

The W matrix is called force-moment transformation matrix [129], and it maps the loads from the cables space to the Cartesian space (loads acting on the robot's effector). Also, this matrix is known as 'structure matrix' [142].

A pose q of a manipulator's effector is said to be wrench-feasible if the CDPM balances any external wrench f in $[f]$ with a bounded non-negative tension t in $[t]$. Here $[f]$ and $[t]$ are, respectively, the prescribed ranges of wrenches and tensions.

To check if the system $Wt=f$ is wrench-feasible or has a bounded non-negative solution, two methods may be employed. The first is by minimizing an objective function as follows [144]:

$$\min(\sum_i^m t_i) \text{ subject to } Wt=f \text{ and } t \in [t] \quad (17)$$

The optimization problem (17) minimizes the sum of cable tensions while ensuring that the equilibrium $Wt=f$ is achieved and the tensions in the cables, t , are within admissible values $[t]$. Note that the objective function may be modified, e.g. by adding a weight coefficient for each cable. The second method is to employ Moore-Penrose pseudo inverse of redundant manipulators [156]:

$$t=W^+ f+(I_m - W^+ W)z \text{ such that } W^+ = W^T (W W^T)^{-1} \quad (18)$$

where $W^+ f$ is the particular solution, $(I_m - W^+ W)z$ is the homogenous solution and z is an arbitrary m dimensional vector. Here, we are looking for a vector z such that t remains within $[t]$ by summing the homogenous and the particular solution. Later, the first method will be utilized to verify the wrench-feasibility of the equilibrium.

4.1.2. Cable interference

Generally speaking, cable interferences are of 3 types: cable to cable, cable to end-effector and cable to workpiece [156][157][158]. Collision detection is usually achieved through computing geometrical relationships.

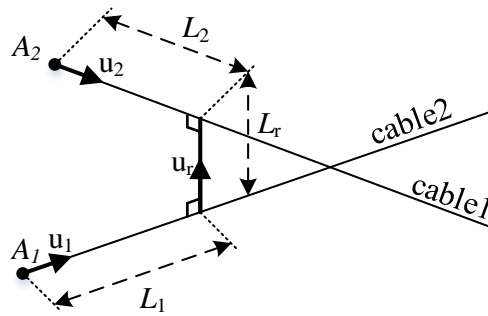


Figure 54: Cable/cable collision detection.

A cable/cable collision happens when two cables meet each other. In this case, mathematically the minimal distance between them is zero. To illustrate, let's consider the example in Figure 54. L_r is the shortest distance between cable1 and cable2, its unit vector u_r is perpendicular to the two cables. A_1 and A_2 are cable exit points, u_1 and u_2 are unit vectors carrying distances L_1 and L_2 , respectively.

$$A_1 + L_1 u_1 + L_r u_r - L_2 u_2 = A_2 \quad (19)$$

The geometrical relationship presented in Eq (19) consists of 3 equations with 3 unknowns, thus solving Eq (19) yields the unknown L_r [151][158]. One shall note that for planar CDPMs cable to cable collision is ignored since cables can be placed in parallel planes in order to avoid interference [156].

Interference between a cable and the end-effector can be detected through angular measurement. Assuming that the end-effector is a convex polygon and that the cables are placed on its vertices, according to Figure 55 if the angle α_i , taken between d_i and v_i , lies within a specific range, a cable/end-effector collision is avoided [156].

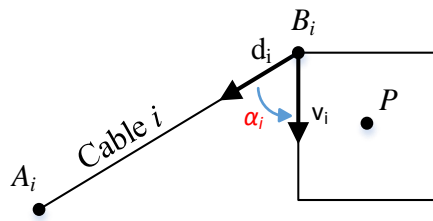


Figure 55: Cable/end-effector collision detection.

The last form of interference, i.e., cable/workpiece, involves the existence of an object in the workspace of the robot (Figure 56). Solving this type of interference depends on the shape of the object. As an example, the box-based algorithm is used in [159].

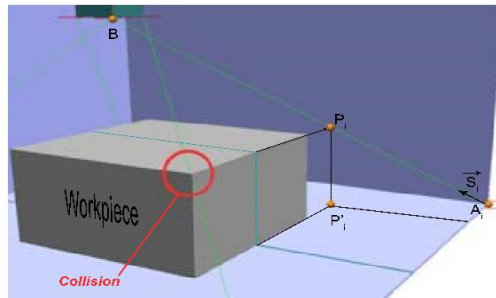


Figure 56: Cable/workpiece interference.

4.2. Introduction to Interval Analysis

4.2.1. Overview

Data analysis and computing of real numbers are usually sensitive to uncertainties, e.g. measurement errors are often encountered when recording signals. Further, a major problem in computing is rounding errors. In fact an infinite number of reals cannot be written in the binary form, and therefore an approximation step is substantial. In robotics, a main source of uncertainties is manufacturing tolerances, so that a difference between the real robot and the developed model is always persistent [160]. The idea behind interval analysis is to provide mathematical tools to deal with inaccuracy and imprecision issues that may induce erroneous results. A well-known example to show the drawback of real number approximation is the

Rump's Example [161][162]. It consists in computing the function f with arguments $(x_0, y_0) = (77617, 33096)$:

$$f(x, y) = (333.75 - x^2)y^6 + x^2(11x^2y^2 - 121y^4 - 2) + 5.5y^8 + x/2y \quad (20)$$

Using standard round-to-nearest IEEE-754 methods, evaluation of f under (x_0, y_0) yields:

$$\begin{aligned} 32\text{-bit} : f(x_0, y_0) &= 1.172604 \\ 64\text{-bit} : f(x_0, y_0) &= 1.1726039400531786 \\ 128\text{-bit} : f(x_0, y_0) &= 1.1726039400531786318588349045201838 \end{aligned} \quad (21)$$

All results in (21) are similar but they are, all, wrong. In fact f can be reduced to Eq (22) [161]:

$$f(x_0, y_0) = (x_0 / 2y_0) - 2 \text{ since } x_0^2 = 5.5y_0^2 + 1 \quad (22)$$

Thereby, the correct result is: $f(x_0, y_0) = -0.827396059946821368141165095479816$.

The purpose of interval analysis is to enclose inexact information within an interval having upper and lower bounds in the way that all errors can be included. Consequently, interval algorithms will produce a bounded solution. E.g. evaluation of f in Eq (20) using intervals for x_0 and y_0 yields an interval containing the correct solution [163]. In general, the use of intervals allows coping with different types of errors in order to provide reliable results.

In the context of CDPMs, the workspace analysis is usually performed using a discretization based method. However, this method cannot cover all the desired workspace since it would require an infinite number of poses. Working with intervals instead of discrete poses can overcome this limitation. Whereas the discrete method overlooks the poses not included in the analysis, the interval approach considers all the given range of poses, thus it guarantees a singularity free workspace. In addition, the interval analysis can handle errors and uncertainties in the determination of the parameters of the cable robot. These errors are mainly due to the uncertainty on the locations of the cable attachment points and manufacturing errors. The downside of the interval analysis method, however, is its high computational time [163].

4.2.2. Interval mathematic

An interval $[x]$ is defined as a set of real numbers x bounded by two real endpoints \underline{x} and \bar{x} :

$$[x] = [\underline{x}, \bar{x}] = \{x \in \mathbb{R} \mid \underline{x} \leq x \leq \bar{x}\} \quad (23)$$

where \underline{x} is the lower bound and \bar{x} is the upper bound. The midpoint or the center of an interval is $\text{mid}([x]) = (\underline{x} + \bar{x}) / 2$, the radius is $\text{rad}([x]) = (\bar{x} - \underline{x}) / 2$ and the width is two times the radius. If $\underline{x} = \bar{x}$ then the interval has a zero width or radius and is called degenerative. A basic operation on an interval is bisection, let consider *bisect* the operator of bisection then:

$$\text{bisect}([x]) = \{[\underline{x}, m], [m, \bar{x}]\}, m = \underline{x} + \bar{x} / 2 \quad (24)$$

Note that in interval mathematic, real arithmetic and linear algebra are extended such that real numbers are replaced by intervals. In the sequel, interval arithmetic and interval linear systems will be explained.

Arithmetic operations on real numbers such addition or multiplication have their equivalent with reference to intervals, let $\circ = \{+, -, \times, \div\}$ be the set of arithmetic operations, then for the interval numbers $[x]$ and $[y]$:

$$[x] \circ [y] = \{x \circ y | x \in [x], y \in [y]\} \quad (25)$$

So, the result of the operation $[x] \circ [y]$ will be the set of operations $x \circ y$ for any x in $[x]$ and for any y in $[y]$. For example:

$$\begin{aligned} [-1, 3] + [2, 4] &= [-1 + 2, 3 + 4] = [1, 7] \\ [-1, 3] \times [2, 4] &= [-1 \times 4, 3 \times 4] = [-4, 12] \end{aligned} \quad (26)$$

In the first equation of (26), the interval $[1, 7]$ encloses the result of all operations $x+y$ for all $x \in [-1, 3]$ and for all $y \in [2, 4]$.

In addition to arithmetic operations, elementary functions such as \ln , \exp , \cos , \sin , \tan , sqrt and so on are extended to receive intervals as arguments, e.g.:

$$\ln([1, 3]) = [0, 1.0987] \quad (27)$$

In Eq (27) the result $[0, 1.0987]$ encloses all possible value of $\ln(x)$ such that $x \in [1, 3]$. Thereby, considering a real function f , by replacing variables, operators and elementary functions by their interval counterparts, the function f can be interval evaluated, e.g. :

$$\begin{aligned} \text{for } f(x, y) = e^x + y \text{ under } [x] = [1, 4] \text{ and } [y] = [-1, 3] \text{ then} \\ [f]([x], [y]) = e^{[1, 4]} + [-1, 3] = [2.7, 54.5] + [-1, 3] = [1.7, 57.5] \end{aligned} \quad (28)$$

Let f be a real function of real variables $x = x_1, \dots, x_n$, and $[f]$ an interval function of one or more interval arguments $[x] = ([x_1] \dots [x_n])$ that encloses the exact image $f([x])$ of $[x]$ under f [163]:

$$\begin{aligned} f([x]) &= f([x_1] \dots [x_n]) \\ &= \{f(x) | x_i \in [x_i], i = 1..n\} \subseteq [f]([x]) \end{aligned} \quad (29)$$

The most known interval evaluation $[f]$ of functions is natural evaluation [164], which is described in Eq (28). Using natural evaluation, $[f]([x])$ overestimates $f([x])$ due to

dependence and wrapping effects [164], and in the case of equality between them, $[f]$ is called minimal. The dependence effect involves multiple occurrences of the same variable in the expression of f and the wrapping effect is induced by discontinuities of f . Thus, the accuracy of the evaluation depends to the expression of f . To explain this issue, we consider a function written in different expressions [164]:

$$\begin{aligned}
 f_1 &= x(x+1) \\
 f_2 &= x \times x + x \\
 f_3 &= x^2 + x \\
 f_4 &= (x + (1/2))^2 - (1/4)
 \end{aligned} \tag{30}$$

Natural evaluation of equations (30) for the interval $[x] = [-1, 1]$ yields:

$$\begin{aligned}
 [f_1]([x]) &= [-2, 2] \\
 [f_2]([x]) &= [-2, 2] \\
 [f_3]([x]) &= [-1, 2] \\
 [f_4]([x]) &= [-(1/4), 2]
 \end{aligned} \tag{31}$$

Therefore, one can confirm that the accuracy of the evaluation depends on the formal expression of f . The function f_4 is minimal since the variable x occurs only once and f_4 is continuous [164].

Other than natural evaluation, many methods such as centered, mixed centered and Taylor inclusion functions have been defined in order to obtain a sharper interval $[f]$. Alternatively, an optimization-based evaluation may be employed to get the enclosure of a function's image [163]. Such method will be addressed in the next section in order to write the transformation matrix.

It is worth noting that regardless the expression of a function f , the width of its image is sharper as the width of the arguments decreases. Indeed, if we bisect an argument $[x]$ into smaller boxes $[x_i]$ then the union of images $[f]([x_i])$ is sharper than $[f]([x])$. Therefore, the following inclusion can be made [163] :

$$[x] = \bigcup_{i=1}^m [x_i] \quad \text{then} \quad [f]([x]) \subseteq \bigcup_{i=1}^m [f]([x_i]) \tag{32}$$

Evaluating $f_3 = x^2 + x$ in (30) with argument $[x] = [-1, 1]$ bisected into 4 equal intervals:

$$\begin{aligned}
 [x] &= [-1,1] = [-1, -0.5] \cup [-0.5,0] \cup [0,0.5] \cup [0.5,1] \\
 [f_3]([-1, -0.5]) &= [-0.7501, 0.5] \\
 [f_3]([-0.5,0]) &= [-0.5, 0.2501] \\
 [f_3]([0,0.5]) &= [0, 0.7501] \\
 [f_3]([0.5,1]) &= [0.7499, 2] \\
 [f]([x]) &= [-1, 2] \subseteq \bigcup_{i=1}^4 [f]([x_i]) = [-0.7501, 2]
 \end{aligned} \tag{33}$$

It is clear that in Eq (33) the bisection technique is useful to lessen the effect of overestimation. However, bisecting intervals in small sizes will induce extra computational time that can be prohibitive if m is large and especially when bisecting in high dimensions. Thus, the choice of the bisection size and the number of variables to be subdivided is crucial in order to keep a reasonable computational time [163].

Now moving to describe linear systems in their interval form, an n dimensional interval vector, called also a box is a vector whose components are intervals can be written as follows:

$$[x] = ([x_1] \ \dots \ [x_n]) = ([\underline{x}_i, \bar{x}_i] \ \dots \ [\underline{x}_n, \bar{x}_n]) \text{ such that } \underline{x}_i \leq x_i \leq \bar{x}_i \ i = 1, \dots, n \tag{34}$$

Similarly, an n by m dimensional interval matrix is a matrix whose elements are intervals can be written as follows:

$$[A] = \begin{pmatrix} [A_{1,1}] & \dots & [A_{1,m}] \\ \vdots & \ddots & \vdots \\ [A_{n,1}] & \dots & [A_{n,m}] \end{pmatrix} \text{ such that } \underline{A}_{i,j} \leq A_{i,j} \leq \bar{A}_{i,j} \ i = 1, \dots, n \ \& \ j = 1, \dots, m \tag{35}$$

For a real linear system $Ax = b$, an interval linear system is defined as follows:

$$[A]x = [b] \tag{36}$$

where $[A]$ is an interval matrix, $[b]$ is an interval vectors. The solution $[x]$ of Eq (36) is the set of vectors x such that for all $A \in [A]$ and for all $b \in [b]$, the system $Ax = b$ holds [163]:

$$[x] = \{x \mid Ax = b, \forall A \in [A] \text{ and } \forall b \in [b]\} \tag{37}$$

The shape of the solution $[x]$ is complex. Thus, from a practical point of view, we are only asked to find the narrowest interval vector that encloses the solution, called the hull of the solution [163]. For demonstration, let's consider the following system [163]:

$$\begin{bmatrix} [2, 3] & [0, 1] \\ [1, 2] & [2, 3] \end{bmatrix} \begin{bmatrix} x_1 \\ x_2 \end{bmatrix} = \begin{bmatrix} [0, 120] \\ [60, 240] \end{bmatrix} \tag{38}$$

The exact solution of Eq (38) is presented in Figure 57:

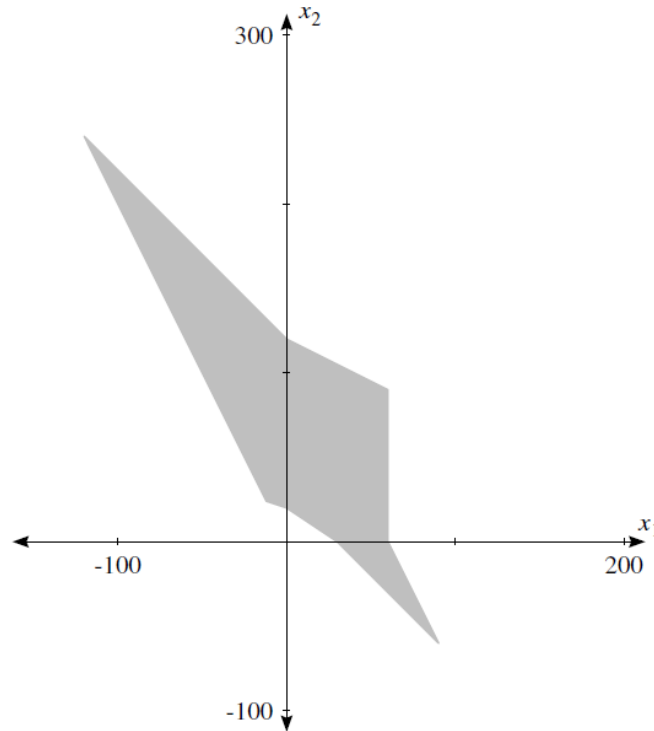


Figure 57: Complex shape of the exact solution of the interval linear system [163].

In the meanwhile, the hull of the solution can be obtained through various methods: Gaussian elimination, Hull method, Gauss-Seidel method and Krawczyk method [163][165]. For the system in Eq (38), the smallest box, i.e., the hull solution is: $[x] = [-120, 90] \quad [-60, 240]$. This box encloses the complex shape given in Figure 57.

Here, an important issue is to verify the solvability or the feasibility of systems of interval linear equations. In fact, based on [166] and assuming that $[A]$ is $n \times m$ interval matrix and $[b]$ is an n dimensional interval vector, then $[A]x = [b]$ is called strongly solvable if it has a solution $[x]$ and is called strongly feasible if it has a non-negative solution $[x]$. A feasibility test will be investigated in the next section in order to verify the tension condition for a CDPM. Further information and details on interval analysis can be found in [163][164] [165].

4.3. Interval-Analysis-Based Design of CDPMs

In this section, employing interval analysis tools, the equilibrium of a CDPM is written and solved in its interval form. First, the transformation matrix is evaluated using interval arithmetic and an optimization procedure. Then, wrench-feasibility of the equilibrium is verified by examining its interval linear system. Finally, the proposed design algorithm capable of finding all feasible sets of design parameters that guarantee the access to a desired workspace, is described.

4.3.1. Interval form of the equilibrium

Writing the classical linear system that describes the equilibrium $Wt=f$ in its interval form requires the use of interval arithmetic in order to compute the transformation interval matrix. In fact, the equilibrium $Wt=f$ can be extended using interval analysis as follows:

$$[W]t=[f] \quad (39)$$

where t is an m dimensional vector of unknowns that describes the required tensions to satisfy the equilibrium.

$[f]$ is an n dimensional interval vector that contains the bounds of the forces and moments, that are applied on the robot end-effector.

$[W]$ is an n by m interval matrix obtained from interval evaluation of the transformation matrix such that:

$$W_{i,j} = f(A_i, B_i, q) \Rightarrow [W_{i,j}] = [f]([a_i], [b_i], [q]) \quad (40)$$

Where $[a_i]$ is the location box of the exit point A_i , $[b_i]$ is the location box of the connection point B_i , and $[q]$ is a box containing a specific range for robot poses $q=(p^T, r^T)^T$. p describes the position of the mobile platform and r defines its orientation.

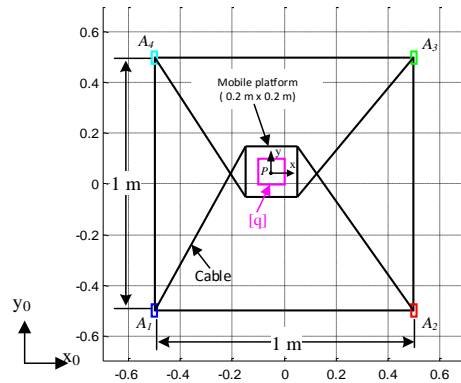


Figure 58: A 3-DOF planar robot and its desired workspace $[q]$.

The basic method to compute the interval matrix, $[W]$, is to apply natural evaluation of the elements of W [144]. For illustration, the example of a 3-DOF planar robot, shown in Figure 58, is considered.

The robot is controlled by 4 cables, the A_i points are located in boxes $[a_i]$ of $20 \text{ mm} \times 50 \text{ mm}$, the B_i points and P point are located, respectively, at the vertices and at the center of

the mobile platform's rectangle. For a range of poses $[q] = ([-0.1, 0] \quad [0, 0.1] \quad [-10^\circ, 10^\circ])^T$, the output of natural evaluation of $[W]$ is:

$$\begin{pmatrix} [-1.439, -0.353] [0.451, 1.406] [0.414, 1.219] [-1.172, -0.318] \\ [0.331, 1.485] [0.299, 1.198] [-1.251, -0.396] [-1.456, -0.430] \\ [-0.210, 0.204] [-0.200, 0.163] [-0.175, 0.168] [-0.160, 0.207] \end{pmatrix} \quad (41)$$

The Expression of W for the planar robot is given in Appendix 3. $[W_{ij}]$ are obtained by evaluating $W_{ij}(A, B_i, q)$ under $[a_i]$, $[b_i]$ and $[q]$. In the case of $[W_{1,1}]$, we have:

$$\begin{aligned} W_{1,1} = d_1 &= \frac{A_1 B_1}{\|A_1 B_1\|} = \frac{(A_{1x} - P_x - B_{1x} \cos(\phi) + B_{1y} \sin(\phi))}{((A_{1x} - P_x - B_{1x} \cos(\phi) + B_{1y} \sin(\phi))^2 + (P_y - A_{1y} + B_{1y} \cos(\phi) + B_{1x} \sin(\phi))^2)^{(1/2)}} \\ &= f(A_1, B_1, q) \end{aligned} \quad (42)$$

Then, under the following arguments: $[a_1] = ([-0.5101, -0.4899] \quad [0.4749, 0.5251])^T$, $[b_1] = (-0.1 \quad 0.1)^T$ and $[q] = ([-0.1, 0] \quad [0, 0.1] \quad [-10^\circ, 10^\circ])^T$, we have:

$$[W_{1,1}] = [f]([a_1], [b_1], [q]) = [-1.439, -0.353] \quad (43)$$

As mentioned in Section 4.2.2, the main drawback of the natural inclusion function is the overestimation of the exact image of $f([a_i], [b_i], [q])$ because of the dependence and wrapping effects [164]. To overcome this limitation, interior-point nonlinear optimization algorithm [167] is used. W_{ij} 's are processed through the optimization procedure to get the lower and the upper bounds, the yielded $[W]$ matrix for the same example of Figure 58 is:

$$\begin{pmatrix} [-0.893, -0.461] [0.586, 0.923] [0.515, 0.861] [-0.814, -0.396] \\ [0.450, 0.888] [0.384, 0.810] [-0.857, -0.508] [-0.919, -0.582] \\ [-0.104, 0.106] [-0.112, 0.089] [-0.098, 0.099] [-0.090, 0.111] \end{pmatrix} \quad (44)$$

Comparing the two methods, i.e., natural and optimization-based evaluations the width of $[W_{1,1}]$ in Eq (44) is about 0.43, which is less than half of the one in (41) given by 1.086. All $[W]$ elements $[W_{ij}]$, are sharper using optimization-based evaluation Eq (44) than using natural inclusion function Eq (41). Therefore, the optimization technique is more efficient in estimating $[W]$, and hence requires less computational time to find the solution for the design of a CDPM.

Here, we shall notice that even using the optimization method, the overestimation of $[W]$ persists. In fact, W_{ij} are nonlinear functions and the exact image of $[W]$ is a complex shape (see Section 4.2.2.), thus there exist many matrices $W \in [W]$ such that $W \neq W_{ij}(A, B, q)$, i.e., W

is not a transformation matrix. This negative aspect is induced by the loss of dependency between the W_{ij} at the time of determination of $[W]$ [144][163].

As mentioned previously, the basic method to lessen the overestimation problem is the bisection technique. In fact, when $[W]$ intervals are large, the feasibility check (see Section 4.3.2.) of the equilibrium may not succeed and a bisection technique of the input variables ($[a_i]$, $[b_i]$ and $[q]$) is essential in order to narrow down the width of $[W]$ intervals [144].

4.3.2. Wrench Feasibility of the equilibrium

In this section, we shall discuss the feasibility of an interval linear system of equations that will ensure the feasibility of the equilibrium. It will be shown that for a given workspace $[q]$, the equilibrium is verified by checking only the feasibility of a finite number of linear systems.

The equilibrium system $[W]t = [f]$ given in Eq (39) is said to be wrench-feasible when:

$$\forall W \in [W] \text{ and } \forall f \in [f] \text{ then } \exists t \in [t] \text{ such that } Wt = f \quad (45)$$

Therefore, for any matrix W that belongs to $[W]$ and for any external wrench f in $[f]$, the equilibrium is attained such that the solution t lies within $[t]$. $[t] = ([t_1], \dots, [t_m])^T = ([\underline{t}_1, \bar{t}_1], \dots, [\underline{t}_m, \bar{t}_m])^T$ defines the minimum and the maximum tension in each cable.

Furthermore, since W_{ij} are functions of A_i , B_i and q (40), then we have:

$$\forall a_i \in [a_i], \forall b_i \in [b_i] \text{ and } \forall q \in [q], W_{ij}(A_i, B_i, q) \in [W_{ij}] \quad (46)$$

Then, using equations (46) and (45), the system $[W]t = [f]$ is wrench-feasible when:

$$\forall a_i \in [a_i], \forall b_i \in [b_i], \forall q \in [q] \text{ and } \forall f \in [f] \text{ then } \exists t \in [t] \text{ such that } Wt = f \quad (47)$$

In other words, the equilibrium $[W]t = [f]$ is wrench-feasible if: for each point A_i and the placement point B_i and for any pose q that belongs to the desired space $[q]$, then a bounded non-negative solution t can be found such that the equilibrium constraint is satisfied.

Relying on the work of Rohn [166], to check the feasibility of an interval linear system of equations, we have the following theorem:

Theorem 1:

A set of equations $[A]x = [b]$ is strongly feasible if and only if, for each $y \in Y_n$ the system $A_y x = b_y$ has a nonnegative solution x_y . Moreover, if this is the case, then for each $A \in [A]$ and

$\mathbf{b} \in [\mathbf{b}]$, the system of equations $[\mathbf{A}]\mathbf{x} = [\mathbf{b}]$ has a solution in the set $\{\mathbf{x}_y \mid y \in \mathbf{Y}_n\}$.

\mathbf{Y}_n is the set of n dimensional column vector \mathbf{y} whose components y_k are equal to 1 or to -1, and the cardinal of \mathbf{Y}_n is equal to 2^n . By means of \mathbf{Y}_n , the interval system $[\mathbf{A}]\mathbf{x} = [\mathbf{b}]$ is decomposed into 2^n classical systems $\mathbf{A}_y \mathbf{x} = \mathbf{b}_y$ associated with \mathbf{y} vectors, each one has \mathbf{x}_y as a solution.

Using the system $\mathbf{A}_y \mathbf{x} = \mathbf{b}_y$, the k^{th} row is of the form:

$$\begin{aligned} \text{if } y_k = 1 & \quad \text{then } (\underline{\mathbf{A}} \mathbf{x})_k = \bar{b}_k \\ \text{if } y_k = -1 & \quad \text{then } (\bar{\mathbf{A}} \mathbf{x})_k = \underline{b}_k \end{aligned} \quad (48)$$

Here, each system $\mathbf{A}_y \mathbf{x} = \mathbf{b}_y$ is built depending on the values of \mathbf{y} 's components. Indeed, for a row k , based on the value y_k (either 1 or -1), we select either the upper bound or the lower bound of an element of $A_{kj} = [\underline{A}_{kj}, \bar{A}_{kj}]$ and a component of $\mathbf{b}_k = [\underline{b}_k, \bar{b}_k]$.

The following example will be used to illustrate the use of Theorem 1. A 2-DOF/3-cables robot is considered. The set \mathbf{Y}_2 is composed of 2 dimensional \mathbf{y} vectors, it has a cardinal of $2^2=4$ and the components of the \mathbf{y} vectors are either equal to 1 or equal to -1. Thereby, the set \mathbf{Y}_2 will be:

$$\mathbf{Y}_2 = \left\{ \begin{pmatrix} 1 \\ 1 \end{pmatrix}, \begin{pmatrix} 1 \\ -1 \end{pmatrix}, \begin{pmatrix} -1 \\ 1 \end{pmatrix}, \begin{pmatrix} -1 \\ -1 \end{pmatrix} \right\} \quad (49)$$

Assuming that for a robot pose $[\mathbf{q}]$, the equilibrium is written as follows:

$$\begin{bmatrix} [-18.62, -0.001] & [0.52, 1.9] & [0.48, 1.92] \\ [-5.39, 1.9] & [-0.26, -0.025] & [0.14, 0.5] \end{bmatrix} [\mathbf{t}] = \begin{bmatrix} [-10, 10] \\ [-10, 10] \end{bmatrix} \quad (50)$$

Then for each $\mathbf{y} \in \mathbf{Y}_2$, the associated 2^2 systems of linear equations $\mathbf{W}_y \mathbf{t} = \mathbf{f}_y$ are:

$$\begin{aligned} \text{for } \mathbf{y} = \begin{pmatrix} 1 \\ 1 \end{pmatrix} & : \begin{bmatrix} -0.001 & 1.9 & 1.92 \\ 1.9 & -0.025 & 0.5 \end{bmatrix} \mathbf{t} = \begin{bmatrix} -10 \\ -10 \end{bmatrix} \\ \text{for } \mathbf{y} = \begin{pmatrix} 1 \\ -1 \end{pmatrix} & : \begin{bmatrix} -0.001 & 1.9 & 1.92 \\ -5.39 & -0.26 & 0.14 \end{bmatrix} \mathbf{t} = \begin{bmatrix} -10 \\ 10 \end{bmatrix} \\ \text{for } \mathbf{y} = \begin{pmatrix} -1 \\ 1 \end{pmatrix} & : \begin{bmatrix} -18.62 & 0.52 & 0.48 \\ 1.9 & -0.025 & 0.5 \end{bmatrix} \mathbf{t} = \begin{bmatrix} 10 \\ -10 \end{bmatrix} \\ \text{for } \mathbf{y} = \begin{pmatrix} -1 \\ -1 \end{pmatrix} & : \begin{bmatrix} -18.62 & 0.52 & 0.48 \\ -5.39 & -0.26 & 0.14 \end{bmatrix} \mathbf{t} = \begin{bmatrix} 10 \\ 10 \end{bmatrix} \end{aligned} \quad (51)$$

Linear equations (51) are constructed as follows: for a row k , if $y_k = -1$ then W_{kj} is equal to \bar{W}_{kj} and f_k is equal to \underline{f}_k . Conversely, if $y_k = 1$ then W_{kj} is equal to \underline{W}_{kj} and f_k is equal to \bar{f}_k .

According to Theorem 1, the interval linear set of equations (50) is wrench-feasible, if and only if, all the 4-derived (, i.e., for all $y \in Y_2$) classical linear set of equations $W_y t = f_y$ are feasible.

A single system $W_y t = f_y$ is feasible or has a nonnegative solution when the optimization procedure:

$$\min\left(\sum_i^m t_i\right) \text{ subject to } W t = f \text{ and } t \in [t] \quad (52)$$

has a nonnegative solution for the t vector. Weights of the objective functions are all equal to one. In our case, all the cables are assumed to have the same pulling capability.

Eventually, the system $[W]t = [f]$ is wrench-feasible if all the single systems $W_y t = f_y$ are wrench-feasible, i.e., have a non-negative bounded solution $t \in [t]$.

4.3.3. Design algorithm of CDPMs

Our design algorithm is based on a discretization of a set of parameters. First, a set of variables that describes the geometry of the CDPM, called design parameters, is defined. Then, by giving the ranges and the step of discretization for each variable we generate a list of all possible geometric configurations. For each one, the equilibrium system is written in its interval form and subsequently a wrench-feasibility test is made. Thereby, we know if a configuration is feasible or not within the desired space.

The implemented algorithm is described in Figure 59. The input parameters of the algorithm are: A , B , Q , $[t]$, $[f]$, D and ε . Where A and B are lists of connection points to the fixed frame and to the end-effector, respectively. The desired workspace Q is a set of p poses: $Q = \{[q_1], [q_2], \dots, [q_p]\}$, $[t]$ is an interval vector containing the admissible cable tensions, $[f]$ is a box containing the external loads, D is a box containing length bounds of the design parameters, and ε is the discretization steps of the components of D . It is worth noticing that some boxes of A and/or B may be degenerative, when the user chooses a unique position for the connection points.

```

Feasible_boxes(A,B,Q,[t],[f],ε)
Lc = Get_Configurations(A,B,D,ε)
for i=1 to (size(Q))
    Lw = Evaluate_Transformation_Matrix(Lc,Q(i))
    Lf = Check_Feasibility(Lw,[t],[f])
    Lc = Lf
end
Lo = Get_Optimal(Lf)
return(Lo)

```

Figure 59: Computation algorithm of feasible set of boxes for a specific workspace.

A procedure called *Evaluate_Transformation_matrix()* is created to write the transformation matrix $[W]$. This procedure includes a loop that skims through the elements of the matrix W in order to get both, the upper and the lower bounds of each element. Besides, a procedure named *Check_Feasibility*($[W],[t],[f]$) is created to check whatever the system $[W]t = [f]$ is wrench-feasible.

The first operation in the algorithm is to get different configurations of the mechanical structure. For that, the procedure *Get_Configurations*(A, B, D, ϵ) produces a list L_c based on the discretization of the design parameters D using the discretization steps ϵ .

Once the list L_c of all configurations is generated, the feasibility of the equilibrium, for every desired pose from the set Q , is checked in order to find all feasible configurations. This task is performed through the for loop: a list L_w contains the evaluated $[W]$ matrices for the mechanical configurations of the list L_c , then the results of the feasibility check are stored in the list L_f . The obtained list L_f includes a set of all feasible configurations that satisfy all the required workspaces of the set Q .

One or more sets of feasible boxes may be found, a method denoted *Get_Optimal*(L_f) selects the optimal configuration according to a user defined criterion. For example, the user may choose the configuration that has the minimal lengths of the fixed mechanical frame of the CDPM.

The described algorithm is implemented in MATLAB. INTLAB interval library [168] is used for interval arithmetic and tools. *fmincon*() MATLAB Optimization function is used for the Jacobian evaluation and *linprog*() MATLAB optimization function is employed for checking the feasibility of linear systems. A desktop computer equipped with a CPU intel Core i7-3770 running at 3.4 GHz is used for the computing.

4.4. Applications to the Design of CDPMs

The illustration of the developed algorithm is carried out using 2 case-studies. The first addresses the design of a 3 DOF planar CDPM and the second one involves a spatial cable robot. As the major drawback of the interval method is the overestimation of results, the effect of bisection on the accuracy of results will be investigated.

4.4.1. Case 1: a planar CDPM

As an example, a 3-DOF planar robot is considered (Figure 60). The end-effector has a shape of a square of $0.2 \text{ m} \times 0.2 \text{ m}$ and it is controlled by 4 cables attached to its vertices.

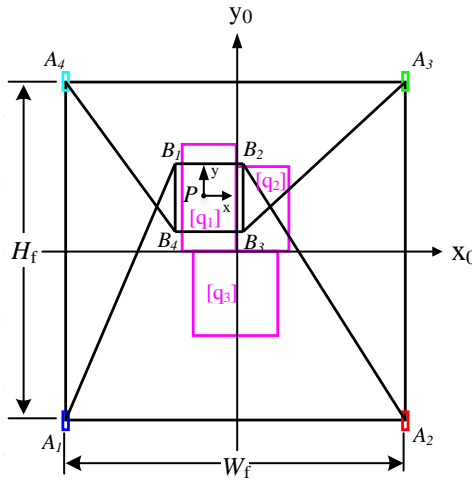


Figure 60: Example of a 3-DOF planar robot.

The robot has to reach the workspace given by $Q = \{[q_1], [q_2], [q_3]\}$ (Table 1) while resisting the external loads $[f] = ([-10, 10] \quad [-10, 10] \quad [-0.5, 0.5])^T$ (forces in N and moments in N.m), and with cable tensions varying between 1 and 50 N.

Table 5: The required workspace for planar CDPM example.

Q	$[q_1]$	$[q_2]$	$[q_3]$
Pose box	$\begin{pmatrix} [-0.1563, 0] \\ [0, 0.3126] \\ [-30^\circ, 30^\circ] \end{pmatrix}$	$\begin{pmatrix} [0, 0.1563] \\ [0, 0.2501] \\ [-25^\circ, 25^\circ] \end{pmatrix}$	$\begin{pmatrix} [-0.1251, 0.1251] \\ [-0.25, 0] \\ [-20^\circ, 20^\circ] \end{pmatrix}$

The exit points $A_1 \dots A_4$ can be located in boxes of $20 \text{ mm} \times 50 \text{ mm}$ and the connection points $B_1 \dots B_4$, are represented by degenerative boxes.

The design parameters are the width W_f and the height H_f of the fixed frame of the CDPM (Table 2), ε is the associated discretization step. Thereby, 70 mechanical configurations were generated.

Table 6: Design parameters specifications for the planar CDPM example

	W_f [m]	H_f [m]
Lower bound	0.840	0.6
Upper bound	1.2	1.2
ε	0.040	0.100

Because of the overestimation problem, translational spaces of $[q_1]$, $[q_2]$ and $[q_3]$ are bisected, respectively, into 4×5 , 4×4 and 6×5 boxes, the total number is 66 (see Figure 62(a)). For the rotation a step of 2° is taken. All the 70 mechanical configurations are passed through the feasibility test, 6 of them are found to be feasible (see Table 7) and the computational time is 1h:34mn.

Table 7: Feasible mechanical configurations for the planar CDPM example

W_f [m]	H_f [m]	$W_f + H_f$ [m]
1.12	1.1	2.22
1.12	1.2	2.32
1.16	1.1	2.26
1.16	1.2	2.36
1.2	1.1	2.3
1.2	1.2	2.4

As a design criterion, we consider the configuration that has the minimal frame dimensions, i.e., $W_f + H_f$. Thereby, the optimal configuration has the following dimensions: $(W_f, H_f) = (1.12 \text{ m}, 1.1 \text{ m})$ corresponding to $W_f + H_f = 2.22 \text{ m}$.

4.4.2. Case 2: a Spatial CDPM

In the following example, the proposed method is applied to a spatial CDPM (Figure 61). The platform in this case has 6-DOF and it is actuated using 8 cables. The orientations of the effector is described using Z-Y-X Euler angles convention [129]. The reader is referred to Appendix 3 for more information about the formal expression of W in the spatial case.

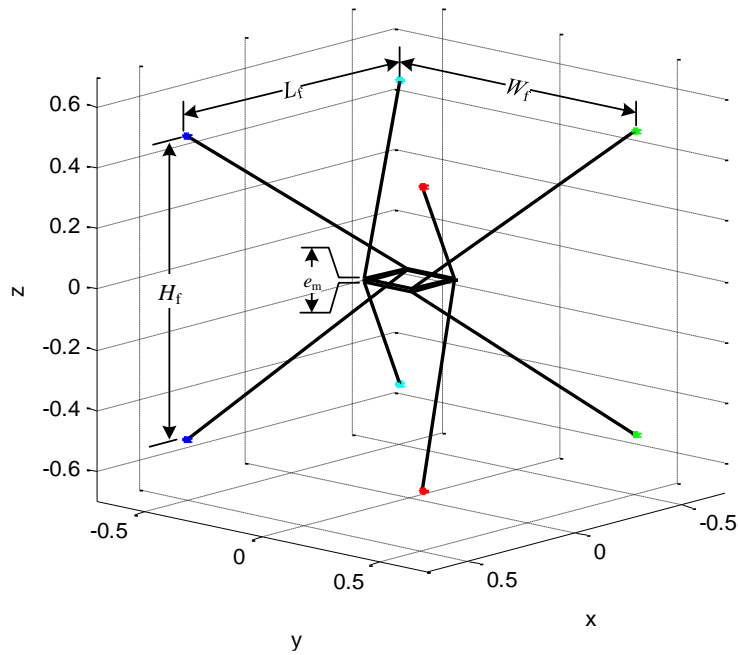


Figure 61: Example of a 6-DOF spatial robot.

The design problem is stated as follows:

Given

- A set of poses of the platform $Q = \{[q_1], [q_2], [q_3], [q_4]\}$ (Table 8),
- A set of external loads for each pose q_i given as intervals:
 $[f] = ([-10,10] \ [-10,10] \ [-10,10] \ [-0.1,0.1] \ [-0.1,0.1] \ [-0.5,0.5])^T$ (forces in N and moment in N.m),
- The upper bound and the lower bound on the tension in the different cables are 1 N and 640 N, respectively,
- A_i points locations are cubes of a side of 5 mm,
- The mobile platform is a thin parallelepiped of $200 \text{ mm} \times 0.200 \text{ mm} \times e_m$.

Find:

- The optimal locations for the fixed points to minimize the overall dimensions of both: the fixed mechanical frame and the end-effector,
- The design variables are the width of the frame W_f , the height of the frame H_f , the length of the frame L_f , and the thickness of the mobile platform e_m (Figure 6). Ranges and discretization steps are specified in Table 9.

Table 8: The required workspace for spatial CDPM example.

Q	$[q_1]$	$[q_2]$	$[q_3]$	$[q_4]$
Pose	$\begin{pmatrix} [-0.1,0] \\ [-0.1,0] \\ [-0.0751,-0.0751] \end{pmatrix}$	$\begin{pmatrix} [-0.1,0] \\ [0,0.1] \\ [-0.0751,0.0751] \end{pmatrix}$	$\begin{pmatrix} [0,0.1] \\ [-0.1,0] \\ [-0.0751,0.0751] \end{pmatrix}$	$\begin{pmatrix} [0,0.1] \\ [0,0.1] \\ [-0.0751,0.0751] \end{pmatrix}$
Interval	$\begin{pmatrix} [-10^\circ,10^\circ] \\ [0,0] \\ [-10^\circ,10^\circ] \end{pmatrix}$	$\begin{pmatrix} [-10^\circ,10^\circ] \\ [0,0] \\ [-15^\circ,15^\circ] \end{pmatrix}$	$\begin{pmatrix} [-10^\circ,10^\circ] \\ [0,0] \\ [-10^\circ,15^\circ] \end{pmatrix}$	$\begin{pmatrix} [-10^\circ,10^\circ] \\ [0,0] \\ [-15^\circ,15^\circ] \end{pmatrix}$

Table 9: Design parameters specifications for spatial CDPM example.

	W_f [m]	H_f [m]	L_f [m]	e_m [m]
Lower bound	0.8	0.8	0.8	0.01
Upper bound	1.1	1.1	1.1	0.03
ϵ	0.1	0.1	0.1	0.01

Again because of the overestimation problem, each translational space of $[q_1], [q_2], [q_3]$ and $[q_4]$ is bisected into $3 \times 4 \times 5$ boxes resulting in a total number of 240. One rotational step of 1° about the x axis is selected. From all tested configurations (192), 15 of them are found to be feasible and the optimal configuration has the following dimensions (in m): $(W_f, H_f, L_f, e_m) = (0.8, 1.1, 0.8, 0.01)$. To obtain this result the computational time is 14h:26mn.

The required computational time for the spatial case is much higher than the one required for the planar one. This high computational time is mainly due to both: the number of box poses and the number of linear equations to be checked for each box of poses. In the planar case, 8 classical linear sets of equations have to be checked for each box of poses, whereas 64 linear systems of equations are checked for the spatial case.

4.4.3. Impact of overestimation problem on the design of CDPMs

Based on the illustrated case-studies, it is observed that the accuracy of the results is sensitive to the size of $[a_i], [b_i]$ and $[q_i]$ boxes, this remark is also confirmed in [155]. Indeed, assigning the desired variables large boxes may lead to the failure of the algorithm. In reducing the size of the boxes, the results are more accurate at the expense of a longer computational time.

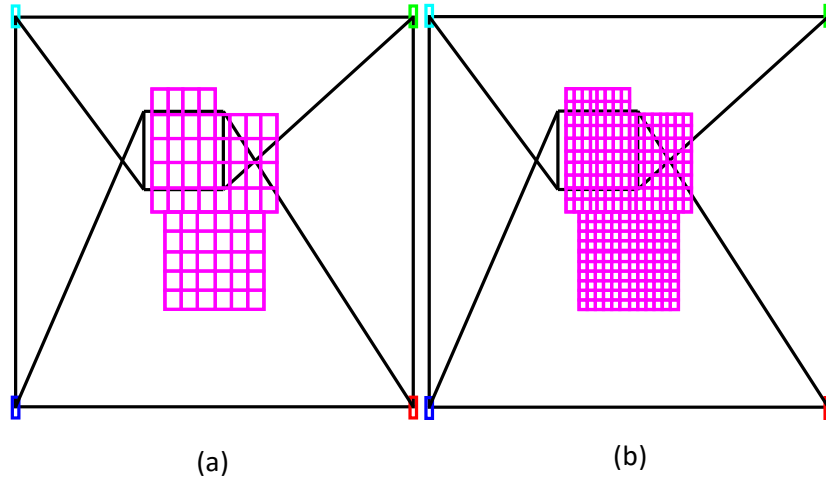


Figure 62: Bisection of the desired workspace: (a) Into 66 boxes, and (b) Into 264 boxes.

To show the effect of the size of bisection of $[q_i]$, we consider the planar example. In case 1, the translational space is bisected into 66 boxes (Figure 62(a)). Narrowing down the intervals by a factor of 2 for each translational axis, results in a number of boxes of $66 \times 4 = 264$ (Figure 62(b)). The computational time increased from 1h:34mn, in case 1, to 6h:54mn and 4 new feasible configurations are found (see Table 10). The optimal one becomes $(W_f, H_f) = (1.04 \text{ m}, 1.0 \text{ m})$ corresponding to $W_f + H_f = 2.04 \text{ m}$. Therefore, one can conclude that the interval analysis is a conservative approach, since the solution is sensitive to the size of the input boxes. However, by using the interval analysis method, one can guarantee that the desired space is fully included in the WFW, which is a singularity-free space.

Table 10 : New feasible configurations for the case of planar CDPM.

W_f [m]	H_f [m]	$W_f + H_f$ [m]
1.04	1.0	2.04
1.04	1.1	2.14
1.08	1.1	2.18
1.08	1.2	2.28

The conservatism of the interval analysis is due to the dependence and the wrapping effects, causing the overestimation of the evaluated transformation matrix W . This drawback can be viewed as an impediment to find the exact mechanical configuration that guarantees the desired WFW. Yet as noted, the accuracy of the results is sensitive to the size of the input boxes. Thus, possible feasible mechanical configurations may be viewed by the algorithm as non-

feasible and hence the obtained solution is overestimated. For that, the optimization based evaluation of W is implemented in order to reduce the negative effect of the overestimation.

When the algorithm fails due to the large size of the boxes, the obvious solution is to apply bisection technique of input boxes (, i.e., $[a_i]$, $[b_i]$ and $[q_i]$) in order to narrow the evaluated $[W]$ matrix. However, bisection in high dimension can exponentially increase the number of configurations to be checked, and hence, the computational time. An adequate strategy can be used to select the variable to be bisected, in order to reduce the computational time. Further, sampling the desired space $[q_i]$ in narrow boxes will increase dramatically the computational time beyond the capability of available computing hardware. Note that the same problem is also found for discrete methods when using a finer grid. An open challenge is to find a compromise between the size of the discretization step and a reasonable computational time.

Conclusion:

An algorithm of designing CDPMs for a specific workspace, based on interval analysis, was discussed and implemented in this chapter. The current algorithm can handle all types of CDPMs, .i.e., incompletely, completely or redundantly restrained CDPMs. for all the case, the feasibility of the equilibrium has to be confirmed, i.e., the non-negative tension constraint is satisfied.

As a powerful computing tool to handle inexactness, the interval analysis was introduced and outlined. Interval arithmetic and interval linear systems were described and used to solve the problem of wrench-feasibility.

The novelty of the developed algorithm was in using interval analysis to design CDPMs. In contrast to discrete approaches in which the workspace is viewed as a grid of points, using the interval analysis method it is seen as a whole range of poses. Hence, the given space lies entirely in the WFW and is a singularity-free workspace. Further, uncertainties on the location of the cable's attachment points can be included.

Two case-studies were considered: a planar CDPM and a spatial one. All feasible designs were found such that the cable tensions are ensured to always be within the maximum and the minimum values. Using the minimal size of the robot as a criterion, the optimal designs were computed.

Based on the given examples, it was observed that the accuracy of results is in relation to the size of pose boxes. By narrowing their sizes, through a bisection procedure, more solutions were found. Therefore, we concluded about the conservatism of the interval method.

In addition, the computational time may increase exponential if many variables are bisected into small boxes.

Interval analysis is a well-known method for obtaining reliable results at the expense of a high computational time. As a practical application, in the next chapter, the design algorithm will be applied to the CDLT in order to compute the optimal geometry of the CDLM. Whereas, for the presented examples all poses are subjected to the same external loads and cable interferences are ignored, for the design of the CDLM, using the dynamic simulation of Chapter 3, the external wrench will be evaluated over all the required space. In addition, the cable/end-effector collision will be addressed.

5. Design of the CDLT Rehabilitation Machine

Summary:

In this chapter, all the previous findings are gathered to design a prototype of the CDLT. Mainly, we focused on the design of the CDLM. Indeed, the gait kinematics obtained in Chapter 2, the dynamic simulation investigated in Chapter 3 and the algorithm of CDPMs design developed in Chapter 4, are all used to design the CDLM.

The required data to design a CDPM are the set of poses and the set of balanced wrenches. In our case, the end-effector is the orthosis that controls the pose of the leg during ambulation. Using gait kinematics (Chapter 2), we compute the workspace reached by the orthosis, which ensures also collision avoidance between the cables and the end-effector. Then, employing the inverse dynamic simulation (Chapter 3), we evaluate the wrench applied on the orthosis over the required space. The aforementioned requirements are assessed as a set of boxes using the interval analysis method developed in Chapter 4.

The aim of the design study is to compute the optimal locations of the cables' exit points, and then to simulate the required power of the actuators. Through a discretization of the design parameters, each single configuration is processed for collision detection and feasibility check. As a result, many configurations may be found to be valid. The one that minimizes the peak of the tension over all the cables is selected as the optimal configuration. Hereafter, curves of the required power are plotted. Consequently, parts of the cable drive unit, i.e., the servo motor, the gear box and the spooling drum are selected.

The second sub-system of the CDLT is the BWSD. It includes two actuated mechanisms: the electric winch and the pre-tension system. Thus, specifications of their parts are computed and suitable components are selected. This chapter ends by presenting and describing the CAD design of the gait training machine.

5.1. Design of the CDLM

As shown in Figure 63, the end-effector (orthosis) of the CDLM is controlled by 4 cables. The location of points A_i and B_i are given with respect to reference frames $\{F_0\}=\{O, x_0, y_0\}$ and $\{F_{or}\}=\{C_2, x_{lg}, y_{lg}\}$, respectively.

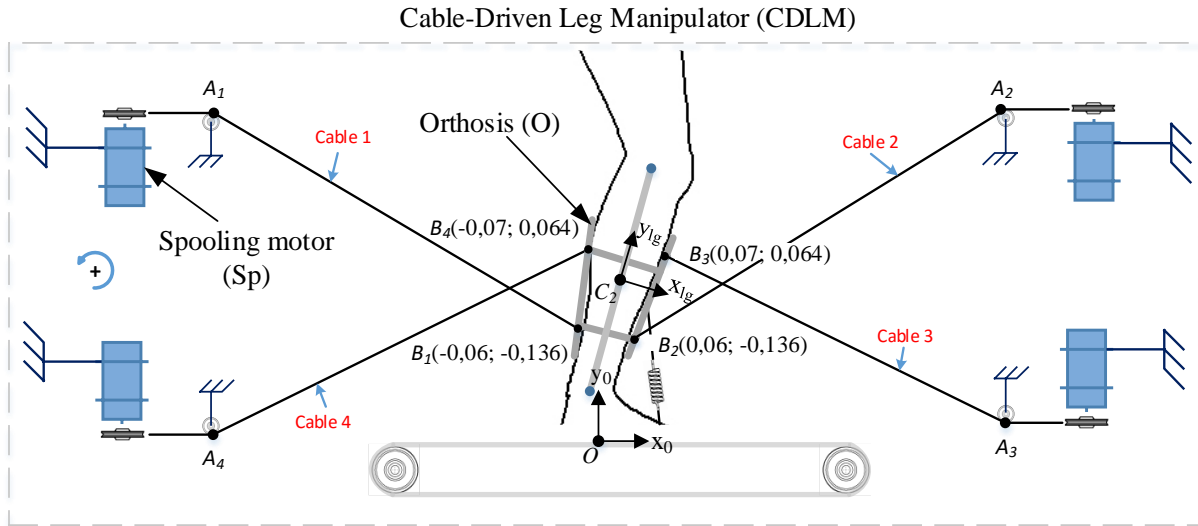


Figure 63: Geometrical specifications of the CDLM.

Assuming that: the orthosis is stationary relative to the leg and the locations of points B_i remain in fixed relative to $\{F_{or}\}$. The first task is to compute the optimal locations of points A_i and the second one is to simulate the power curves of the spooling motors (Figure 63).

5.1.1. Design requirements

Two criteria are involved for the design of the CDLM, the first one is to guarantee the feasibility of the equilibrium, i.e., it is achieved with non-negative tensions, and second one deals with the interference between the cables and the end-effector. To write the equilibrium, some information is required: the poses attained and the wrench applied by/on the end-effector. Here the external wrench is the actuation wrench computed in Chapter 3.

One of the objectives of the design analysis is to cope with the difference in heights h of the patients. These heights typically vary from 1.4 m to 1.9 m, according to [84]. Furthermore, technical specifications of the CDLM are: the GC time $t_{gc}=1.4s$ and the amount of unloading BWS can reach 20% for a body mass $m=100$ kg.

Note that the time 1.4 s corresponds to a walking speed of 3.4 km/h for a height of 1.7 m. Moreover, the smaller is the value of BWS , the more significant cable tensions are required. In our case 20% means that the robot will resist 80 kg when $m=100$ kg, which is a common value [84].

In addition, the two simulation scenarios introduced in Section 3.2.3, i.e., the on-ground and off-ground walking are considered in the design study. Including the two cases is essential, since we don't know in which case cable tensions will be more important. Moreover, for the

off-ground walking, we consider that the body elevation is 0.1 m, i.e., the sole of the foot is 0.1 m above the treadmill when the lower limb lies vertically.

5.1.1.1. Workspace and external wrench evaluation

The required workspace Q is evaluated as a set of n boxes $Q=\{[q_1],[q_2],\dots,[q_n]\}$. Further, $Q=(P^T R^T)^T$ includes translations P and rotations R . The translational workspace P is determined as follows: an initial search space $P_0 = ([-1, 1], [0, 1])^T$ is bisected into a grid of boxes $[b_0]$, each one has a width of $\varepsilon_p=0.04$ mm. Since the equilibrium is written at the leg CoM C_2 (See Figure 63), then the space P is defined by the space reached by C_2 . The height of body h is varied from 1.4 m to 1.9 m using a step 0.05 m. For each height, by simulating the gait kinematics, if the point C_2 is found to be inside a box $[b_0]$ of the search space P_0 then it is considered as included in P .

```

[Q,F]=Get_Worksapce_and_Wrench( $P_0,\varepsilon_p,\varepsilon_r,m,t_{gc},BWS$ )
for h from 1.4 to 1.9
  [x,y, $\phi$ ,f]=Dynamic_Simulation( $h,m,t_{gc},BWS$ )
  for i from 1 to size(x)
    p=Intersection( $P_0,(x(i),y(i))$ )
    if (p  $\neq \emptyset$ ) then
      k=k+1
      P(k) $\leftarrow$ (p)
      S(k) $\leftarrow$ ( $\phi(i),f(i)$ )
    endif
  endfor
endfor
[Q,F]=Sort(P,S, $\varepsilon_p$ )
return(Q,F)

```

Figure 64: Algorithm of workspace and external wrench evaluation.

In addition, using the gait kinematics and the dynamic simulation, for each position of C_2 the orientation of the leg ϕ and the actuation wrench $f=(F_{cdrx}, F_{cdry}, M_{cdtz})^T$ are stored such that we associate for each box $[p_i]$ of P the corresponding orientations $[\phi]$ and wrenches $[f]$. Lastly, for every box $[p_i]$, the workspace Q is organized by sorting the orientations by a step ε_r of 2° .

The implemented algorithm for the assessment of the workspace Q and the external wrench F is shown in Figure 64. The inputs are the initial search space P_0 , the width of position boxes ε_p , the sorting step of orientations ε_r , the body mass m , the amount of unloading BWS and the time of the GC t_{gc} . The outputs of the algorithm are the sets of the required workspace Q and the external wrench F . It is worth mentioning that Q and F are two sets having the same

cardinal. For any pose $[q_i]$ of Q , we have the corresponding wrench $[f_i]$, i.e., the external wrench is evaluated for every pose box $[q_i]$.

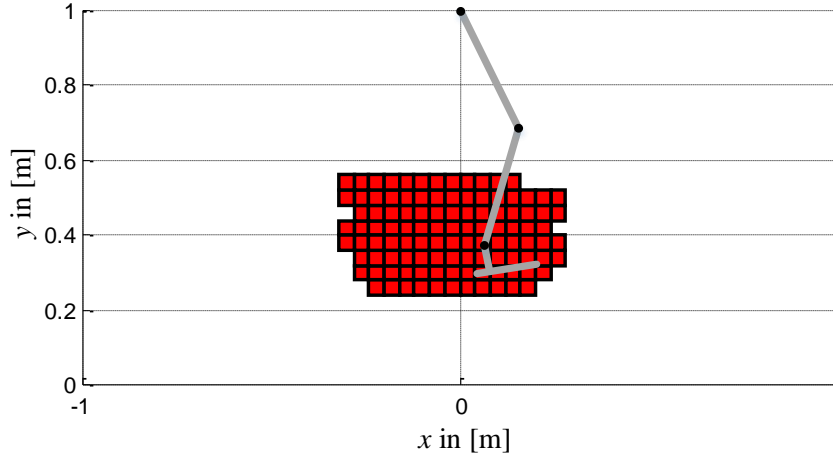


Figure 65: the required translational workspace P evaluated as a set of boxes.

As a result, the translational space P is visualized in Figure 65, the total number of translational boxes is 108. To show how orientations and wrenches are associated with position boxes, let's consider the box $[p_o] = ([-0.1601, -0.1199], [0.4399, 0.4801])^T$ centered at $(x, y)=(-0.14, 0.46)$. The corresponding boxes of orientations and wrenches are presented in Table 11. In total, for $[p_o]$ orientation ϕ varies from -59.76 to -56.61 and from -19.19 to -16.06 . For example if ϕ is located within $[-19.19, -17.23]$ then the applied moment varies from 4.08 Nm to 4.77 Nm.

Therefore for each translational box $[p_i]$ of P , we have the associated boxes of orientations $[\phi]$, forces $[F_{cdrx}]$, $[F_{cdry}]$ and moments $[M_{cdrz}]$. Lastly, the required workspace Q is evaluated into 632 pose boxes. Hereafter, the set Q and F are used as inputs for the design algorithm of CDPMs. More precisely they will be employed to write the equilibrium of the CDLM.

Table 11: Orientation and external wrench of a box $[b_o]$ centred at $(x,y)=(-0.14,0.46)$.

Orientation $[\phi]$ [Deg]	Force $[F_{cdrx}]$ [N]	Force $[F_{cdry}]$ [N]	Moment $[M_{cdrz}]$ [N.m]
[-59.76, -57.78]	[-42.40, 6.83]	[159.90, 196.66]	[18.05, 27.15]
[-57.67, -56.61]	[8.82, 27.30]	[195.67, 201.31]	[16.91, 19.68]
[-19.19, -17.23]	[113.82, 125.05]	[161.97, 180.18]	[4.08, 4.77]
[-17.11, -16.06]	[100.70, 114.24]	[181.29, 192.02]	[4.67, 4.97]

5.1.1.2. Cable interference

On top of the equilibrium feasibility, an important issue is the cable interferences. In the case

of planar robots, cable/cable interference is not considered since cables can be placed in parallel planes but cable/end-effector interference cannot be avoided [156].

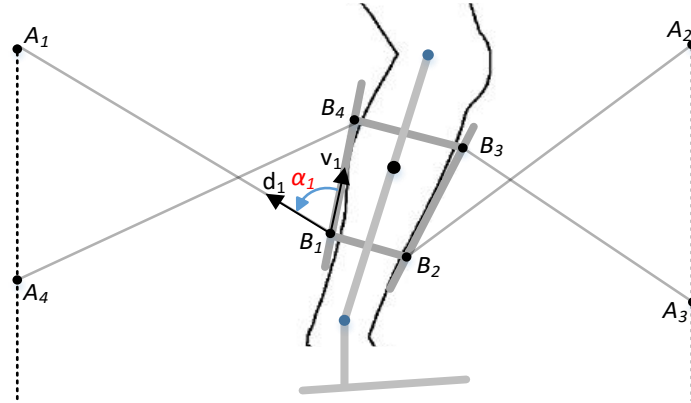


Figure 66: Cable/end-effector collision detection

Through angular measurements, this type of interference can be detected. For that, the following condition is defined to avoid cable/end-effector interference (see Figure 66):

$$\alpha_i = \angle(v_i, d_i) \text{ such that } 0 \leq \alpha_i \leq \pi, i = 1..4 \quad (53)$$

here for a cable i from 1 to 4, the value of the angle α_i constructed by vectors v_i and d_i , have to be between 0 and π , in order to guarantee that the cable i doesn't interfere with the end-effector.

5.1.2. Generation of optimal design parameters

Generation of optimal design parameters is accomplished through two stages: first we determine all feasible sets of design parameters and then we select an optimal one based on the following criterion: minimization of the maximum tension over all the cables.

5.1.2.1. Generation of all feasible sets of design parameters

Determination of the optimal locations of the cable exit points involves the use of the algorithm developed in Chapter 4 (figure 59). The algorithm is modified by adding an interference detection procedure (Figure 67), in order to get all feasible sets of solutions.

```

Feasible_Boxes(A,B,Q,[t],F,D,ε)
Lc = Get_Configurations(A,B,D,ε)
for i=1 to (size(Q))
    if (cable_interference(Lc(i))) then continue
    Lw = Evaluate_Transformation_Matrix(Lc,Q(i))
    Lf = Check_Feasibility(Lw,[t],F(i))
    Lc = Lf
end
return(Lf)
    
```

Figure 67: Algorithm of generation of feasible and collision-free configurations

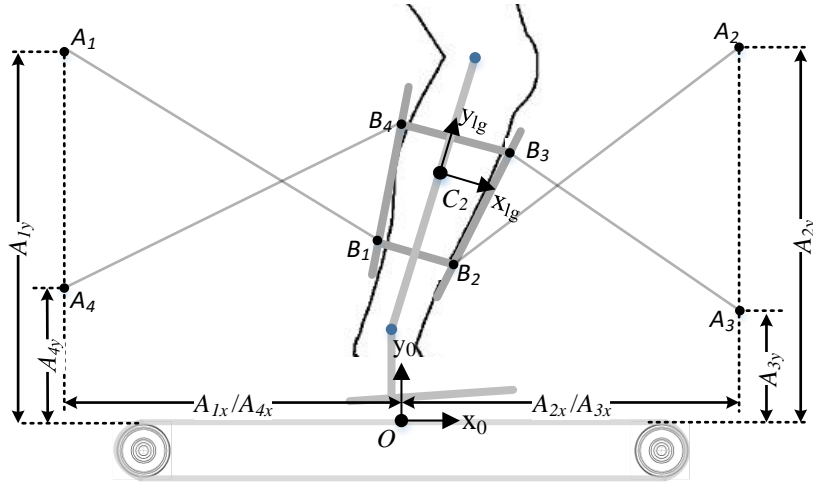


Figure 68: Design parameters of the CDLM: A_{1y} , A_{2y} , A_{3y} , A_{4y} , A_{1x}/A_{4x} and A_{2x}/A_{3x}

The design parameters D are: the A_{iy} coordinate of point A_i , A_{1x}/A_{4x} coordinate of points A_1 and A_4 , and A_{2x}/A_{3x} coordinate of points A_2 and A_3 (see Figure 68). For each parameter, an initial search range is selected and then discretized. Table 12 shows the bounds for the selected geometric parameters and the corresponding discretization steps ε . Thereby, a list L_c of the different configurations of the fixed mechanical frame, i.e., the different locations of points A_i are generated.

Table 12: Design parameters specifications.

	A_{1y}	A_{2y}	A_{3y}	A_{4y}	A_{1x}/A_{4x}	A_{2x}/A_{3x}
Lower bound	0.6	0.6	0	0	-0.8	0.8
Upper bound	1	1	0.4	0.4	-1	1
ε	0.02	0.02	0.02	0.02	0.02	0.02

Every configuration of L_c is processed, first the procedure *Cable_Interference()* detects possible collision over a GC. If no interference is encountered a feasibility test is executed (*Check_Feasibility()*). Hence, the list L_f contains all valid configurations.

In summary, a configurations is valid if two conditions are satisfied: it is feasible under the required space Q and the external wrench F, and there is no cable/end-effector collision. In the next section we will discuss the details of computing the optimal set of points A_i .

5.1.2.2. Generation of the optimal design parameters

Many valid configurations are found, thus we are asked to select an optimal one. Our optimization criterion is the configuration that minimizes the maximum tension over all the cables, i.e., the configuration that minimizes the maximum required torque over all the actuators.

```

Get_Optimal( $L_f$ )
for i from 1 to (size( $L_f$ ))
for h from 1.4 to 1.9
b = Compute_External_Wrench( $L_f(i), h$ )
t = Compute_Tensions( $L_f(i), b$ )
j = j + 1
 $L_t(j) = Max\_Curve(t)$ 
endfor
 $L_m(i) = \max(L_t)$ 
endfor
index = Get_Index_Minimum( $L_m$ )
 $C_o = L_f(\text{index})$ 

```

Figure 69: Algorithm of generation of the optimal design

A last algorithm is developed in order to get the optimal configurations (Figure 69). For each valid configuration of the list L_f , the tension curves of the cables are computed ($Compute_Tensions()$) during a GC. Then the overall maximum value is determined ($Max_Curve()$).

To explain the procedure $Max_Curve()$, the following case is considered: a body height of 1.7 m and a given valid configuration of A_i points: $(A_{1y}, A_{2y}, A_{3y}, A_{4y}, A_{1x}/A_{4x}, A_{2x}/A_{3x}) = (0.9, 0.7, 0, 0, -1, 1)$. The obtained tensions in the cables are shown in Figure 70(a) and Figure 70(b) for the on-ground and off-ground cases, respectively. The maximum tension is about 596 N found at 0.72 s in Cable 2 during the on-ground walking.

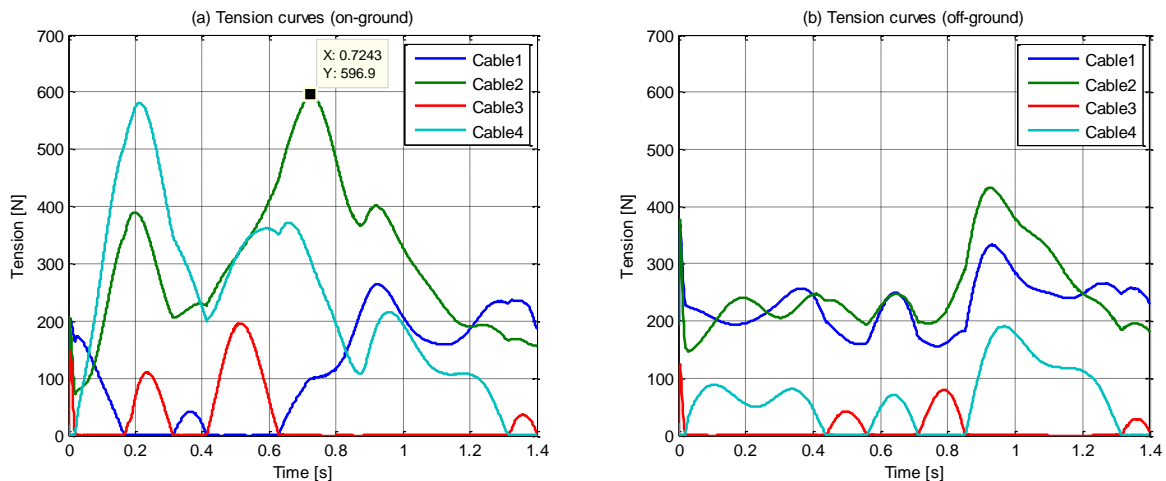


Figure 70: Curves of cable tensions: (a) On-ground walking, and (b) Off-ground walking

While the list L_t (Figure 69) contains the maximum tensions as a function of both configurations and heights, the list L_m contains the maximum tensions for the configurations only. The function $Get_Index_Minimum()$ searches in the list L_m for the smallest value of the

tension t of t and returns its index. Based on the selected index, the optimal configuration is identified, which is given by the following crossed configuration: $C_o = (1, 0.82, 0, 0, -1, 1)$.

The design optimization algorithm allows us to get the configuration that minimizes the peak of the tension over all the cables. Thus, based on the found configuration, the next step is to compute the required power of the robot actuators.

5.1.3. Curves of simulated power requirements

Now the optimal design is assessed but the required power is not yet determined. Thus, based on the selected configuration C_o , the next step is to compute the curves of maximum tension over all heights h and whatever the walking case, i.e., on-ground or off-ground simulation. Here, cable tensions are computed through the minimization procedure introduced in Section 4.1.1 as follows:

$$\min\left(\sum_i^m t_i\right) \text{ subject to } W t = f \text{ and } t \geq 0 \quad (54)$$

Throughout a GC and for every time frame, we compute the wrench f and the transformation matrix W , then the minimization (54) is executed to get the tension in the cables. Figure 71(a) shows, as an example, the tensions in cable 4 for heights $h=1.4$ m and $h=1.9$ m, and for the two walking scenarios. Figure 71(b) presents the maximum tension for the cable 4, which consists on determining the maximum tension over the curves of Figure 71(a) for every time frame.

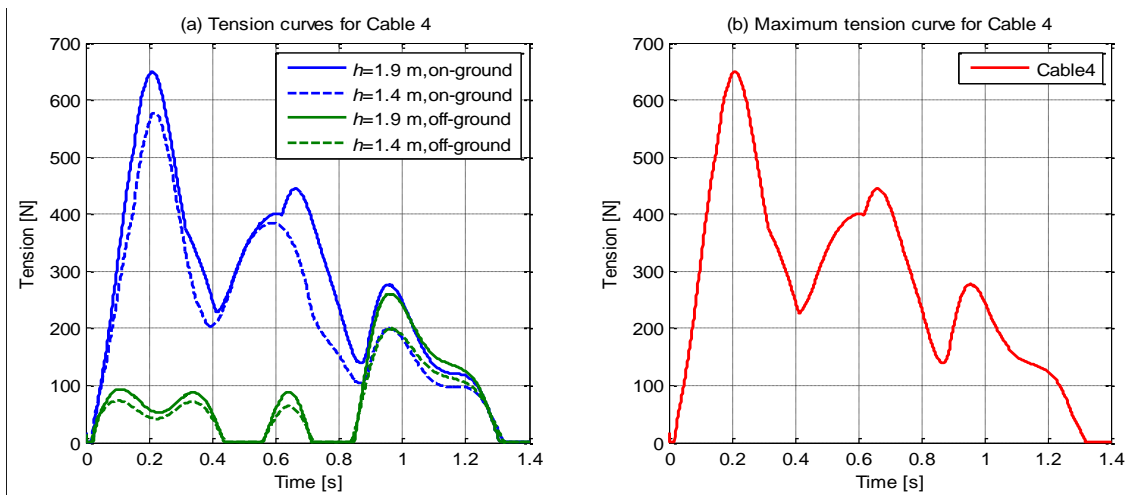


Figure 71: Determination of maximum tension for Cable 4

Hereafter, curves of maximum tensions for all the cables are plotted in Figure 72(a). To make a comparative study with a feasible but a non-optimal configuration, consider the configuration $C_{no} = (0.65, 0.65, 0, 0, 1, -1)$. The corresponding trajectories are shown in Figure 72(b). While for C_o the maximum is 657.3 N found in cable 2, for C_{no} it is about 757 N located

in cable 1 which is greater than the first value. Thus, C_o guarantees the minimum peak of the tension, consequently, the required torque of actuators is less significant.

In addition to tension information, the magnitude of the velocities of points B_i are computed. Hereafter, the maximum cable velocities are determined (see Figure 73). Once the maximum tensions and the linear velocities are calculated for all the cables, they are used to simulate the power curves (see Figure 74).

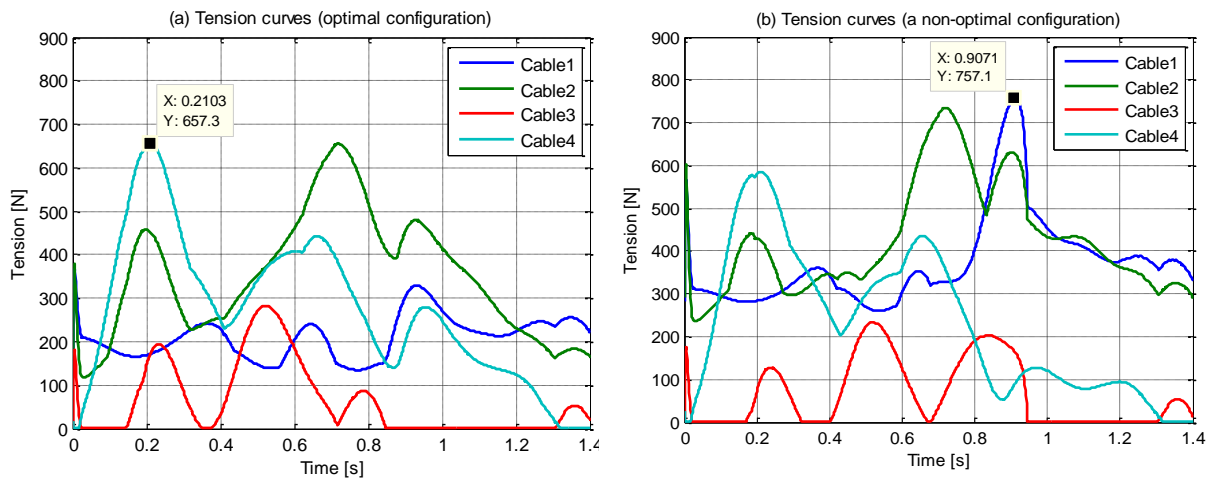


Figure 72: Maximum cable tensions for: (a) The optimal configuration, and (b) A non-optimal configuration

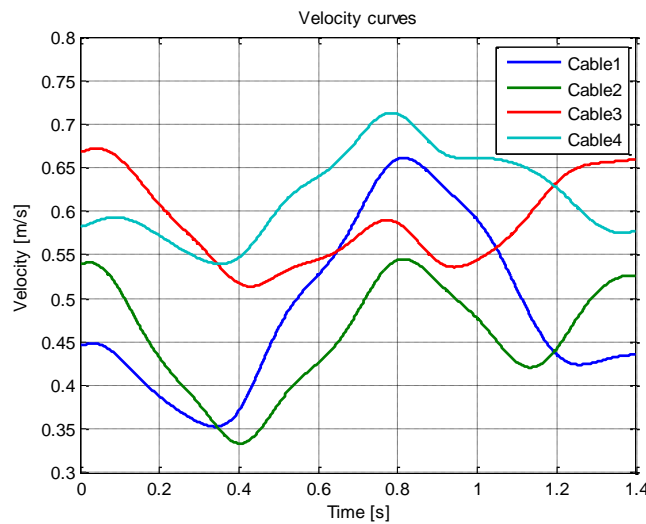


Figure 73: Maximum linear velocity of the cables

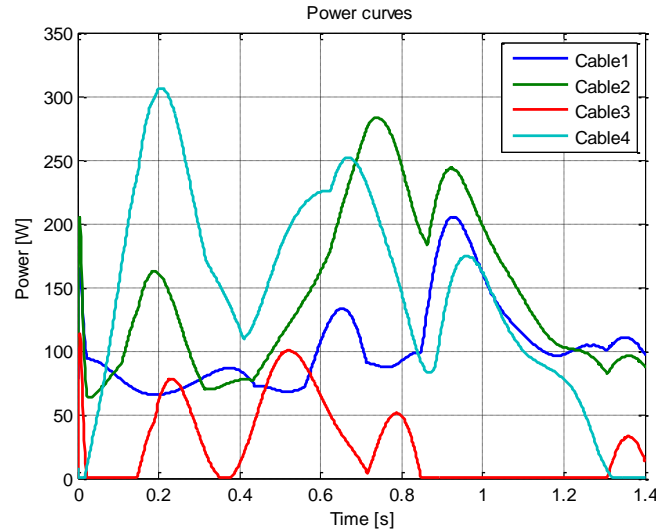


Figure 74: Simulated cables power

The maximum tensions and the linear velocities of all the cables are used to simulate the power curves (Figure 74). Cable 2 and cable 4 can only produce a positive torque (see Figure 63). Since the required torque is positive from 0.06s to 1.26s (see Figure 48-Figure 49). These cables are the most active ones, In fact, according to Figure 74, their curves dominate the others. Also one can observe that cable 1 and cable 2 exert an upward force (see Figure 63), then for the off-ground simulation (Figure 70(b)), these cables are the most active in order to keep the leg in the air. In contrast, cable 3 is the least active one because it generates a negative torque or a downward force. In fact, its required power vanishes during the swing phase (Figure 74).

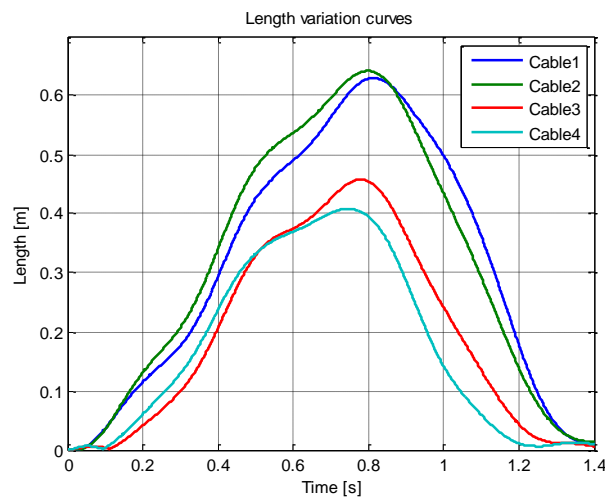


Figure 75: Length variation curves of cables for the optimal design

Lastly, an extra data to design the spooling system of cable is the cable length variation, which is presented in Figure 75. Maximum length is required in order to select, for a given diameter, the number of revolute on the spooling drum.

In the sequel, all the obtained curves will be used to get the specifications of the different parts of the cable drive mechanism.

5.2. Actuation Parts Selection of the CDLT

In this section, the actuation mechanisms of the CDLM and the BWSD are designed.

5.2.1. Actuators of the CDLM

In general, the drive unit of cables embodies 3 parts: a servo motor, a gear box and a spiral drum (Figure 76). Afterward, based on results of the first section specifications of each part will be determined.

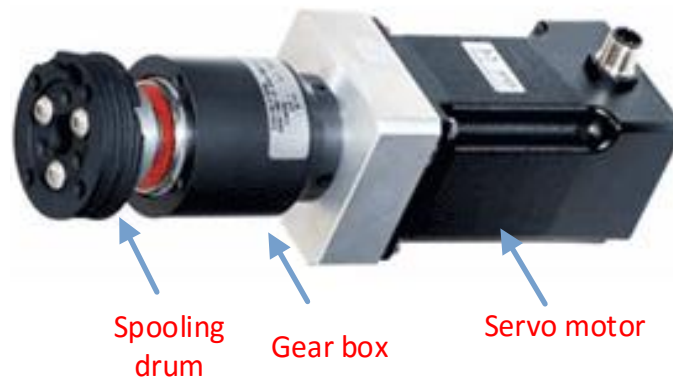


Figure 76: Cable drive unit [169]

Table 13 shows the highest values of the tension, linear velocity and power retrieved, respectively, from Figure 72(a), Figure 73 and Figure 74. As well, Average values are given.

Table 13: Maximum and average requirements of cable actuation system.

	Cable 1	Cable 2	Cable 3	Cable 4
Maximum tension [N]	368.1	655.22	282.76	657.35
Average tension [N]	210.4	353.22	61.39	276.05
Maximum velocity [m.s ⁻²]	0.661	0.545	0.672	0.713
Average velocity [m.s ⁻²]	0.49	0.45	0.59	0.62
Maximum power [W]	205.45	283.02	113.28	306.62
Average power [W]	103.46	146.21	24.51	147.74

The design of the cable drive unit is not a simple task. However, the following steps are adopted:

i)-At the beginning, we set the maximum speed of spooling of cables n_{spc} to 250 rpm. Then, by considering the maximum velocity of cables (Table 13) and according to Eq (55) the corresponding diameters of the spooling drums (D_{spc}) are in mm: 50.5, 41.7 51.4 and 54.5. Thereby, one may choose a single value $D_{\text{spc}}=55$ mm for all the drums.

$$D_{\text{spc}} = 60.V_{\text{max}} / \pi.n_{\text{spc}} \quad (55)$$

ii)-In relation to Figure 75, the maximum length L_{max} over all the cables is 0.65 m, then the minimum number of revolute for the drums is: $N_{\text{revc}} = L_{\text{max}} / (\pi.D_{\text{spc}}) = 3.7$. One may choose $N_{\text{rev}}=5$.

iii)-Taking into account that the maximum rpm of the servo motor is 5000 rpm, thus, the gear box ratio is: $i_{\text{gbc}} = 5000 / 250 = 20$.

iv)-Relying on Eq (56) and by considering Table 13, the maximum and the average values of the torque, the rotational speed and the torque of the spooling motors are calculated and presented in

Table 14.

$$\begin{aligned} \tau &= (t \cdot D_{\text{spc}}) / (2 \cdot i_{\text{gbc}}) \quad : \text{Torque [Nm]} \\ n &= (60.V.i_{\text{gbc}}) / (\pi.D_{\text{spc}}) \quad : \text{Rotational speed [rpm]} \\ P &= 2\pi.\tau.n / 60 \quad : \text{Power [W]} \end{aligned} \quad (56)$$

Table 14: Maximum and mean requirement for the servo motors.

	motor 1	motor 2	motor 3	motor 4
Maximum speed [rpm]	4592.53	3786.56	4668.43	4951.79
Average speed [rpm]	3405.56	3179.85	4064.66	4306.83
Maximum torque [Nm]	0.51	0.9	0.39	0.9
Average torque [Nm]	0.29	0.49	0.084	0.38
Maximum power [W]	243.42	357.24	190.07	468.7
Average power [W]	103.17	161.73	35.93	171.19

Consequently, a single selection of the motor for all the cables is the Parker DC servo motor RS240B (see Appendix 4.1). The nominal performances of this motor are: (0.39 Nm, 3000rpm) and the maximum allowed are: (1.3 Nm, 5500 rpm). For the reduction unit, we chose the planetary gear box head Parker PV40FB (see Appendix 4.2). It has a ratio of 20 and a nominal output torque of 6.5 Nm.

5.2.2. Actuators of the BWSD

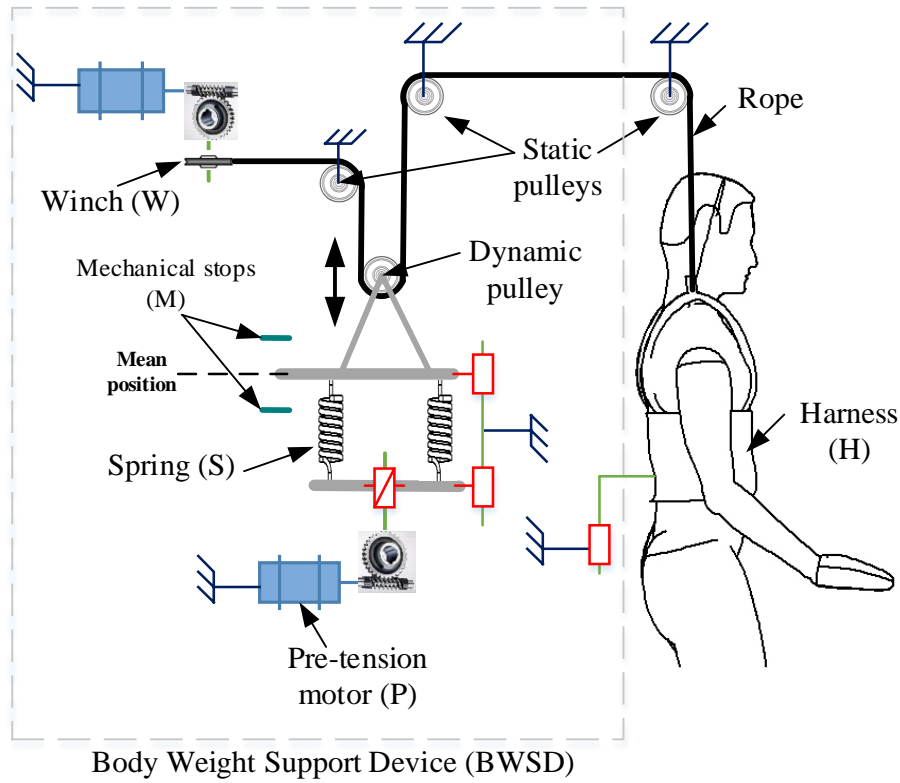


Figure 77: Diagram of the body weight support system

Two active mechanisms are included in the BWSD: the first (W) serves to lift the patient from a sitting to a standing posture and the second one (P) adjusts the springs offset in order to select the amount of unloading.

5.2.2.1. Electric Winch

The electric winch includes a DC motor, a worm gear box and a spooling drum. The average speed of lifting is $V_{lf} = 3.3$ cm/s [170] and the lifting capacity is up to $F_{lf} = 120$ kg. Here, the chosen diameter of the spooling Drum is $D_{spw} = 60$ mm, then the required torque and spooling speed are:

$$\begin{aligned}\tau_{drw} &= F_{lf} \cdot g \cdot D_{spw} / 2 = 35.32 \text{ Nm} \\ n_{drw} &= (60 \cdot V_{lf}) / (\pi \cdot D_{spw}) = 10.5 \text{ rpm}\end{aligned}\quad (57)$$

A Hydromec Q45 (41Nm) worm gear box with a ratio $i_{gbw} = 102$ is selected (See Appendix 4.3). Further, its efficiency is $\eta_{gbw} = 0.49$, therefore the requirements of the motor are:

$$\begin{aligned}\tau_{mw} &= \tau_{drw} / (i_{gbw} \cdot \eta_{gbw}) = 0.6 \text{ Nm} \\ n_{mw} &= n_{drw} \cdot i_{gbw} = 1261 \text{ rpm}\end{aligned}\quad (58)$$

By examining the curves of the servo motor integrated in the cable spooling unit (Parker RS 240B, see Appendix 4.1), one can use it also for the electric winch.

5.2.2.2. Pre-tension mechanism

The pre-tension mechanism integrates a motor, a worm gear box and a power screw. The output average speed is $V_p = 0.5$ cm/s [170] and the unloading capacity is about $F_{uc} = 80$ kg.

A trapezoidal power screw (XCF6200) having a diameter $D_{sc} = 16$ mm and a pitch $p = 4$ mm is selected (Appendix 4.4). Taking into account that its efficiency is approximately $\eta_{sc} = 0.47$, then the required torque and rotational speed on the screw are:

$$\begin{aligned} \tau_{sc} &= 2 \cdot F_{uc} \cdot g \cdot D_{sc} / (2 \cdot \eta_{sc}) = 26.72 \text{ Nm} \\ n_{sc} &= (60 \cdot V_p) / p = 75 \text{ rpm} \end{aligned} \quad (59)$$

A Hydromec Q30 (21Nm) worm gear box with a ratio $i_{pgb} = 40$ is chosen (see Appendix 4.5). Note that its efficiency is $\eta_{pgb} = 0.57$, therefore the requirements of the motor are:

$$\begin{aligned} \tau_{mp} &= \tau_{sc} / (i_{pgb} \cdot \eta_{pgb}) = 1.17 \text{ Nm} \\ n_{mp} &= n_{sc} \cdot i_{pgb} = 3000 \text{ rpm} \end{aligned} \quad (60)$$

The motor parker RS 240B (Appendix 4.1) is suitable to actuate the pre-tension mechanism.

So far, all the actuation mechanisms are dimensioned and selected. Thus, in the following section we will present the conceptual design of the CDLT.

5.3. Presentation of the CAD Design of the CDLT

The design of the experimental device CDLT is presented in Figure 78. The fixed frame is made out of aluminium profiles allowing an easy configurability. A four bars mechanism is attached to the harness and hence guides the vertical motion of the body. The BWSD as a one unit is assembled on the back of the fixed frame. For the spooling system, a cable exits from the cable drive unit and then is directed to the orthosis via a pulley.

Besides, parts of the BWSD are shown in Figure 79, the two sliding parts translate along two guidance shafts through housing bearings. The dynamic pulley is attached to the upper sliding part in order to transmit the unloading force. Furthermore, the position of the lower sliding part is set through a power screw/sleeve system.

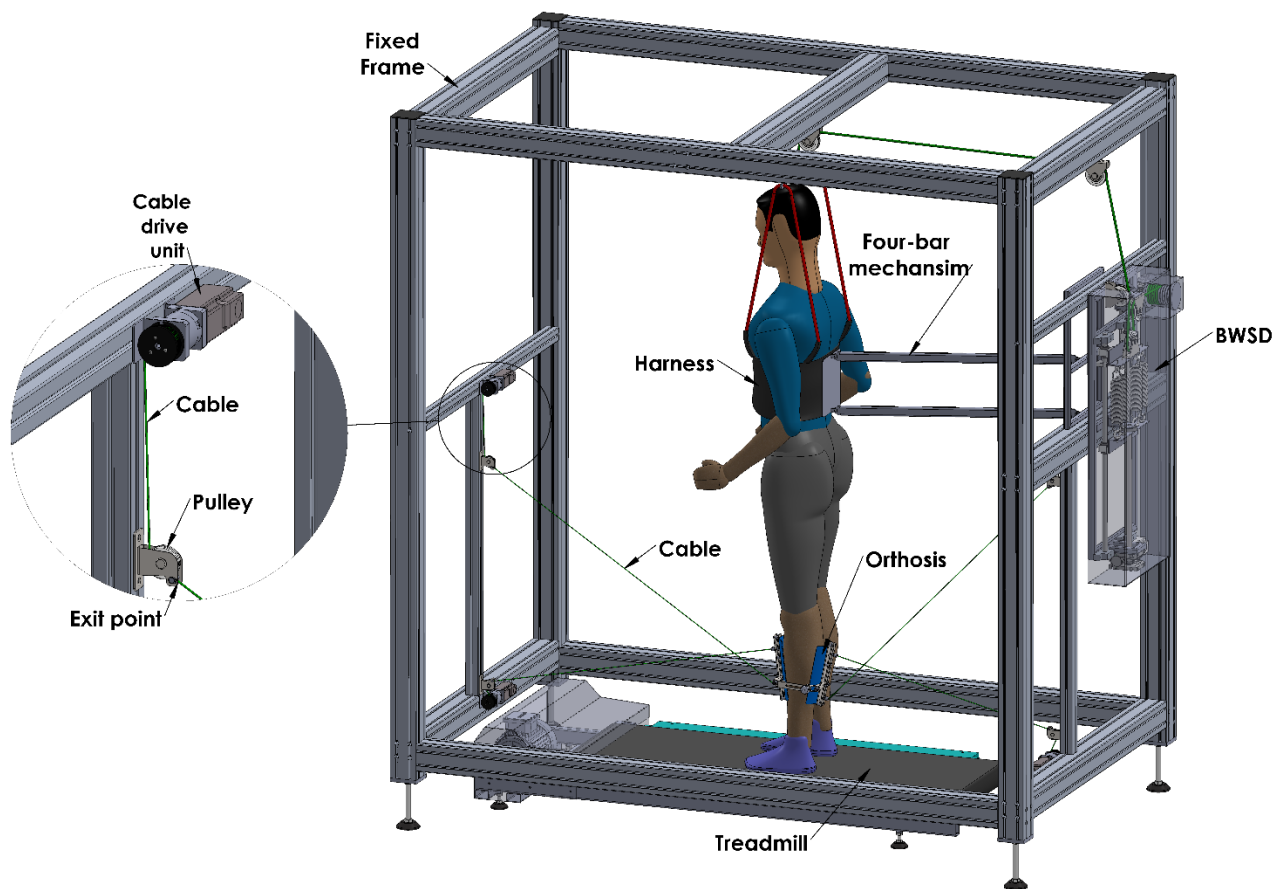


Figure 78: The CAD Design of the CDLT.

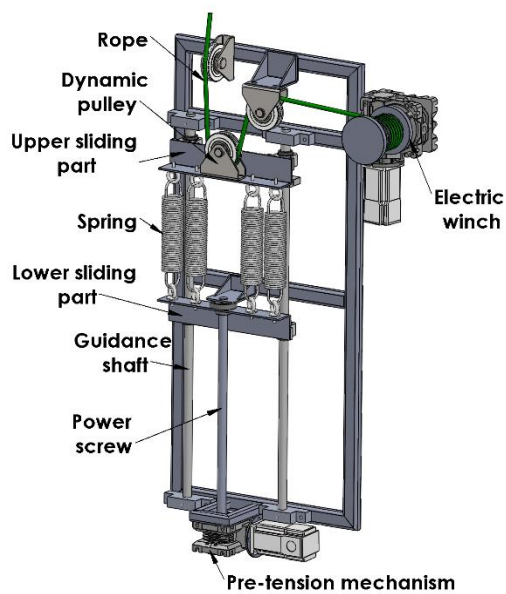


Figure 79: Inside the BWSD.

Conclusion:

A design study and an actuation analysis have been carried out in this chapter. Throughout, the mechanical sub-systems of the CDLT, i.e., the CDLM and the BWSD were designed.

First, we investigated the design of the CDLM. For that, the required space and wrenches were assessed as a set of boxes. Feasible designs were generated using the developed algorithm in Chapter 4. In addition, a collision detection procedure was addressed. Thereby, valid designs satisfying the two conditions: a non-negative tension in the cables and a free cable/end-effector collision, were determined. Among all valid designs, the optimal one was the configuration that minimizes the peak of the tensions in all the cables. Afterwards, a power analysis was conducted in order to size the robot actuators.

Based on the obtained curves, specifications of the cable drive unit were determined and suitable components were chosen. In addition, actuation parts of the BWSD were also seized. Lastly, the CAD solution of the CDLT was presented

6. Discussion and Concluding Remarks

In this research, the design of a gait rehabilitation machine based on a cable-driven robot, called the CDLT, was investigated. Throughout, a full design approach was provided and described.

Gait training aims at assisting disabled patients to reproduce the gait pattern, and hence, to be able to walk again. So far, various gait trainers have been developed, only a few of them were commercialized. Most of these machines have high cost and complexity. As an alternative to classical rigid robots, the use of CDPMs is a promising solution. Indeed, due to its simplicity and low cost, CDPMs are an attractive solution for rehabilitation. However, from a design point of view, the study of cable robots is a challenging problem where one has to take advantage of the use of cables while overcoming its limitations. The proposed CDLT machine includes two mechanisms: a BWSD that maintains the patient in a vertical posture over a treadmill, and a CDLM that controls the lower limb movement in the sagittal plane by means of a cable robot. The effector of the cable robot consists of an orthosis attached to the leg. Thereby, the CDLT allows the patients to practice walking in a safe condition.

6.1. Gait Experiment and Walking Data

The substantial information for the development of the CDLT was the spatio-temporal specifications of the gait cycle. An experiment was conducted to get the kinematics and the dynamics of a normal gait. Although similar information is available in the literature, we preferred conducting our own experimentation so that the analysis protocol is consistent with the target application. Furthermore, trajectories of a normal gait may differ among research laboratories due to several dispersing problems. In fact, if we examine the gait function of the same subject in different centers, results may vary more or less significantly.

The equipment used in the gait experiment is made of a Vicon motion capture system and a set of force platforms. A Healthy person was equipped with a set of reflective markers, their positions allowed us to determine the joint trajectories of the lower limb. By moving the joints of the lower limb in close ranges to those occurring during walking, the sphere fitting method was used to identify the CoRs. The fitting was achieved through geometrical, algebraic and Pratt algorithms. Results were shown to be close and any one of these methods may be employed, the same observation can be found in [112]. Benefits of this functional method is that the CoR is located regardless of the placement's accuracy of the markers on specific anatomical landmarks. However, the motion of the markers in relation to the bones, known as soft-tissue artifact, is still a problematic issue. Optimization approaches could be investigated

in order to improve the accuracy of the marker motion [171]. After computing the different CoRs, the angular motions of the different segment were evaluated.

All the retrieved curves, including motion trajectories and the ground reactions, were smoothed through the use of the Butterworth filter, then they were scaled to one gait cycle. Furthermore, for the ground reaction the amplitude was normalized relative to the body weight.

One may notice that the use of the overground walking data as a target motion for an upright treadmill walking may not be the optimal solution, due the probable existence of a difference between these two modes of walking. The obtained data can be used to estimate the required power of actuation.

6.2. Dynamic Simulation of Treadmill Walking

The experimentally obtained walking data were exploited to carry out an inverse dynamic simulation of the CDLT. The lower limb is driven using the leg orthosis, in order to determine the required actuation wrench to drive the limb during a gait cycle. Furthermore, the target performance was the kinematics of the normal gait.

The human body was modeled as a four segment articulated mechanism. Length, mass and inertia specifications of each segment were retrieved from anthropometric data. Only two parameters were required to retrieve all the data, i.e., the mass and the height of the body.

The body was subjected to three external forces: the weight, the unloading force and the ground reaction. Solving of the inverse dynamic model was achieved using two different methods: Newton-Euler and a Matlab SimMechanics Model.

Considering a body having a mass of 100 kg and a height of 1.7 m, the required wrench was calculated during a gait cycle of 1.4 s. The actuation wrench was evaluated at the leg CoM for two situations: on-ground and off-ground walking. Taking into account both cases is essential, since the time when the required cable tensions are the highest is unknown.

Results using the analytical method (Newton-Euler) and the computer simulation (SimMechanics) were similar, which validated the method. Note that the SimMechanics model is simpler to implement since it does not require the use of the explicit equations of motion. However, the required computational time is higher in the case of SimMechanics.

Note that for this simulation, the patient participation to achieve the walking movement was not taken into account, which is the worst case in calculating the cable tensions. By adding the contribution of the muscles, the carried simulation could be employed in order to assess the progress of gait recovery by computing the difference between the required and the measured actuation wrenches.

6.3. Design of CDMPs Using Interval Analysis

The main subsystem of the CDLT is the CDLM. One of the contributions of this research, is the development of an approach on designing CDMPs for a desired workspace using interval analysis.

The workspace analysis of CDMPs is usually carried out by means of wrench-feasibility, i.e., the equilibrium of a particular pose is achieved with non-negative bounded tensions in the cables. Thus, for the analysis of the CDMPs workspace, one has to find all the feasible poses of the mobile platform. The design problem was presented as follows: given a required workspace, specific external loads and a set of design parameters, find the feasible parameters that satisfy the wrench-feasibility condition. Conversely to discrete paradigms that treat the workspace as a grid of points, by means of interval analysis, we examined the workspace as an entire range. Indeed, the equilibrium of the CDPM was written in its interval form then its wrench-feasibility was verified using a strong-feasibility theorem.

The developed algorithm is capable of finding all possible solutions where an optimal design can be selected in relation to a user defined criterion. Effectiveness of the algorithm was illustrated by designing two CDMPs: a planar robot and a spatial one. All feasible designs were found such that the wrench-feasibility condition is guaranteed, hence the desired space is a WFW and is free from singularities.

Due to the dependence and the wrapping effects, we noted that the number of feasible solutions is sensitive to the size of the pose boxes. By bisecting the desired space into narrow boxes, new feasible designs were found but a higher computational time was recorded. In order to lessen the effect of overestimation, an optimization based evaluation of the transformation matrix was applied. An open challenge is to find a compromise between the size of the pose boxes and a reasonable computational time. It is worth mentioning that a prohibitive computational time may be found for discrete methods when using a finer grid.

While the main downside of the interval method is its high computational time and results overestimation, the obtained solutions are certified with respect to the rounding errors and they are reliable over all the desired workspace and the connection points' uncertainty boxes. On the contrary, results of discrete methods are only valid for a finite number of poses, and for each pose the results are potentially sensitive to rounding errors.

To sum up, interval analysis provides reliable and robust results but the high computation time could be a limiting factor in using this method. The interpreter nature of MATLAB can also explain this important computation time. Using the C language could be a possible alternative to speed the calculation. Development of new optimized numerical

algorithms and implementation of parallel computing can also contribute to reducing the required computational time.

6.4. Design of the CDLT

The CDLT machine has two main sub-systems: the CDLM and the BWSD. We particularly focused on the design of the CDLM. The training machine was designed to be adaptable with a range of height, varying from 1.4 m to 1.9 m. The maximum amount of unloading is 80 kg and the maximum walking speed corresponds to a gait cycle time of 1.4s.

Using the gait data and the inverse dynamic simulation, the required workspace and external wrenches of the CDLM were evaluated as a set of boxes. Inputting these requirements to the design algorithm of Chapter 4, feasible designs of the CDLM were determined. In addition, a procedure of collision detection between the cables and the end-effector was added to the algorithm. The optimal design was selected as the one that minimizes the maximum of cable tensions over all the cables.

Once the geometry of the CDLM was determined, the power requirement was simulated. Thereby, specifications of the cable drive units were selected. Besides, the actuation parts of the BWSD were also seized. Lastly, a CAD design was provided and described.

While for this work the optimization criterion is the maximum tension in the cables, one can select other criteria depending on the application and the wish of the designer. Minimizing the cable velocity, the cable power or the overall power consumption, could be an alternative choice for the optimization criterion.

Moreover, tensions were determined by minimizing the sum of cable tensions, this objective function may be modified in order to better estimate the distribution of tensions over all the cable.

6.5. Future Scope

In this work, a cable-based gait training machine was developed and designed. As a next step, an ongoing work is underway to build this device and then to evaluate it through healthy persons.

For the actual design, we were limited to the motion of the lower limb in the sagittal plane. The cable robot is reconfigurable and versatile, thus more DOFs may be added in order to allow a more natural gait.

Investigating a control system for the CDLT is essential. For a position control strategy, it is required to generate adequate cable trajectories to reproduce the gait pattern. However, to

implement a patient-cooperative approach, tensions in the cables must be measured in order to evaluate the contribution of the muscle forces. Thereby, recovery progress can also be assessed.

Appendices

Appendix 1: Anthropometric data [127]

TABLE 4.1 Anthropometric Data

Segment	Definition	Segment Weight/Total Body Weight	Center of Mass/Segment Length		Radius of Gyration/Segment Length		Density	
			Proximal	Distal	C of G	Proximal		Distal
Hand	Wrist axis/knuckle II middle finger	0.006 M	0.506	0.494 P	0.297	0.587	0.577 M	1.16
Forearm	Elbow axis/ulnar styloid	0.016 M	0.430	0.570 P	0.303	0.526	0.647 M	1.13
Upper arm	Glenohumeral axis/elbow axis	0.028 M	0.436	0.564 P	0.322	0.542	0.645 M	1.07
Forearm and hand	Elbow axis/ulnar styloid	0.022 M	0.682	0.318 P	0.468	0.827	0.565 P	1.14
Total arm	Glenohumeral joint/ulnar styloid	0.050 M	0.530	0.470 P	0.368	0.645	0.596 P	1.11
Foot	Lateral malleolus/head metatarsal II	0.0145 M	0.50	0.50 P	0.475	0.690	0.690 P	1.10
Leg	Femoral condyles/medial malleolus	0.0465 M	0.433	0.567 P	0.302	0.528	0.643 M	1.09
Thigh	Greater trochanter/femoral condyles	0.100 M	0.433	0.567 P	0.323	0.540	0.653 M	1.05
Foot and leg	Femoral condyles/medial malleolus	0.061 M	0.606	0.394 P	0.416	0.735	0.572 P	1.09
Total leg	Greater trochanter/medial malleolus	0.161 M	0.447	0.553 P	0.326	0.560	0.650 P	1.06
Head and neck	C7-T1 and 1st rib/ear canal	0.081 M	1.000	— PC	0.495	0.116	— PC	1.11
Shoulder mass	Stenoclavicular joint/glenohumeral axis	—	0.712	0.288	—	—	—	1.04
Thorax	C7-T1/T12-L1 and diaphragm*	0.216 PC	0.82	0.18	—	—	—	0.92
Abdomen	T12-L1/L4-L5*	0.139 LC	0.44	0.56	—	—	—	—
Pelvis	L4-L5/greater trochanter*	0.142 LC	0.105	0.895	—	—	—	—
Thorax and abdomen	C7-T1/L4-L5*	0.355 LC	0.63	0.37	—	—	—	—
Abdomen and pelvis	T12-L1/greater trochanter*	0.281 PC	0.27	0.73	—	—	—	1.01
Trunk	Greater trochanter/glenohumeral joint*	0.497 M	0.50	0.50	—	—	—	1.03
Trunk head neck	Greater trochanter/glenohumeral joint*	0.578 MC	0.66	0.34 P	0.503	0.830	0.607 M	—
Head, arms, and trunk (HAT)	Greater trochanter/glenohumeral joint*	0.678 MC	0.626	0.374 PC	0.496	0.798	0.621 PC	—
HAT	Greater trochanter/mid rib	0.678	1.142	—	0.903	1.456	—	—

*NOTE: These segments are presented relative to the length between the greater trochanter and the glenohumeral joint. Source Codes: M, Dempster via Miller and Nelson; *Biomechanics of Sport*, Lea and Febiger, Philadelphia, 1973. P, Dempster via Plagenhoef; *Patterns of Human Motion*, Prentice-Hall, Inc. Englewood Cliffs, NJ, 1971. L, Dempster via Plagenhoef from living subjects; *Patterns of Human Motion*, Prentice-Hall, Inc., Englewood Cliffs, NJ, 1971. C, Calculated.

Appendix 2: dynamic and kinematic data

Newton-Euler equations:

Upper body equilibrium

$$F_{\text{uby}} = \alpha \cdot (-m_{\text{ub}} + m_{\text{oth}}) \cdot g + k((m \cdot g \cdot BWS)/k + \Delta y/2) - (m_{\text{ub}} + m_{\text{oth}}) \cdot a_{\text{uby}}$$

Thigh equilibrium

$$F_{\text{thx}} = -(I_{\text{th}} \cdot \dot{\omega}_{\text{thz}} - (C_1 H)_x \cdot F_{\text{uby}} + (C_1 K)_x \cdot F_{\text{uby}} + (C_1 H)_y \cdot a_{\text{thx}} \cdot m_{\text{th}} - (C_1 K)_x \cdot a_{\text{thy}} \cdot m_{\text{th}} - (C_1 K)_x \cdot g \cdot m_{\text{th}}) / ((C_1 H)_y - (C_1 K)_y)$$

$$F_{\text{thy}} = F_{\text{uby}} - a_{\text{thy}} \cdot m_{\text{th}} - g \cdot m_{\text{th}}$$

Foot equilibrium

Stance phase

$$F_{\text{ftx}} = -a_{\text{ftx}} \cdot m_{\text{ft}} - R_{\text{grx}} \cdot (F_{\text{uny}} - g \cdot m_{\text{b}})$$

$$F_{\text{fity}} = -a_{\text{fity}} \cdot m_{\text{ft}} - g \cdot m_{\text{ft}} - R_{\text{gry}} \cdot (F_{\text{uny}} - g \cdot m_{\text{b}})$$

$$F_{\text{lr}} = \|F_{\text{lr}}\| \cdot (P_1 P_2 / \|P_1 P_2\|) \text{ such that } \|F_{\text{lr}}\| = 0$$

Swing phase

$$F_{\text{ftx}} = (I_{\text{ft}} \cdot (P_1 P_2)_x \cdot \dot{\omega}_{\text{ftz}} + (C_3 A)_x \cdot (P_1 P_2)_x \cdot a_{\text{fity}} \cdot m_{\text{ft}} - (C_3 A)_x \cdot (P_1 P_2)_y \cdot a_{\text{ftx}} \cdot m_{\text{ft}} + (C_3 P_2)_x \cdot (P_1 P_2)_y \cdot a_{\text{ftx}} \cdot m_{\text{ft}} - (C_3 P_2)_y \cdot (P_1 P_2)_x \cdot a_{\text{ftx}} \cdot m_{\text{ft}} + (C_3 A)_x \cdot (P_1 P_2)_x \cdot g \cdot m_{\text{ft}}) / ((C_3 A)_x \cdot (P_1 P_2)_y - (C_3 A)_y \cdot (P_1 P_2)_x - (C_3 P_2)_x \cdot (P_1 P_2)_y + (C_3 P_2)_y \cdot (P_1 P_2)_x)$$

$$F_{\text{fity}} = (I_{\text{ft}} \cdot (P_1 P_2)_y \cdot \dot{\omega}_{\text{ftz}} + (C_3 A)_y \cdot (P_1 P_2)_x \cdot a_{\text{fity}} \cdot m_{\text{ft}} - (C_3 A)_y \cdot (P_1 P_2)_y \cdot a_{\text{ftx}} \cdot m_{\text{ft}} + (C_3 P_2)_x \cdot (P_1 P_2)_y \cdot a_{\text{fity}} \cdot m_{\text{ft}} - (C_3 P_2)_y \cdot (P_1 P_2)_x \cdot a_{\text{fity}} \cdot m_{\text{ft}} + (C_3 A)_y \cdot (P_1 P_2)_x \cdot g \cdot m_{\text{ft}} + (C_3 P_2)_x \cdot (P_1 P_2)_y \cdot g \cdot m_{\text{ft}} - (C_3 P_2)_y \cdot (P_1 P_2)_x \cdot g \cdot m_{\text{ft}}) / ((C_3 A)_x \cdot (P_1 P_2)_y - (C_3 A)_y \cdot (P_1 P_2)_x - (C_3 P_2)_x \cdot (P_1 P_2)_y + (C_3 P_2)_y \cdot (P_1 P_2)_x)$$

$$F_{\text{lr}} = \|F_{\text{lr}}\| \cdot (P_1 P_2 / \|P_1 P_2\|) \text{ such that}$$

$$\|F_{\text{lr}}\| = -(I_{\text{ft}} \cdot \dot{\omega}_{\text{ftz}} + (C_3 A)_x \cdot a_{\text{fity}} \cdot m_{\text{ft}} - (C_3 A)_y \cdot a_{\text{ftx}} \cdot m_{\text{ft}} + (C_3 A)_x \cdot g \cdot m_{\text{ft}}) / ((C_3 A)_x \cdot (P_1 P_2)_y - (C_3 A)_y \cdot (P_1 P_2)_x - (C_3 P_2)_x \cdot (P_1 P_2)_y + (C_3 P_2)_y \cdot (P_1 P_2)_x)$$

Leg equilibrium

$$F_{\text{cdrx}} = a_{\text{lgx}} \cdot (m_{\text{lg}} + m_{\text{or}}) - F_{\text{lr}} - F_{\text{thx}} - F_{\text{ftx}}$$

$$F_{\text{cdry}} = g \cdot (m_{\text{lg}} + m_{\text{or}}) - F_{\text{lry}} - F_{\text{thy}} - F_{\text{fity}} + a_{\text{lgy}} \cdot (m_{\text{lg}} + m_{\text{or}})$$

$$M_{\text{cdrz}} = \dot{\omega}_{\text{lgz}} \cdot (I_{\text{lg}} + I_{\text{or}}) - (C_2 A)_x \cdot F_{\text{fity}} + (C_2 A)_y \cdot F_{\text{ftx}} - (C_2 P_1)_x \cdot F_{\text{lry}} + (C_2 P_1)_y \cdot F_{\text{lr}} - (C_2 K)_x \cdot F_{\text{thy}} + (C_2 K)_y \cdot F_{\text{thx}}$$

Kinematic equations:

Pose equations of lower limb's segments computed at CoMs:

$$\begin{pmatrix} {}^0C_{1x} \\ {}^0C_{1y} \\ \phi_{th} \end{pmatrix} = \begin{pmatrix} -C_{1y} \cdot \sin(\theta_{hip}) \\ H_y + C_{1y} \cdot \cos(\theta_{hip}) \\ \theta_{hip} \end{pmatrix}$$

$$\begin{pmatrix} {}^0C_{2x} \\ {}^0C_{2y} \\ \phi_{lg} \end{pmatrix} = \begin{pmatrix} C_{2y} \cdot \sin(\theta_{knee} - \theta_{hip}) - K_y \cdot \sin(\theta_{hip}) \\ H_y + K_y \cdot \cos(\theta_{hip}) + C_{2y} \cdot \cos(\theta_{knee} - \theta_{hip}) \\ \theta_{hip} - \theta_{knee} \end{pmatrix}$$

$$\begin{pmatrix} {}^0C_{3x} \\ {}^0C_{3y} \\ \phi_{ft} \end{pmatrix} = \begin{pmatrix} C_{3x} \cdot \cos(\theta_{knee} - \theta_{ankle} - \theta_{hip}) + C_{3y} \cdot \sin(\theta_{knee} - \theta_{ankle} - \theta_{hip}) - K_y \cdot \sin(\theta_{hip}) + A_y \cdot \sin(\theta_{knee} - \theta_{hip}) \\ H_y + C_{3y} \cdot \cos(\theta_{knee} - \theta_{ankle} - \theta_{hip}) + K_y \cdot \cos(\theta_{hip}) - C_{3x} \cdot \sin(\theta_{knee} - \theta_{ankle} - \theta_{hip}) + A_y \cdot \cos(\theta_{knee} - \theta_{hip}) \\ \theta_{hip} - \theta_{knee} + \theta_{ankle} \end{pmatrix}$$

Position equations of lower limb's vectors:

Vector C_1H

$$(C_1H)_x = C_{1y} \cdot \sin(\theta_{hip})$$

$$(C_1H)_y = -C_{1y} \cdot \cos(\theta_{hip})$$

Vector C_1K

$$(C_1K)_x = \sin(\theta_{hip}) \cdot (C_{1y} - K_y)$$

$$(C_1K)_y = -\cos(\theta_{hip}) \cdot (C_{1y} - K_y)$$

Vector C_3A

$$(C_3A)_x = -C_{3x} \cdot \cos(\theta_{knee} - \theta_{ankle} - \theta_{hip}) - C_{3y} \cdot \sin(\theta_{knee} - \theta_{ankle} - \theta_{hip})$$

$$(C_3A)_y = C_{3x} \cdot \sin(\theta_{knee} - \theta_{ankle} - \theta_{hip}) - C_{3y} \cdot \cos(\theta_{knee} - \theta_{ankle} - \theta_{hip})$$

Vector C_3P_2

$$(C_3P_2)_x = P_{2x} \cdot \cos(\theta_{knee} - \theta_{ankle} - \theta_{hip}) - C_{3x} \cdot \cos(\theta_{knee} - \theta_{ankle} - \theta_{hip}) - C_{3y} \cdot \sin(\theta_{knee} - \theta_{ankle} - \theta_{hip}) + P_{2y} \cdot \sin(\theta_{knee} - \theta_{ankle} - \theta_{hip})$$

$$(C_3P_2)_y = P_{2y} \cdot \cos(\theta_{knee} - \theta_{ankle} - \theta_{hip}) - C_{3y} \cdot \cos(\theta_{knee} - \theta_{ankle} - \theta_{hip}) + C_{3x} \cdot \sin(\theta_{knee} - \theta_{ankle} - \theta_{hip}) - P_{2x} \cdot \sin(\theta_{knee} - \theta_{ankle} - \theta_{hip})$$

Vector P_2P_1

$$(P_1P_2)_x = P_{2x} \cdot \cos(\theta_{knee} - \theta_{ankle} - \theta_{hip}) + P_{2y} \cdot \sin(\theta_{knee} - \theta_{ankle} - \theta_{hip}) - P_{1x} \cdot \cos(\theta_{knee} - \theta_{hip}) + A_y \cdot \sin(\theta_{knee} - \theta_{hip}) - P_{1y} \cdot \sin(\theta_{knee} - \theta_{hip})$$

$$(P_1P_2)_y = P_{2y} \cdot \cos(\theta_{knee} - \theta_{ankle} - \theta_{hip}) - P_{2x} \cdot \sin(\theta_{knee} - \theta_{ankle} - \theta_{hip}) + A_y \cdot \cos(\theta_{knee} - \theta_{hip}) - P_{1y} \cdot \cos(\theta_{knee} - \theta_{hip}) + P_{1x} \cdot \sin(\theta_{knee} - \theta_{hip})$$

Vector C_2K

$$(C_2K)_x = -C_{2y} \cdot \sin(\theta_{knee} - \theta_{hip})$$

$$(C_2K)_y = -C_{2y} \cdot \cos(\theta_{knee} - \theta_{hip})$$

Vector C₂A

$$(C_2A)_x = \sin(\theta_{knee} - \theta_{hip}) \cdot (A_y - C_{2y})$$

$$(C_2A)_y = \cos(\theta_{knee} - \theta_{hip}) \cdot (A_y - C_{2y})$$

Vector C₂P₁

$$(C_2P_1)_x = P_{1x} \cdot \cos(\theta_{knee} - \theta_{hip}) - C_{2y} \cdot \sin(\theta_{knee} - \theta_{hip}) + P_{1y} \cdot \sin(\theta_{knee} - \theta_{hip})$$

$$(C_2P_1)_y = P_{1y} \cdot \cos(\theta_{knee} - \theta_{hip}) - C_{2y} \cdot \cos(\theta_{knee} - \theta_{hip}) - P_{1x} \cdot \sin(\theta_{knee} - \theta_{hip})$$

Appendix 3: Robot equilibrium equations

The general form of the equilibrium

$$Wt = f$$

where

$$W = \begin{pmatrix} d_1 & \cdots & d_m \\ b_1 \times d_1 & \cdots & b_m \times d_m \end{pmatrix}$$

and

$$d_i = B_i A_i / \|B_i A_i\|, \quad b_i = P B_i$$

Planar case:

Pose q:

$$q = (P_x \quad P_y \quad \phi)^T$$

Rotation matrix R:

$$R = \begin{bmatrix} \cos(\phi) & -\sin(\phi) & 0 \\ \sin(\phi) & \cos(\phi) & 0 \\ 0 & 0 & 1 \end{bmatrix}$$

Transformation matrix W:

$$B_i A_i = \begin{pmatrix} A_x - P_x - B_x \cos(\phi) + B_y \sin(\phi) \\ A_y - P_y - B_y \cos(\phi) - B_x \sin(\phi) \end{pmatrix}$$

$$b_i = \begin{pmatrix} B_x \cos(\phi) - B_y \sin(\phi) \\ B_y \cos(\phi) + B_x \sin(\phi) \end{pmatrix}$$

$$W_{1j} = (1 / \|B_i A_i\|) (A_x - P_x - B_x \cos(\phi) + B_y \sin(\phi))$$

$$W_{2j} = (1 / \|B_i A_i\|) (A_y - P_y - B_y \cos(\phi) - B_x \sin(\phi))$$

$$W_{3j} = (1 / \|B_i A_i\|) (-(B_y \cos(\phi) + B_x \sin(\phi))(A_x - P_x - B_x \cos(\phi) + B_y \sin(\phi)) - ((B_x \cos(\phi) - B_y \sin(\phi))(P_y - A_y + B_y \cos(\phi) + B_x \sin(\phi))))$$

Spatial case:

Pose q:

$$q = (P_x \quad P_y \quad P_z \quad \alpha \quad \beta \quad \gamma)^T$$

Rotation matrix R:

$$R = \begin{bmatrix} \cos(\alpha)\cos(\beta) & -\sin(\alpha)\cos(\gamma) + \cos(\alpha)\sin(\beta)\sin(\gamma) & \sin(\alpha)\sin(\gamma) + \cos(\alpha)\sin(\beta)\cos(\gamma) \\ \sin(\alpha)\cos(\beta) & \cos(\alpha)\cos(\gamma) + \sin(\alpha)\sin(\beta)\sin(\gamma) & -\cos(\alpha)\sin(\gamma) + \sin(\alpha)\sin(\beta)\cos(\gamma) \\ -\sin(\beta) & \cos(\beta)\sin(\gamma) & \cos(\beta)\cos(\gamma) \end{bmatrix}$$

Transformation matrix W:

$$B_i A_i = \begin{pmatrix} A_x - P_x + B_y (\cos(\gamma)\sin(\alpha) - \cos(\alpha)\sin(\beta)\sin(\gamma)) - B_z (\sin(\alpha)\sin(\gamma) + \cos(\alpha)\cos(\gamma)\sin(\beta)) - B_x \cos(\alpha)\cos(\beta) \\ A_y - P_y - B_y (\cos(\alpha)\cos(\gamma) + \sin(\alpha)\sin(\beta)\sin(\gamma)) + B_z (\cos(\alpha)\sin(\gamma) - \cos(\gamma)\sin(\alpha)\sin(\beta)) - B_x \cos(\beta)\sin(\alpha) \\ A_z - P_z + B_x \sin(\beta) - B_z \cos(\beta)\cos(\gamma) - B_y \cos(\beta)\sin(\gamma) \end{pmatrix}$$

$$b_i = \begin{pmatrix} B_z (\sin(\alpha)\sin(\gamma) + \cos(\gamma)\cos(\gamma)\sin(\beta)) - B_y (\cos(\gamma)\sin(\alpha) - \cos(\alpha)\sin(\beta)\sin(\gamma)) + B_x \cos(\alpha)\cos(\beta) \\ B_y (\cos(\alpha)\cos(\gamma) + \sin(\alpha)\sin(\beta)\sin(\gamma)) - B_z (\cos(\alpha)\sin(\gamma) - \cos(\gamma)\sin(\alpha)\sin(\beta)) + B_x \cos(\beta)\sin(\alpha) \\ B_z \cos(\beta)\cos(\gamma) - B_x \sin(\beta) + B_y \cos(\beta)\sin(\gamma) \end{pmatrix}$$

$$W_{1j} = (1 / \|B_i A_i\|) (-P_x - A_x - B_y (\cos(\gamma)\sin(\alpha) - \cos(\alpha)\sin(\beta)\sin(\gamma)) + B_z (\sin(\alpha)\sin(\gamma) + \cos(\alpha)\cos(\gamma)\sin(\beta)) + B_x \cos(\alpha)\cos(\beta))$$

$$W_{2j} = (1 / \|B_i A_i\|) (-P_y - A_y + B_y (\cos(\alpha)\cos(\gamma) + \sin(\alpha)\sin(\beta)\sin(\gamma)) - B_z (\cos(\alpha)\sin(\gamma) - \cos(\gamma)\sin(\alpha)\sin(\beta)) + B_x \cos(\beta)\sin(\alpha))$$

$$W_{3j} = (1 / \|B_i A_i\|) (-P_z - A_z - B_x \sin(\beta) + B_z \cos(\beta)\cos(\gamma) + B_y \cos(\beta)\sin(\gamma))$$

$$W_{4j} = (1 / \|B_i A_i\|) ((B_z \cos(\beta) \cos(\gamma) - B_x \sin(\beta) + B_y \cos(\beta) \sin(\gamma)) (P_y - A_y + B_y (\cos(\alpha) \cos(\gamma) + \sin(\alpha) \sin(\beta) \sin(\gamma)) - B_z (\cos(\alpha) \sin(\gamma) - \cos(\gamma) \sin(\alpha) \sin(\beta)) + B_x \cos(\beta) \sin(\alpha)) - ((B_y (\cos(\alpha) \cos(\gamma) + \sin(\alpha) \sin(\beta) \sin(\gamma)) - B_z (\cos(\alpha) \sin(\gamma) - \cos(\gamma) \sin(\alpha) \sin(\beta)) + B_x \cos(\beta) \sin(\alpha)) (P_z - A_z - B_x \sin(\beta) + B_z \cos(\beta) \cos(\gamma) + B_y \cos(\beta) \sin(\gamma)))$$

$$W_{5j} = (1 / \|B_i A_i\|) ((B_z (\sin(\alpha) \sin(\gamma) + \cos(\alpha) \cos(\gamma) \sin(\beta)) - B_y (\cos(\gamma) \sin(\alpha) \cos(\alpha) \sin(\beta) \sin(\gamma)) + B_x \cos(\alpha) \cos(\beta)) (P_z - A_z - B_x \sin(\beta) + B_z \cos(\beta) \cos(\gamma) + B_y \cos(\beta) \sin(\gamma)) - ((B_z \cos(\beta) \cos(\gamma) - B_x \sin(\beta) + B_y \cos(\beta) \sin(\gamma)) (P_x - A_x - B_y (\cos(\gamma) \sin(\alpha) - \cos(\alpha) \sin(\beta) \sin(\gamma)) + B_z (\sin(\alpha) \sin(\gamma) + \cos(\alpha) \cos(\gamma) \sin(\beta)) + B_x \cos(\alpha) \cos(\beta)))$$

$$W_{6j} = (1 / \|B_i A_i\|) ((B_y (\cos(\alpha) \cos(\gamma) + \sin(\alpha) \sin(\beta) \sin(\gamma)) - B_z (\cos(\alpha) \sin(\gamma) - \cos(\gamma) \sin(\alpha) \sin(\beta)) + B_x \cos(\beta) \sin(\alpha)) (P_x - A_x - B_y (\cos(\gamma) \sin(\alpha) - \cos(\alpha) \sin(\beta) \sin(\gamma)) + B_z (\sin(\alpha) \sin(\gamma) + \cos(\alpha) \cos(\gamma) \sin(\beta)) + B_x \cos(\alpha) \cos(\beta)) - ((B_z (\sin(\alpha) \sin(\gamma) + \cos(\alpha) \cos(\gamma) \sin(\beta)) - B_y (\cos(\gamma) \sin(\alpha) - \cos(\alpha) \sin(\beta) \sin(\gamma)) + B_x \cos(\alpha) \cos(\beta)) (P_y - A_y + B_y (\cos(\alpha) \cos(\gamma) + \sin(\alpha) \sin(\beta) \sin(\gamma)) - B_z (\cos(\alpha) \sin(\gamma) - \cos(\gamma) \sin(\alpha) \sin(\beta)) + B_x \cos(\beta) \sin(\alpha)))$$

Appendix 4: Technical data

Servo motor: Parker DC Servo Motor RS240B

192-003012N1
086358

High Performance DC Servo Motor - RS Series
www.parker.com/ssd/rs

High Performance DC Servo Motor - RS Series

Overview

Description

Using high energy magnets, RS DC motors combined with RTS drives are particularly suitable for applications which require a very compact solution or a high dynamic level.

Characteristics and advantages

- High performance characteristics
- Excellent low-speed functioning
- High compactness
- Very long service life
- Rare earth magnets
- Tacho, encoder resolver and brake in option

Features

- **Shaft**
 - RS1 to RS4: Smooth full shaft
 - RS5 and RS6: Full keyed shaft
- **2nd Shaft end**
 - RS1 to RS3: possibility to mount standard tacho or encoder
 - RS5 and RS6: possibility to mount standard tacho, adaptation for encoder mounting in option
- **Output cables 1 m without connector**
- **Options**
 - Brake (RS2 to RS6)
 - Tachometer
 - Adaptation 2nd shaft end for encoder mounting (RS5 and RS6)



Technical Characteristics - Overview

Motor type	DC motors with rare earth magnets
Number of poles	4
Protection degree	RS1 to RS4: IP40 RS5 and RS6: IP54
Insulation	Class F
Torque at low speed	0.05 ... 13 Nm
Permanent current at low speed	1.5 ... 28 A
Rated voltage	20.7 ... 105 V
Rated speed	2 000 ... 3 000 min ⁻¹
Rotor inertia	2.4 ... 8 300 kgmm ²

High Performance DC Servo Motor - RS Series
Technical Data

Technical Data

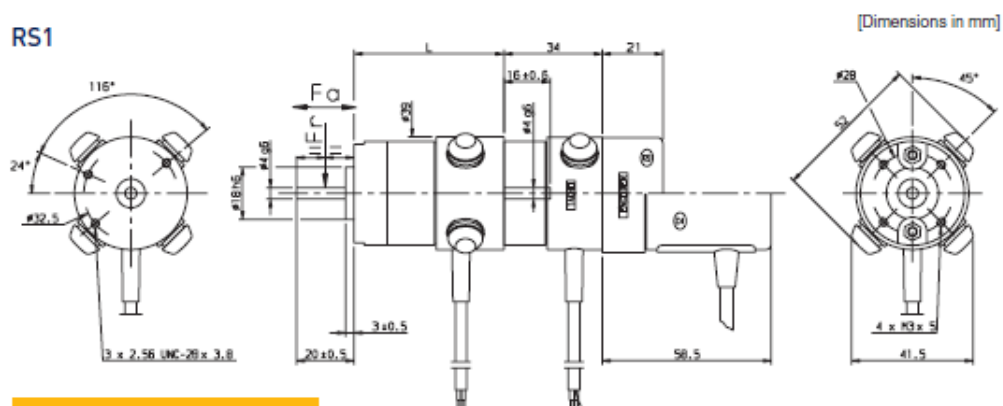
Torque at low speed M_0 [Nm]	Permanent current at low speed I_0 [A]	Rated Voltage U [V]	Rated Speed N [min ⁻¹]	Rotor Inertia [kgmm ²]	Product Code			Typical combination
0.05	1.5	20.7	3000	2.4	RS110MR1	■	00	RTS 3/10-40M
0.092	2.3	21.2	3000	4.1	RS120GR1	■	00	RTS 3/10-40M
0.13	2.7	23.7	3000	5.8	RS130ER1	■	00	RTS 3/10-40M
0.11	2.5	24	3000	13	RS210LR1	■	00	RTS 3/10-40M
0.225	4.1	25.4	3000	195	RS220FR1	■	00	RTS 10/20-60 ⁽¹⁾
0.232	2.8	38.6	3000	195	RS220KR1	■	00	RTS 3/10-40M
0.31	5.6	24	3000	26	RS230CR1	■	00	RTS 10/20-60 ⁽¹⁾
0.39	6	27.6	3000	325	RS240BR1	■	00	RTS 10/20-60 ⁽¹⁾
0.28	2.6	49	3000	54	RS310NR1	■	00	RTS 10/20-60 ⁽¹⁾
0.54	4.5	49	3000	83	RS320HR1	■	00	RTS 10/20-60 ⁽¹⁾
0.78	5.9	51	3000	110	RS330ER1	■	00	RTS 10/20-60 ⁽¹⁾
0.98	6.9	53	3000	140	RS340CR1	■	00	RTS 10/20-60 ⁽¹⁾
0.48	3.6	60	3000	137	RS410RR1	■	00	RTS 10/20-60 ⁽¹⁾
0.93	6.2	60	3000	225	RS420JR1	■	00	RTS 10/20-60 ⁽¹⁾
1.3	8.1	43	2000	310	RS430FR1	■	00	RTS 10/20-60 ⁽¹⁾
1.36	6.6	78	3000	310	RS430HR1	■	00	RTS 12/24-130 T
1.74	7	90	3000	400	RS440GR1	■	00	RTS 12/24-130 T
1.9	7.9	82	2700	1000	RS510LR1	■	00	RTS 12/24-130 T
3.1	10.9	92	2700	1350	RS520GR1	■	00	RTS 12/24-130 T
4	13	97	2700	1700	RS530ER1	■	00	RTS 20/40-130 T
5	15	104	2700	2050	RS540CR1	■	00	RTS 20/40-130 T
8	22.3	100	2400	5300	RS620GR1	■	00	RTS 40/80-190 T
10.8	25	100	2000	6800	RS630FR1	■	00	RTS 40/80-190 T
13	28	105	2000	8300	RS640ER1	■	00	RTS 40/80-190 T

⁽¹⁾ M = single phase or T = three phase

High Performance DC Servo Motor - RS Series
Dimensions

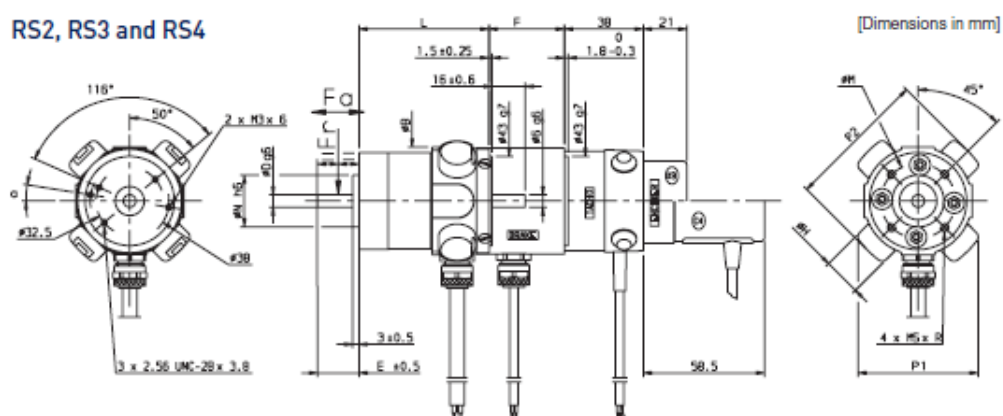
Dimensions

RS1



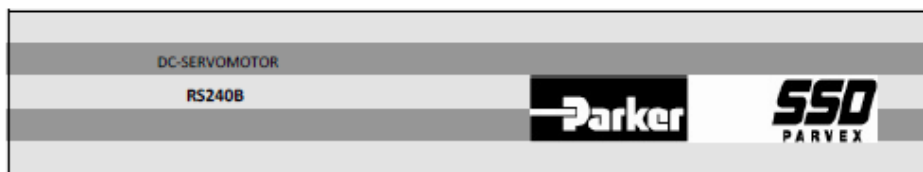
RS1 dimensions				
Motor	L	Weight [kg]	Fr ⁽¹⁾ [daN]	Fa ⁽¹⁾ [daN]
RS110	52.1	0.27	6	3
RS120	68.1	0.36	6	3
RS130	84.1	0.45	6	3

RS2, RS3 and RS4



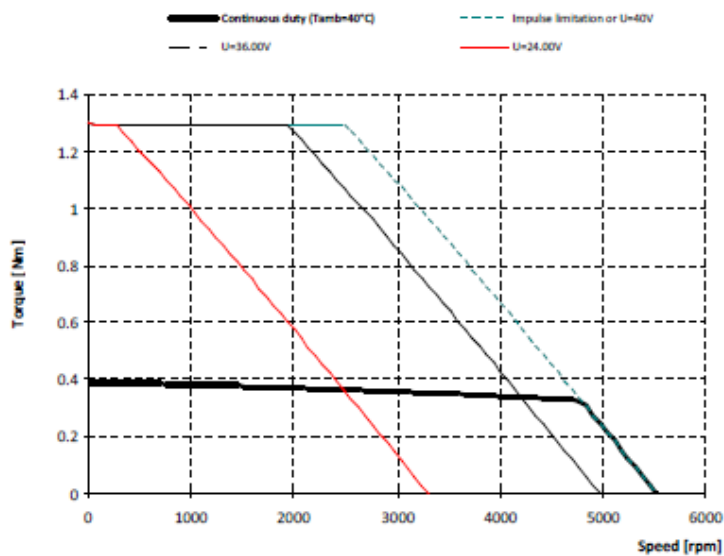
RS2, RS3 and RS4 with brake, tacho and encoder dimensions															
Motor	a	N	D	E	B	L	F	P1	P2	H	MSxR	M	Weight [kg]	Fr ⁽¹⁾ [daN]	Fa ⁽¹⁾ [daN]
RS210	9°	25	6	20	52	63	36.4	58	68	18.5	M4x6	36	0.54	18	10
RS220	9°	25	6	20	52	79	36.4	58	68	18.5	M4x6	36	0.7	18	10
RS230	9°	25	6	20	52	95	36.4	58	68	18.5	M4x6	36	0.86	18	10
RS240	9°	25	6	20	52	111	36.4	58	68	18.5	M4x6	36	1	18	10
RS310	-	32	9	25	68	80.5	41	69	83	18.5	M5x8	45	0.9	28	15
RS320	-	32	9	25	68	100.5	41	69	83	18.5	M5x8	45	1.3	28	15
RS330	-	32	9	25	68	120.5	41	69	83	18.5	M5x8	45	1.6	28	15
RS340	-	32	9	25	68	140.5	41	69	83	18.5	M5x8	45	2	28	15
RS410	-	50	11	32	83	95.5	40	82	98	22	M5x8	65	1.2	40	20
RS420	-	50	11	32	83	115.5	40	82	98	22	M5x8	65	1.8	40	20
RS430	-	50	11	32	83	135.5	40	82	98	22	M5x8	65	2.4	40	20
RS440	-	50	11	32	83	155.5	40	82	98	22	M5x8	65	3	40	20

⁽¹⁾ Fr and Fa not cumulative



Low speed torque	0.39	N.m	M_0
Permanent current at low speed	6	A	I_0
Supply voltage with loaded motor	28	V	U
Definition speed	3000	rpm	N
Maximum supply voltage	40	V	U_{max}
Maximum speed	5500	rpm	N_{max}
Peak current	20	A	I_{max}
Back emf constant at 1000 rpm (25°C)*	7.15	V	K_e
Torque constant	0.068	N.m/A	K_t
Winding resistance(25°C)	0.68	Ω	R_b
Winding inductance	0.45	mH	L
Rotor inertia	0.0000325	kg.m ²	J
Thermal time constant	7.5	min	T_{th}
Motor mass	1.04	kg	M

All data are given in typical values under standard conditions.



FICHER-004

Création: 14 août 1987	Edition:	22/déc/2010	RS240B	.f
------------------------	----------	-------------	--------	----

Planetary Gearbox: Parker PV40FB, Ratio=20

In-Line
Planetary

PV Series Gearheads

Performance Specifications

Parameter	Units	Ratio	PV40/PV17	PV60/PV23	PV90/PV34	PV115/PV42	
Nominal Output Torque $T_{nom r}$	Nm (in-lb)	3	–	–	12.0 (106.200)	35 (309.75)	74 (654.90)
		4	5.9 (52.215)	18.9 (167.265)	56 (495.60)	111 (982.30)	
		5	6.2 (54.870)	19.6 (173.460)	58 (513.30)	115 (1017.70)	
		7	5.5 (48.675)	16.7 (147.795)	52 (460.20)	104 (920.40)	
		10	3.5 (30.975)	10.6 (93.810)	33 (292.05)	67 (592.95)	
		12	–	–	18.2 (161.070)	54 (477.90)	112 (991.20)
		15	–	–	19.4 (171.690)	58 (513.30)	120 (1062.00)
		16	6.5 (57.525)	–	–	–	–
		20	6.5 (57.525)	21.5 (190.275)	67 (592.95)	136 (1203.60)	
		25	6.7 (59.295)	20.0 (177.000)	63 (557.55)	126 (1115.10)	
		30	–	–	22.5 (199.275)	71 (628.35)	144 (1274.40)
		35	6.7 (59.295)	–	–	–	–
		40	6.5 (57.525)	21.5 (190.275)	67 (592.95)	136 (1203.60)	
		50	6.7 (59.295)	20.0 (177.000)	63 (557.55)	126 (1115.10)	
		70	5.5 (48.675)	16.7 (147.795)	52 (460.20)	104 (920.40)	
100	3.5 (30.975)	10.6 (93.810)	33 (292.05)	67 (592.95)			
Maximum Acceleration Output Torque ¹⁾ $T_{acc r}$	Nm (in-lb)	3	–	–	24.0 (212.400)	70 (619.50)	148 (1309.80)
		4, 5, 12, 15	11.8 (104.430)	36.4 (322.140)	108 (955.80)	222 (1964.70)	
		7, 70	11.0 (97.350)	33.4 (295.590)	104 (920.40)	208 (1840.80)	
		10, 100	7.0 (61.950)	21.2 (187.620)	66 (584.10)	134 (1185.90)	
		16, 20, 25, 30, 35, 40, 50	13.0 (115.050)	40.0 (354.000)	126 (1115.10)	252 (2230.20)	
Emergency Stop Output Torque ²⁾ $T_{em r}$	Nm (in-lb)	3, 4, 5, 12, 15, 16, 20, 25, 30, 35, 40, 50	16.0 (141.600)	55.0 (486.750)	170 (1504.50)	350 (3097.50)	
		7, 70	13.7 (121.245)	44.0 (389.400)	137 (1212.45)	290 (2466.50)	
		10, 100	9.2 (81.420)	39.0 (345.150)	122 (1079.70)	255 (2256.75)	
						20,000	
Nominal Input Speed $N_{nom r}$	RPM	3 – 100	4500	4000	3500	3000	
Maximum Input Speed $N_{max r}$	RPM	3 – 100	8000	6000	6000	5000	
Service Life	h	3 – 100					
Standard Backlash ³⁾	arc-min	3 – 10	<15	<12	<10	<8	
		15 – 100	<18	<16	<14	<12	
Efficiency at Nominal Torque	%	3 – 10	96				
		15 – 100	94				
Noise Level at 3000 RPM ⁴⁾	db	3 – 100	<60	<65	<65	<70	
Maximum Allowable Case Temperature	°C	3 – 100	-20 to 100				
Lubrication		3 – 100	Lifetime lubrication				
Mounting Position		3 – 100	Any				
Direction of Rotation		3 – 100	Same as Input				
Degree of Protection		3 – 100	IP64				
Maximum Weight	kg (lbs)	3 – 10	0.6 (1.2)	1.2 (2.5)	3.2 (7.0)	6.8 (13.5)	
		15 – 100	0.9 (2.0)	1.6 (3.5)	4.3 (9.5)	9.7 (19.3)	

1) $t_{acc} + t_{dec} = 0.2 (t_{acc} + t_{cont} + t_{dec})$ $T_{cont} = 0.25 T_{acc}$

2) Maximum of 1000 stops.

3) Measured at 2% of rated torque.

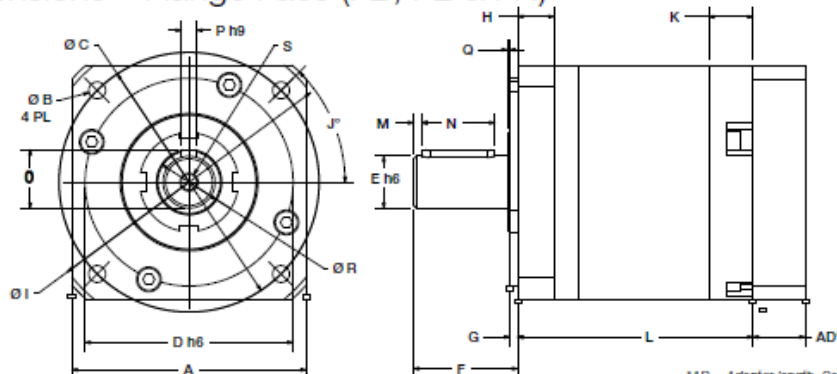
4) Measure at 1m. r – rated values



PV Series Gearheads



Dimensions – Flange Face (FB, FE & FN)



Metric & NEMA Frame Sizes

Frame Size	A		B		C		D		E		F		G		H		I		J	
	mm	in	mm	in	mm	in	mm	in	mm	in	mm	in	mm	in	mm	in	mm	in	°	
Metric	PV40FB	43	1.693	3.4	0.134	50	1.969	35	1.378	13	0.512	26	1.024	3	0.118	10	0.394	56	2.205	45
	PV60FB	62	2.441	5.5	0.217	70	2.756	50	1.969	16	0.630	25	0.984	2.5	0.098	10.3	0.406	80	3.150	45
	PV60FN	62	2.441	5.5	0.217	70	2.756	50	1.969	14	0.551	25	0.984	2.5	0.098	10.3	0.406	80	3.150	45
	PV90FB	90	3.543	8.5	0.256	100	3.937	80	3.150	20	0.787	40	1.575	3	0.118	14	0.551	116	4.567	45
	PV90FN	90	3.543	8.5	0.256	100	3.937	80	3.150	20	0.787	40	1.575	3	0.118	14	0.551	116	4.567	45
	PV115FB	115	4.528	8.5	0.335	130	5.118	110	4.331	24	0.945	50	1.969	3.5	0.138	18	0.709	152	5.984	45
PV115FN	115	4.528	8.5	0.335	130	5.118	110	4.331	25	0.984	55	2.165	3.5	0.138	18	0.709	152	5.984	45	
NEMA		in	mm	in	mm	in	mm	in	mm	in	mm	in	mm	in	mm	in	mm	in	mm	°
	PV17FE	1.693	43	0.138	3.5	1.724	43.8	0.866	22	0.250	6.35	0.984	25	0.059	1.5	0.236	6	2.165	55	45
	PV23FE	2.441	62	0.195	4.95	2.625	66.675	1.500	38.1	0.375	9.525	1.000	25.4	0.098	2.5	0.374	9.5	3.150	80	45
	PV34FE	3.543	90	0.217	5.52	3.875	98.43	2.875	73.025	0.500	12.7	1.250	31.75	0.118	3	0.591	15	4.567	116	45
PV42FE	4.528	115	0.281	7.14	4.949	125.7	2.187	55.55	0.625	15.875	1.500	38.1	0.094	2.4	0.787	20	5.984	152	45	
Frame Size	K		L1		L2		M		N		O		P		Q		R		S	
	mm	in	mm	in	mm	in	mm	in	mm	in	mm	in	mm	in	mm	in	mm	in	mm	
Metric	PV40FB	11	0.433	48.5	1.909	63	2.480	2.1	0.083	16	0.630	15	0.591	5	0.197	2	0.079	17.831	0.702	M4x8
	PV60FB	16	0.630	71.5	2.815	91.5	3.602	3.2	0.126	16	0.630	18	0.709	5	0.197	1	0.039	28	1.102	M5x12
	PV60FN	16	0.630	71.5	2.815	91.5	3.602	3.2	0.126	16	0.630	16	0.630	5	0.197	1	0.039	28	1.102	M5x12
	PV90FB	17	0.670	90.5	3.563	114	4.488	3.197	0.126	28	1.102	22.5	0.886	6	0.236	1	0.039	38	1.496	M6x12
	PV115FB	23	0.906	114.5	4.508	148.5	5.846	4.2	0.165	40	1.575	27	1.063	8	0.315	1.5	0.059	40	1.575	M10x22
	PV115FN	23	0.906	114.5	4.508	148.5	5.846	4.2	0.165	40	1.575	27	1.063	8	0.315	1.5	0.059	40	1.575	M10x22
NEMA		in	mm	in	mm	in	mm	in	mm	in	mm	in	mm	in	mm	in	mm	in	mm	
	PV17FE	0.433	11	1.909	48.5	2.480	63	-	-	-	-	-	-	-	-	0.091	2.3	0.458	11.633	-
	PV23FE	0.630	16	2.382	60.5	3.169	80.5	-	-	0.748	19	0.372	9.444	Flat	0.039	1	0.785	19.939	M5x12	
	PV34FE	0.670	17	3.228	82	4.154	105.5	-	-	1.063	27	0.561	14.247	0.125	3.175	0.039	1	0.984	25	M6x12
PV42FE	0.906	23	4.016	102	5.354	136	0.016	0.4	1.120	28.45	0.705	17.91	0.188	4.775	-	-	-	-	M6x20	

Parker Hannifin Corporation
Electromechanical Automation Division
Port Washington, New York

www.parkermotion.com

9

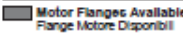
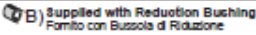
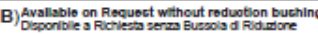
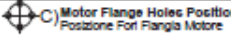


Worm gear box: Hydromec Q45 FB 102

Q45 Square - Gear **41Nm** Rating - Aluminum WORM GEARBOXES 

QUICK SELECTION / Selezione veloce input speed (n_i) = 1400 min⁻¹

Output Speed n ₂ [min ⁻¹]	Ratio i	Motor power P _{av} [kW]	Output torque M _{av} [Nm]	Service factor f.s.	Nominal power P ₀ [kW]	Nominal torque M ₀₂ [Nm]	Available B5 motor flanges		Available B14 motor flanges			Dynamic efficiency RD	Tooth Module [mm]	 Ratios code
							-B	-C	-O	-P	-Q			
200	7	0.37	14	2.2	0.80	30	B		B-C	B-C		80	2.2	01
140	10	0.37	20	1.5	0.57	30	B		B-C	B-C		79	2.2	02
100	14	0.37	27	1.1	0.41	30	B		B-C	B-C		77	2.4	03
67	21	0.37	36	1.2	0.43	41	B		B-C	B-C		67	1.6	04
50	28	0.25	31	1.3	0.33	41	B		B-C	B-C		65	2.5	05
38	37	0.25	40	1.0	0.26	41	B		B-C	B-C		63	1.8	06
30	46	0.25	46	0.9	0.22	41	B		B-C	B-C		59	1.5	07
23	60	0.18	41	1.0	0.18	41	B		B-C	B-C		56	1.2	08
20	70	0.12	31	1.0	0.12	30	B		B-C	B-C		54	1.0	09
13.7	102	0.09	31	1.0	0.09	29	B		B-C	B-C		49	0.72	10

 Motor Flanges Available / Flange Motore Disponibili
 Supplied with Reduction Bushing / Fornito con Bussola di Riduzione
 Available on Request without reduction bushing / Disponibile a Richiesta senza Bussola di Riduzione
 Motor Flange Holes Position / Posizione Fori Flangia Motore

* Power higher than the maximum one which can be supported by the gearbox. Select according to the torque M_{av}
 Potenza superiore a quella massima sopportabile dal riduttore. Selezionare in base al momento torcente M_{av}

2

EN Unit Q45 is supplied with synthetic oil, providing "long life" lubrication. For mounting position V5-V6 please contact us. See table 1 for lubrication and recommended quantity. In table 2 please see possible radial loads and axial loads on the gearbox.

I Il riduttore tipo Q45 viene fornito lubrificato a vita con olio sintetico. Per posizioni V5-V6 contattare il ns. servizio tecnico. Vedi tab. 1 per oli e quantità consigliati. In tab.2 sono presenti i carichi radiali e assiali applicabili al riduttore.

D Für die Lebensdauerschmierung ist das Getriebe der Größe Q45 mit synthetischem Öl befüllt. Bei Einbaulage V5 oder V6 bitten wir um Rücksprache. In Tabelle 1 ist die Schmiermenge und das empfohlene Schmiermittel angegeben. In Tabelle 2 sind die zulässigen Radial - und Axialbelastungen des Getriebes aufgeführt.

F Le réducteur de type Q45 est fourni lubrifié à vie avec de l'huile synthétique. Concernant les positions V5, V6, contactez notre service d'assistance technique. Voir tableau 1 concernant les huiles et les quantités conseillées. Les charges radiales et axiales applicables au réducteur sont précisées dans le tableau 2.

E El reductor tamaño Q45 se suministra, lubricado de por vida con aceite sintético. Para las posiciones V5 y V6 contactar con nuestro servicio técnico. Ver tabla 1, para cantidades y aceites recomendados. En la tabla 2, se encuentran las cargas radiales y axiales admitidas por el reductor.

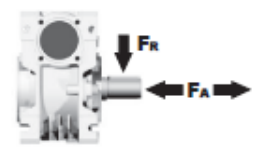
LUBRICATION Q45 Oil Quantity 0.09 Lt.

AGIP Teilm VSF 320	SHELL Omala S4 WE 320
--------------------	-----------------------

For all details on lubrication and plugs check our website tab. 1
 Per maggiori dettagli su lubrificazione e tappi olio vedi il nostro sito web

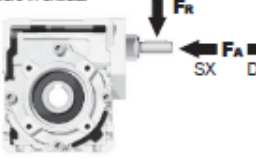
RADIAL AND AXIAL LOADS

Output shaft
Albero di uscita



n ₂ [min ⁻¹]	FA [N]	FR [N]
200	180	900
150	200	1000
100	220	1100
75	240	1200
50	260	1400
25	300	1800
15	400	2000

Input shaft
albero in entrata



n _i [min ⁻¹]	FA [N]	FR [N]
1400	42	210

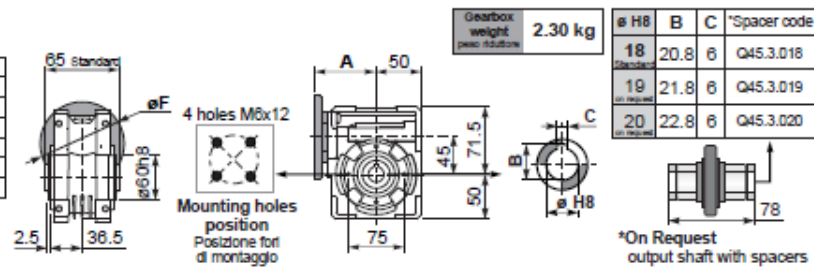
***Strong axial loads in the DX direction are not allowed.**
 Non sono consentiti forti carichi assiali con direzione DX

tab. 2

3D dimensions on the Web Square - Gear **41Nm Q45**

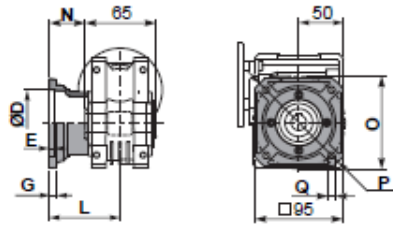
PQ45FB... Basic wormbox
Riduttore base

M. flanges	Kit code	øF	A
63B5	K050.4.041	138	80
71B5	K050.4.042	160	77.5
56B14	KC40.4.049	80	77.5
63B14	K050.4.047	90	80
71B14	K050.4.045	105	77.5



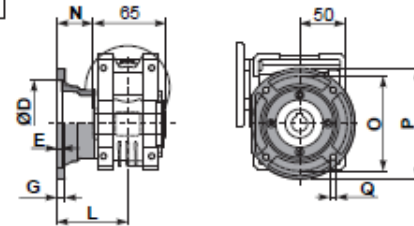
2

PQ45FC... Square flange
Flangia quadrata



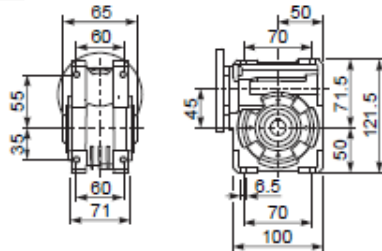
type B	øD	E	G	L	N	O	P	Q	kit code
FC	60 H8	4	7	67	34.5	75	110	9	KQ45.9.010
FL	60 H8	4	7	97	64.5	75	110	9	KQ45.9.011

PQ45F1... Round flange
Flangia rotonda

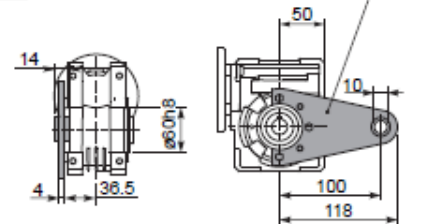


type S	øD	E	G	L	N	O	P	Q	kit code
F1	95H8	5	9	80	47.5	115	140	9.5	KSQ45.9.012
F2	80H8	5	12	58	25.5	100	120	9	KSQ45.9.013

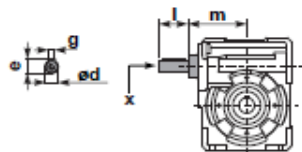
PQ45FB... Feet
Piedini



PQ45BR... Reaction arm
Braccio di reazione

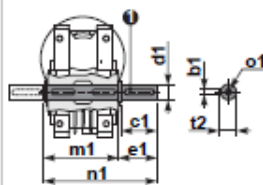


RQ45FB... Input shaft
Albero in entrata



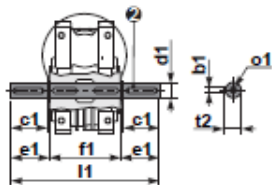
	ød	e	g	l	m	x	kit code
type B	11 h8	12.5	4	30	74	-	ⓐ K045.5.006 PAM71
type S	-	-	-	-	-	-	ⓑ -

PQ45...S... Single Shaft
Albero lento semplice



ⓐ kit cod. K045.5.028 type B
ⓑ kit cod. KS045.5.030 type S

PQ45...D... Double Shaft
Albero lento bisp.



ⓐ kit cod. K045.5.029 type B
ⓑ kit cod. KS045.5.031 type S

	b1	c1	d1	e1	f1	l1	m1	n1	t2	o1
type B	8	32	18 ^{+0.020} _{-0.010}	43	65	151	70	113	20.5	M6x18
type S	8	40	19 ^{+0.020} _{-0.010}	58.5	65	182	70	128.5	21.5	M8x20

Power screw: Thomson XCF6200

XCF16x4M

16 x 4 mm, Flange Mount, XC Advanced Anti-Backlash, XCF6200

Specs	Dimensions	Downloads	Get Quote
--------------	------------	-----------	-----------

PRODUCT	
Nut Style:	Flange Mount
Diameter x Lead:	16 x 4 mm
Product Category:	XC Advanced Anti-Backlash
Product Series:	XCF6200

PERFORMANCE	
Static Capacity (lbs):	450
Static Capacity (N):	2002
Efficiency (%):	47
Lead Accuracy (in/ft):	0.003
Lead Accuracy (µm/300mm):	76
Max Axial Backlash (in):	0
Max Axial Backlash (mm):	0
Dynamic Load (lbf):	175
Dynamic Load (kN):	0.778
Torque to Raise 1 kN (N-m):	1.35
Drag Torque (oz-in):	40215
Drag Torque (N-m):	0.56 - 0.15

MECHANICAL PROPERTIES	
Max Temperature (°F):	180
Max Temperature (°C):	82
Friction Coefficient:	0.1

SCREW	
	
Nominal Diameter or BCD (in):	0.63
Nominal Diameter or BCD (mm):	16
Lead (in):	0.157
Lead (mm):	4
Screw Root Diameter (in):	0.45
Screw Root Diameter (mm):	11.43
Max Screw Length (in):	144
Max Screw length (mm):	3657
Standard Screw Length (in):	144
Standard Screw Length (mm):	3658
Screw Material:	Stainless Steel
Standard P/N:	SRT16x4M
Screw weight (kg/m):	1.21
Number of Starts:	1

Worm gear box: Hydromec Q30 FB 30

Q30

Square - Gear
21Nm

Rating - Aluminum WORM GEARBOXES

QUICK SELECTION / Selezione veloce										input speed (n ₁) = 1400 min ⁻¹			
Output Speed n ₂ [min ⁻¹]	Ratio i	Motor power P _{in} [kW]	Output torque M _{out} [Nm]	Service factor f.s.	Nominal power P _{in} [kW]	Nominal torque M _{in} [Nm]	Available B5 motor flanges		Available B14 motor flanges		Dynamic efficiency RD	Tooth Module [mm]	Ratios code
							-A	-B	-O	-P			
280	5	0.18	5	3.3	0.60	17	B		B-C		82	1.28	01
200	7	0.18	7	2.4	0.44	17	B		B-C		80	1.44	02
140	10	0.18	10	1.8	0.32	17	B		B-C		78	1.44	03
93	15	0.18	13	1.4	0.25	19	B		B-C		73	1.44	04
70	20	0.18	17	1.1	0.20	19	B		B-C		70	1.09	05
47	30	0.12	15	1.4	0.17	21	B		B-C		62	1.44	06
35	40	0.12	19	1.1	0.13	20	B		B-C		57	1.09	07
23	61	0.09	19	1.1	0.10	20	B		B-C		50	0.72	08
17.5	80	0.09	16	1.0	0.06	16	B		B-C		48	0.56	09

A Motor Flanges Available / Flange Motore Disponibili
B Supplied with Reduction Bushing / Fornito con Bussola di Riduzione
B Available on Request without reduction bushing / Disponibile a Richiesta senza Bussola di Riduzione
C Motor Flange Hole Position / Posizione Fori Flangia Motore

2

- EN** Unit Q30 is supplied with synthetic oil, providing "long life" lubrication. For mounting position V5-V6 please contact us. See table 1 for lubrication and recommended quantity. In table 2 please see possible radial loads and axial loads on the gearbox.
- I** Il riduttore tipo Q30 viene fornito lubrificato a vita con olio sintetico. Per posizioni V5-V6 contattare il ns. servizio tecnico. Vedi tab. 1 per oli e quantità consigliati. In tab.2 sono presenti i carichi radiali e assiali applicabili al riduttore.
- D** Für die Lebensdauerschmierung ist das Getriebe der Größe Q30 mit synthetischem Öl befüllt. Bei Einbaulage V5 oder V6 bitten wir um Rücksprache. In Tabelle 1 ist die Schmiermenge und das empfohlene Schmiermittel angegeben. In Tabelle 2 sind die zulässigen Radial - und Axialbelastungen des Getriebes aufgeführt.
- F** Le réducteur de type Q30 est fourni lubrifié à vie avec de l'huile synthétique. Concernant les positions V5.V6, contactez notre service d'assistance technique. Voir tableau 1 concernant les huiles et les quantités conseillées. Les charges radiales et axiales applicables au réducteur sont précisées dans le tableau 2.
- E** El reductor tamaño Q30 se suministra, lubricado de por vida con aceite sintético. Para las posiciones V5 y V6 contactar con nuestro servicio técnico. Ver tabla 1, para cantidades y aceites recomendados. En la tabla 2, se encuentran las cargas radiales y axiales admitidas por el reductor.

LUBRICATION Q30 Oil Quantity 0.03Lt.	
AGIP Telium VSF 320	SHELL Omala S4 WE 320

For all details on lubrication and plugs check our website tab. 1
Per maggiori dettagli su lubrificazione e tappi olio vedi il nostro sito web

RADIAL AND AXIAL LOADS

Output shaft
Albero di uscita

n ₂ [min ⁻¹]	FA [N]	FR [N]
200	120	800
150	140	700
100	160	800
75	180	900
50	200	1000
25	250	1250
15	280	1400

Input shaft
albero in entrata

n ₁ [min ⁻¹]	FA [N]	FR [N]
1400	20	100

*Strong axial loads in the DX direction are not allowed.
Non sono consentiti forti carichi assiali con direzione DX

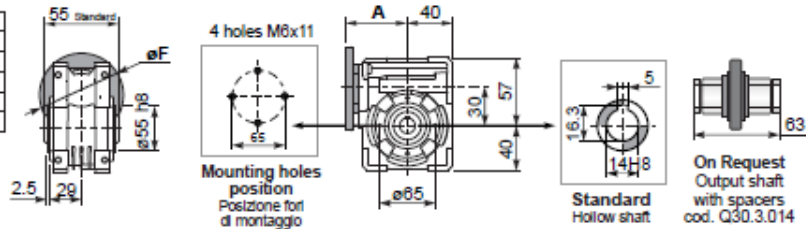
tab. 2

3D dimensions on the Web Square - Gear **21Nm Q30**

PQ30FB... Basic wormbox
Riduttore base

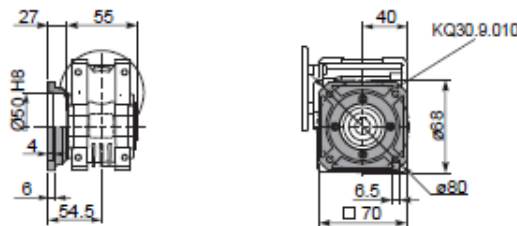
Gearbox weight
peso riduttore **1.15 kg**

M. flanges	Kit code	aF	A
56B5	K030.4.041	120	61.5
63B5	K030.4.042	140	62.5
56B14	K030.4.048	80	61.5
63B14	K030.4.045	90	62.5

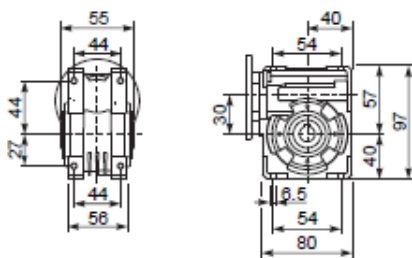


2

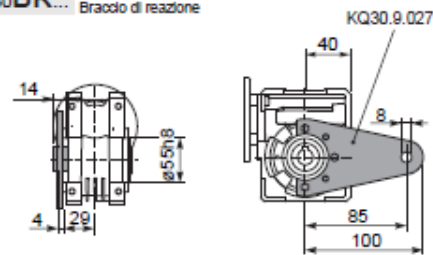
PQ30FC... Square flange
Flangia quadrata



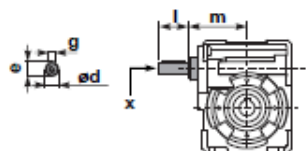
PQ30FB... Feet
Piedini



PQ30BR... Reaction arm
Braccio di reazione



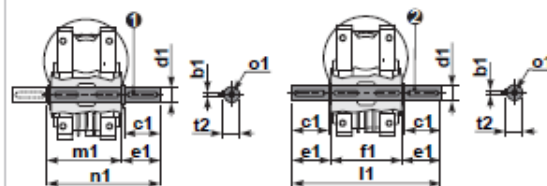
RQ30FB... Input shaft
Albero in entrata



	ød	e	g	l	m	x	kit code
type B	9 h6	10.2	3	20	58	-	K030.5.006 PAM63
type S	-	-	-	-	-	-	-

PQ30.....S Single Shaft
Albero lento semplice

PQ30.....D Double Shaft
Albero lento bisp.



ⓘ kit cod. K030.5.028 type B

Ⓜ kit cod. K030.5.029 type B

	b1	c1	d1	e1	f1	l1	m1	n1	t2	ø1
type B	5	25	14 ^{+0.020} _{-0.020}	35.5	55	128	59	94.5	18	M5x14
type S	-	-	-	-	-	-	-	-	-	-

References

- [1] E. T. Harness, N. Yozbatiran, and S. C. Cramer, “Effects of intense exercise in chronic spinal cord injury,” *Spinal Cord*, vol. 46, no. 11, pp. 733–737, Jun. 2008.
- [2] G. A. Donnan, M. Fisher, M. Macleod, and S. M. Davis, “Stroke,” *Lancet*, vol. 371, no. 9624, pp. 1612–1623, 2008.
- [3] K. W. Muir, “Stroke,” *Medicine (Baltimore)*, vol. 41, no. 3, pp. 169–174, 2013.
- [4] J. C. Furlan, B. M. Sakakibara, W. C. Miller, and A. V. Krassioukov, “Global incidence and prevalence of traumatic spinal cord injury,” *Can. J. Neurol. Sci.*, vol. 40, no. 04, pp. 456–464, 2013.
- [5] K. Stephan, S. Huber, S. Häberle, K.-G. Kanz, V. Bühren, M. van Griensven, B. Meyer, P. Biberthaler, R. Lefering, S. Huber-Wagner, and others, “Spinal cord injury--incidence, prognosis, and outcome: an analysis of the TraumaRegister DGU,” *Spine J.*, vol. 15, no. 9, pp. 1994–2001, 2015.
- [6] K. Nasir, “Heart Disease and Stroke Statistics-2015 Update: A Report From the American Heart Association,” *Circ.* 2014 131 e1-e294., 2014.
- [7] N. S. C. I. S. Center and others, “Facts and Figures at a Glance,” *Birmingham, AL Univ. Alabama Birmingham*, 2013.
- [8] I. Miyai, Y. Fujimoto, Y. Ueda, H. Yamamoto, S. Nozaki, T. Saito, and J. Kang, “Treadmill training with body weight support: Its effect on Parkinson’s disease,” *Arch. Phys. Med. Rehabil.*, vol. 81, no. 7, pp. 849–852, 2000.
- [9] M. R. Schindl, C. Forstner, H. Kern, and S. Hesse, “Treadmill training with partial body weight support in nonambulatory patients with cerebral palsy,” *Arch. Phys. Med. Rehabil.*, vol. 81, no. 3, pp. 301–306, 2000.
- [10] H. J. A. van Hedel and V. Dietz, “Rehabilitation of locomotion after spinal cord injury,” *Restor. Neurol. Neurosci.*, vol. 28, no. 1, pp. 123–134, 2010.
- [11] R. K. Bode, A. W. Heinemann, P. Semik, and T. Mallinson, “Relative importance of rehabilitation therapy characteristics on functional outcomes for persons with stroke,” *Stroke*, vol. 35, no. 11, pp. 2537–2542, 2004.
- [12] K. J. Sullivan, D. A. Brown, T. Klassen, S. Mulroy, T. Ge, S. P. Azen, C. J. Winstein, P. T. C. R. N. (PTClinResNet, and others, “Effects of task-specific locomotor and strength training in adults who were ambulatory after stroke: results of the STEPS randomized clinical trial,” *Phys. Ther.*, vol. 87, no. 12, pp. 1580–1602, 2007.

-
- [13] G. Kwakkel, R. van Peppen, R. C. Wagenaar, S. W. Dauphinee, C. Richards, A. Ashburn, K. Miller, N. Lincoln, C. Partridge, I. Wellwood, and others, “Effects of augmented exercise therapy time after stroke a meta-analysis,” *Stroke*, vol. 35, no. 11, pp. 2529–2539, 2004.
- [14] R. P. S. Van Peppen, H. J. M. Hendriks, N. L. U. Van Meeteren, P. J. M. Helders, and G. Kwakkel, “The development of a clinical practice stroke guideline for physiotherapists in The Netherlands: a systematic review of available evidence,” *Disabil. Rehabil.*, vol. 29, no. 10, pp. 767–783, 2007.
- [15] A. L. Siu, J. D. Penrod, K. S. Boockvar, K. Koval, E. Strauss, and R. S. Morrison, “Early ambulation after hip fracture: effects on function and mortality,” *Arch. Intern. Med.*, vol. 166, no. 7, pp. 766–771, 2006.
- [16] M. C. Creditor, “Hazards of hospitalization of the elderly,” *Ann. Intern. Med.*, vol. 118, no. 3, pp. 219–223, 1993.
- [17] A. Tözeren, *Human body dynamics: classical mechanics and human movement*. Springer Science & Business Media, 2000.
- [18] R. N. P. D. Elaine Nicpon Marieb, P. B. Wilhelm, and J. B. Mallatt, *Human Anatomy, Media Update, Books a la Carte Edition*. Benjamin-Cummings Publishing Company, 2011.
- [19] C. Freudenrich, G. J. Tortora, and B. H. Derrickson, *Visualizing Anatomy and Physiology*. Wiley, 2013.
- [20] M. W. Whittle, *Gait analysis: an introduction*. Butterworth-Heinemann, 2014.
- [21] V. Singh, *Textbook of Anatomy Abdomen and Lower Limb*; no. v. 2. Elsevier Health Sciences APAC, 2014.
- [22] M. F. Bear, B. W. Connors, M. Paradiso, M. F. Bear, B. W. Connors, and M. A. Neuroscience, “Exploring the brain,” *Neurosci. Williams Wilkins*, 1996.
- [23] National Stroke Association, “Explaining Stroke” Available at: <http://www.stroke.org/stroke-resources/resource-library/explaining-stroke-flash> [Accessed Mars 6, 2016].
- [24] W. H. Organization and I. S. C. Society, *International Perspectives on Spinal Cord Injury*. World Health Organization, 2013.
- [25] S. C. Kirshblum, S. P. Burns, F. Biering-Sorensen, W. Donovan, D. E. Graves, A. Jha, M. Johansen, L. Jones, A. Krassioukov, M. J. Mulcahey, M. Schmidt-Read, and W. Waring, “International standards for neurological classification of spinal cord injury (Revised 2011),” *J. Spinal Cord Med.*, vol. 34, no. 6, pp. 535–546, Nov. 2011.
-

-
- [26] A. H. Association and others, “Heart disease and stroke statistics at a glance.” 2015.
- [27] S. B. O’Sullivan, T. J. Schmitz, and G. Fulk, *Physical rehabilitation*. FA Davis, 2013.
- [28] J. Mehrholz, C. Werner, J. Kugler, and M. Pohl, “Electromechanical-assisted training for walking after stroke,” *Cochrane Database Syst Rev*, vol. 4, no. 4, 2007.
- [29] R. Greenwood, “The clinical science of neurologic rehabilitation,” *Brain*, vol. 127, no. 6, pp. 1454–1460, 2004.
- [30] C. Maria, R. Dutra, C. Maria, R. Dutra, A. Duarte, D. L. Moser, and E. F. Manffra, “Locomotor training with partial body weight support in spinal cord injury rehabilitation : literature review,” vol. 26, no. 4, pp. 907–920, 2013.
- [31] M. MacKay-Lyons, “Central pattern generation of locomotion: a review of the evidence,” *Phys. Ther.*, vol. 82, no. 1, pp. 69–83, 2002.
- [32] A. J. Threlkeld, L. D. Cooper, B. P. Monger, A. N. Craven, and H. G. Haupt, “Temporospatial and kinematic gait alterations during treadmill walking with body weight suspension,” *Gait Posture*, vol. 17, no. 3, pp. 235–245, 2003.
- [33] V. Dietz and S. J. Harkema, “Locomotor activity in spinal cord-injured persons,” *J. Appl. Physiol.*, vol. 96, no. 5, pp. 1954–1960, 2004.
- [34] S. A. Dunlop, “Activity-dependent plasticity: implications for recovery after spinal cord injury,” *Trends Neurosci.*, vol. 31, no. 8, pp. 410–418, 2008.
- [35] S. Hesse, “Treadmill training with partial body weight support after stroke: a review,” *NeuroRehabilitation*, vol. 23, no. 1, pp. 55–65, 2008.
- [36] I. Díaz, J. J. Gil, and E. Sánchez, “Lower-limb robotic rehabilitation: literature review and challenges,” *J. Robot.*, vol. 2011, 2011.
- [37] V. Dietz and T. Sinkjaer, “Spastic movement disorder: impaired reflex function and altered muscle mechanics,” *Lancet Neurol.*, vol. 6, no. 8, pp. 725–733, 2007.
- [38] I. Džidić and S. Moslavac, “Functional skills after the rehabilitation of spinal cord injury patients: observation period of 3 years.,” *Spinal Cord*, vol. 35, pp. 620–623, 1997.
- [39] B. Dobkin, H. Barbeau, D. Deforge, J. Ditunno, R. Elashoff, D. Apple, M. Basso, A. Behrman, L. Fugate, S. Harkema, and others, “The evolution of walking-related outcomes over the first 12 weeks of rehabilitation for incomplete traumatic spinal cord injury: the multicenter randomized Spinal Cord Injury Locomotor Trial,” *Neurorehabil. Neural Repair*, vol. 21, no. 1, pp. 25–35, 2007.
- [40] B. H. Dobkin, “Rehabilitation after stroke,” *N. Engl. J. Med.*, vol. 352, no. 16, pp. 1677–1684, 2005.
- [41] H. S. Jørgensen, H. Nakayama, H. O. Raaschou, and T. S. Olsen, “Recovery of walking

- function in stroke patients: the Copenhagen Stroke Study,” *Arch. Phys. Med. Rehabil.*, vol. 76, no. 1, pp. 27–32, 1995.
- [42] B. H. Dobkin, “An overview of treadmill locomotor training with partial body weight support: a neurophysiologically sound approach whose time has come for randomized clinical trials,” *Neurorehabil. Neural Repair*, vol. 13, no. 3, pp. 157–165, 1999.
- [43] C. O. Sousa, J. A. Barela, C. L. Prado-Medeiros, T. F. Salvini, and A. M. F. Barela, “The use of body weight support on ground level: an alternative strategy for gait training of individuals with stroke,” *J. Neuroeng. Rehabil.*, vol. 6, no. 1, p. 1, 2009.
- [44] H. Barbeau, M. Wainberg, and L. Finch, “Description and application of a system for locomotor rehabilitation,” *Med. Biol. Eng. Comput.*, vol. 25, no. 3, pp. 341–344, 1987.
- [45] T. G. Hornby, D. H. Zemon, and D. Campbell, “Robotic-assisted, body-weight-supported treadmill training in individuals following motor incomplete spinal cord injury,” *Phys. Ther.*, 2005.
- [46] M. Frey, G. Colombo, M. Vaglio, R. Bucher, M. Jörg, and R. Riener, “A novel mechatronic body weight support system,” *IEEE Trans. Neural Syst. Rehabil. Eng.*, vol. 14, no. 3, pp. 311–321, Sep. 2006.
- [47] C. L. Richards, F. Malouin, S. Wood-Dauphinee, J. I. Williams, J.-P. Bouchard, and D. Brunet, “Task-specific physical therapy for optimization of gait recovery in acute stroke patients,” *Arch. Phys. Med. Rehabil.*, vol. 74, no. 6, pp. 612–620, 1993.
- [48] F. Malouin, M. Potvin, J. Prévost, C. L. Richards, and S. Wood-Dauphinee, “Use of an intensive task-oriented gait training program in a series of patients with acute cerebrovascular accidents,” *Phys. Ther.*, vol. 72, no. 11, pp. 781–789, 1992.
- [49] C. M. Dean, C. L. Richards, and F. Malouin, “Task-related circuit training improves performance of locomotor tasks in chronic stroke: a randomized, controlled pilot trial,” *Arch. Phys. Med. Rehabil.*, vol. 81, no. 4, pp. 409–417, 2000.
- [50] G. V Smith, K. H. C. Silver, A. P. Goldberg, and R. F. Macko, “‘Task-oriented’ exercise improves hamstring strength and spastic reflexes in chronic stroke patients,” *Stroke*, vol. 30, no. 10, pp. 2112–2118, 1999.
- [51] V. Dietz, G. Colombo, and L. Jensen, “Locomotor activity in spinal man,” *Lancet*, vol. 344, no. 8932, pp. 1260–1263, 1994.
- [52] V. R. Edgerton, R. D. Leon, S. J. Harkema, J. A. Hodgson, N. London, D. J. Reinkensmeyer, R. R. Roy, R. J. Talmadge, N. J. Tillakaratne, W. Timoszyk, and others, “Retraining the injured spinal cord,” *J. Physiol.*, vol. 533, no. 1, pp. 15–22, 2001.
- [53] D. S. Smith, E. Goldenberg, A. Ashburn, G. Kinsella, K. Sheikh, P. J. Brennan, T. W.

- Meade, D. W. Zutshi, J. D. Perry, and J. S. Reeback, "Remedial therapy after stroke: a randomised controlled trial.," *Br Med J (Clin Res Ed)*, vol. 282, no. 6263, pp. 517–520, 1981.
- [54] M. Dam, P. Tonin, S. Casson, M. Ermani, G. Pizzolato, V. Iaia, and L. Battistin, "The effects of long-term rehabilitation therapy on poststroke hemiplegic patients.," *Stroke*, vol. 24, no. 8, pp. 1186–1191, 1993.
- [55] G. Kwakkel, R. C. Wagenaar, J. W. R. Twisk, G. J. Lankhorst, and J. C. Koetsier, "Intensity of leg and arm training after primary middle-cerebral-artery stroke: a randomised trial," *Lancet*, vol. 354, no. 9174, pp. 191–196, 1999.
- [56] M. Wirz, D. H. Zemon, R. Rupp, A. Scheel, G. Colombo, V. Dietz, and T. G. Hornby, "Effectiveness of automated locomotor training in patients with chronic incomplete spinal cord injury: a multicenter trial," *Arch. Phys. Med. Rehabil.*, vol. 86, no. 4, pp. 672–680, 2005.
- [57] J. A. Galvez and D. J. Reinkensmeyer, "Robotics for Gait Training After Spinal Cord Injury," vol. 11, no. 2, pp. 18–33, 2005.
- [58] J. Liang, A. Hernandez, O. Ma, B. Qiao, and R. Paz, "Nonhuman test of a new active body support system for improving locomotion training," in *Advanced Intelligent Mechatronics, 2009. AIM 2009. IEEE/ASME International Conference on*, 2009, pp. 1312–1317.
- [59] M. Glauser, Z. Lin, and P. E. Allaire, "Modeling and control of a partial body weight support system: an output regulation approach," *Control Syst. Technol. IEEE Trans.*, vol. 18, no. 2, pp. 480–490, 2010.
- [60] K. E. Gordon, D. P. Ferris, M. Robertson, J. A. Beres, and S. J. Harkema, "The importance of using an appropriate body weight support system in locomotor training," in *Soc Neurosci*, 2000, vol. 26, no. 1, p. 160.
- [61] F. Gazzani, A. Fadda, M. Torre, and V. Macellari, "WARD: a pneumatic system for body weight relief in gait rehabilitation," *Rehabil. Eng. IEEE Trans.*, vol. 8, no. 4, pp. 506–513, 2000.
- [62] T. Watanabe, E. Ohki, T. Ando, and M. G. Fujie, "Fundamental study of force control method for pelvis-supporting body weight support system," in *Robotics and Biomimetics, 2008. ROBIO 2008. IEEE International Conference on*, 2009, pp. 1403–1408.
- [63] G. Chen, D. Schwandt, H. F. M. der Loos, J. Anderson, D. P. Ferris, F. E. Zajac, S. A. Kautz, C. G. Burgar, C. Patten, R. R. Neptune, and others, "Compliance-adjustable,

- force-sensing harness support for studying treadmill training in neurologically impaired subjects,” in *Proceedings of the 6th Annual Gait and Clinical Movement Analysis Meeting*, 2001, pp. 25–28.
- [64] S. Hussain, S. Q. Xie, and G. Liu, “Robot assisted treadmill training: mechanisms and training strategies,” *Med. Eng. Phys.*, vol. 33, no. 5, pp. 527–533, 2011.
- [65] E. H. F. van Asseldonk and H. van der Kooij, “Robot-Aided Gait Training with LOPES,” in *Neurorehabilitation Technology*, Springer, 2012, pp. 379–396.
- [66] R. Riener, L. Lünenburger, S. Jezernik, M. Anderschitz, G. Colombo, and V. Dietz, “Patient-cooperative strategies for robot-aided treadmill training: first experimental results,” *Neural Syst. Rehabil. Eng. IEEE Trans.*, vol. 13, no. 3, pp. 380–394, 2005.
- [67] J. F. Veneman, R. Kruidhof, E. E. G. Hekman, R. Ekkelenkamp, E. H. F. Van Asseldonk, and H. Van Der Kooij, “Design and evaluation of the LOPES exoskeleton robot for interactive gait rehabilitation,” *IEEE Trans. Neural Syst. Rehabil. Eng.*, vol. 15, no. 1, pp. 379–386, 2007.
- [68] E. T. Wolbrecht, V. Chan, D. J. Reinkensmeyer, and J. E. Bobrow, “Optimizing compliant, model-based robotic assistance to promote neurorehabilitation,” *Neural Syst. Rehabil. Eng. IEEE Trans.*, vol. 16, no. 3, pp. 286–297, 2008.
- [69] J. L. Emken, J. H. Wynne, S. J. Harkema, and D. J. Reinkensmeyer, “Robotic device for manipulating human stepping,” *IEEE Trans. Robot.*, vol. 22, no. 1, 2006.
- [70] S. K. Banala, S. K. Agrawal, and J. P. Scholz, “Active Leg Exoskeleton (ALEX) for gait rehabilitation of motor-impaired patients,” in *Rehabilitation Robotics, 2007. ICORR 2007. IEEE 10th International Conference on*, 2007, pp. 401–407.
- [71] D. Aoyagi, W. E. Ichinose, S. J. Harkema, D. J. Reinkensmeyer, and J. E. Bobrow, “A Robot and Control Algorithm That Can Synchronously Assist in Naturalistic Motion During Body-Weight-Supported Gait Training Following Neurologic Injury,” vol. 15, no. 3, pp. 387–400, 2007.
- [72] G. Colombo, M. Joerg, R. Schreier, and V. Dietz, “Treadmill training of paraplegic patients using a robotic orthosis,” *J. Rehabil. Res. Dev.*, vol. 37, no. December, pp. 693–700, 2000.
- [73] S. Freivogel, J. Mehrholz, T. Husak-Sotomayor, and D. Schmalohr, “Gait training with the newly developed ‘LokoHelp’-system is feasible for non-ambulatory patients after stroke, spinal cord and brain injury. A feasibility study,” *Brain Inj.*, vol. 22, no. 7–8, pp. 625–632, 2008.
- [74] R. G. West, “Powered gait orthosis and method of utilizing same,” U.S. Patent No.

- 6,689,075, 2004.
- [75] S. Hesse and D. Uhlenbrock, "A mechanized gait trainer for restoration of gait.," *J. Rehabil. Res. Dev.*, vol. 37, no. 6, pp. 701–708, 2000.
- [76] H. Schmidt, "HapticWalker-A novel haptic device for walking simulation," in *Proc. of EuroHaptics*, 2004, pp. 60–67.
- [77] S. Hesse, A. Waldner, and C. Tomelleri, "Innovative gait robot for the repetitive practice of floor walking and stair climbing up and down in stroke patients.," *J. Neuroeng. Rehabil.*, vol. 7, p. 30, 2010.
- [78] C. D. M. Simons, E. H. F. van Asseldonk, J. I. Folkersma, J. van den Hoek, M. Postma, and J. H. Buurke, "First clinical results with the new innovative robotic gait trainer LOPES," *Gait posture*, vol. 2, no. 30, 2009.
- [79] S. K. Banala, S. K. Agrawal, A. Fattah, V. Krishnamoorthy, W.-L. Hsu, J. Scholz, and K. Rudolph, "Gravity-balancing leg orthosis and its performance evaluation," *Robot. IEEE Trans.*, vol. 22, no. 6, pp. 1228–1239, 2006.
- [80] S. K. Agrawal, S. K. Banala, A. Fattah, V. Sangwan, V. Krishnamoorthy, J. P. Scholz, and W.-L. Hsu, "Assessment of motion of a swing leg and gait rehabilitation with a gravity balancing exoskeleton," *Neural Syst. Rehabil. Eng. IEEE Trans.*, vol. 15, no. 3, pp. 410–420, 2007.
- [81] B. Armstrong-Hélouvry, P. Dupont, and C. C. De Wit, "A survey of models, analysis tools and compensation methods for the control of machines with friction," *Automatica*, vol. 30, no. 7, pp. 1083–1138, 1994.
- [82] S. K. Banala, S. H. Kim, S. K. Agrawal, and J. P. Scholz, "Robot assisted gait training with active leg exoskeleton (ALEX)," *Neural Syst. Rehabil. Eng. IEEE Trans.*, vol. 17, no. 1, pp. 2–8, 2009.
- [83] J. L. Emken, S. J. Harkema, J. A. Beres-Jones, C. K. Ferreira, and D. J. Reinkensmeyer, "Feasibility of manual teach-and-replay and continuous impedance shaping for robotic locomotor training following spinal cord injury," *Biomed. Eng. IEEE Trans.*, vol. 55, no. 1, pp. 322–334, 2008.
- [84] Hocoma AG, "Lokomat - Hocoma." Available at: <https://www.hocoma.com/world/en/products/lokomat/> [Accessed March 6, 2016].
- [85] Motorika LTd, "ReoAmbulator." Available at: <http://www.motorika.com/?categoryId=91261> [Accessed March 6, 2016].
- [86] S. Jezernik, G. Colombo, and M. Morari, "Automatic gait-pattern adaptation algorithms for rehabilitation with a 4-DOF robotic orthosis," *Robot. Autom. IEEE Trans.*, vol. 20,

- no. 3, pp. 574–582, 2004.
- [87] R. Riener, “Technology of the robotic gait orthosis Lokomat,” in *Neurorehabilitation Technology*, Springer London, 2012, pp. 221–232.
- [88] S. Freivogel, D. Schmalohr, and J. Mehrholz, “Improved walking ability and reduced therapeutic stress with an electromechanical gait device,” *J. Rehabil. Med.*, vol. 41, no. 9, pp. 734–739, 2009.
- [89] S. Fisher, L. Lucas, and T. Adam Thrasher, “Robot-assisted gait training for patients with hemiparesis due to stroke,” *Top. Stroke Rehabil.*, vol. 18, no. 3, pp. 269–276, 2011.
- [90] H. Schmidt, C. Werner, R. Bernhardt, S. Hesse, and J. Krüger, “Gait rehabilitation machines based on programmable footplates,” *J. Neuroeng. Rehabil.*, vol. 4, no. 1, p. 1, 2007.
- [91] M. Pohl, C. Werner, M. Holzgraefe, G. Kroczeck, I. Wingendorf, G. Hoölig, R. Koch, and S. Hesse, “Repetitive locomotor training and physiotherapy improve walking and basic activities of daily living after stroke: a single-blind, randomized multicentre trial (DEutsche GAngrainerStudie, DEGAS),” *Clin. Rehabil.*, vol. 21, no. 1, pp. 17–27, 2007.
- [92] C. Werner, S. Von Frankenberg, T. Treig, M. Konrad, and S. Hesse, “Treadmill training with partial body weight support and an electromechanical gait trainer for restoration of gait in subacute stroke patients a randomized crossover study,” *Stroke*, vol. 33, no. 12, pp. 2895–2901, 2002.
- [93] S. H. Peurala, O. Airaksinen, P. Huuskonen, P. Jäkälä, M. Juhakoski, K. Sandell, I. M. Tarkka, and J. Sivenius, “Effects of intensive therapy using gait trainer or floor walking exercises early after stroke,” *J. Rehabil. Med.*, vol. 41, no. 3, pp. 166–173, 2009.
- [94] I. C. Maier, E. B. de Haller, S. M. Beer, I. Borggraefe, K. Campen, A. R. Luft, D. Manoglou, A. Meyer-Heim, T. Schuler, and M. Wirz, “Transfer of technology into clinical application,” in *Neurorehabilitation Technology*, Springer, 2012, pp. 303–323.
- [95] S. Hesse and C. Werner, “Connecting research to the needs of patients and clinicians,” *Brain Res. Bull.*, vol. 78, no. 1, pp. 26–34, 2009.
- [96] C. Tomelleri, A. Waldner, C. Werner, and S. Hesse, “Adaptive locomotor training on an end-effector gait robot: evaluation of the ground reaction forces in different training conditions,” in *Rehabilitation Robotics (ICORR), 2011 IEEE International Conference on*, 2011, pp. 1–5.
- [97] R. Riener, L. Lünenburger, and G. Colombo, “Human-centered robotics applied to gait training and assessment,” *J. Rehabil. Res. Dev.*, vol. 43, no. 5, p. 679, 2006.
- [98] A. Morbi, “Design, Control, and Implementation of a Robotic Gait Rehabilitation

- System for Overground Gait Training,” 2014.
- [99] M. Wu and J. M. Landry, “Lower Extremity Flexible Assist Devices for Locomotion,” in *Neurorehabilitation Technology*, Springer, 2012, pp. 361–378.
- [100] D. Surdilovic and J. Zhang, “STRING-MAN: Wire-robot technology for safe, flexible and human-friendly gait rehabilitation,” in *Rehabilitation Robotics, 2007. ICORR 2007. IEEE 10th International Conference on*, 2007, pp. 446–453.
- [101] A. Alamdari and V. Krovi, “Robotic physical exercise and system (ROPES): A cable-driven robotic rehabilitation system for lower-extremity motor therapy,” in *ASME 2015 International Design Engineering Technical Conferences and Computers and Information in Engineering Conference*, 2015, pp. V05AT08A032–V05AT08A032.
- [102] D. Surdilovic and R. Bernhardt, “STRING-MAN: a new wire robot for gait rehabilitation,” in *Robotics and Automation, 2004. Proceedings. ICRA’04. 2004 IEEE International Conference on*, 2004, vol. 2, pp. 2031–2036.
- [103] M. Wu, T. G. Hornby, J. M. Landry, H. Roth, and B. D. Schmit, “A cable-driven locomotor training system for restoration of gait in human SCI,” *Gait Posture*, vol. 33, no. 2, pp. 256–260, 2011.
- [104] G. Colombo and R. Bucher, “Device for adjusting the prestress of an elastic means around a predetermined tension or position,” U.S. Patent No. 8,192,331, 2012.
- [105] R. Verhoeven, “Analysis of the Workspace of Tendon-based Stewart Platforms,” Ph.D. dissertation, Dept. Mech. Eng., Duisburg-Essen Univ., Duisburg, 2004.
- [106] C. L. Vaughan, B. L. Davis, L. Christopher, and J. C. O. Connor, *Dynamics of Human Gait*. Kiboho Publishers, 1999.
- [107] J. Hamill and K. M. Knutzen, *Biomechanical basis of human movement*. Lippincott Williams & Wilkins, 2006.
- [108] R. Baker, “Gait analysis methods in rehabilitation,” *J. Neuroeng. Rehabil.*, vol. 3, p. 10, Jan. 2006.
- [109] R. Bartlett, *Introduction to sports biomechanics Analysing human movement patterns*. Routledge, 2007.
- [110] A. L. Bell, R. A. Brand, and D. R. Pedersen, “Prediction of hip joint centre location from external landmarks,” *Hum. Mov. Sci.*, vol. 8, no. 1, pp. 3–16, 1989.
- [111] A. L. BELL, “A COMPARISON OF THE ACCURACY OF SEVERAL HIP CENTER LOCATION PREDICTION METHODS,” vol. 23, no. 6, pp. 6–8, 1990.
- [112] R. M. Ehrig, W. R. Taylor, G. N. Duda, and M. O. Heller, “A survey of formal methods for determining the centre of rotation of ball joints,” *J. Biomech.*, vol. 39, no. 15, pp.

- 2798–2809, 2006.
- [113] S. J. Piazza, N. Okita, and P. R. Cavanagh, “Accuracy of the functional method of hip joint center location: Effects of limited motion and varied implementation,” *J. Biomech.*, vol. 34, pp. 967–973, 2001.
- [114] S. Upadhyaya and W.-S. Lee, “Survey of Formal Methods of Hip Joint Center Calculation in Human Studies,” *APCBEE Procedia*, vol. 7, pp. 27–31, 2013.
- [115] H. Kainz, C. P. Carty, L. Modenese, R. N. Boyd, and D. G. Lloyd, “Estimation of the hip joint centre in human motion analysis: A systematic review,” *Clin. Biomech.*, vol. 30, no. 4, pp. 319–329, 2015.
- [116] M. Sangeux, H. Pillet, and W. Skalli, “Which method of hip joint centre localisation should be used in gait analysis?,” *Gait Posture*, vol. 40, no. 1, pp. 20–25, 2014.
- [117] V. Camomilla, A. Cereatti, G. Vannozzi, and A. Cappozzo, “An optimized protocol for hip joint centre determination using the functional method.,” *J. Biomech.*, vol. 39, no. 6, pp. 1096–106, Jan. 2006.
- [118] G. Wu, S. Siegler, P. Allard, C. Kirtley, A. Leardini, D. Rosenbaum, M. Whittle, D. D. D’Lima, L. Cristofolini, and H. Witte, “ISB recommendation on definitions of joint coordinate system of various joints for the reporting of human joint motion—part I: ankle, hip, and spine,” *J. Biomech.*, vol. 35, no. 4, pp. 543–548, 2002.
- [119] J. L. Hicks and J. G. Richards, “Clinical applicability of using spherical fitting to find hip joint centers.,” *Gait Posture*, vol. 22, no. 2, pp. 138–45, Oct. 2005.
- [120] L. Boutin, A. Eon, S. Zeghloul, and P. Lacouture, “An auto-adaptable algorithm to generate human-like locomotion for different humanoid robots based on motion capture data,” in *Intelligent Robots and Systems (IROS), 2010 IEEE/RSJ International Conference on*, 2010, pp. 1256–1261.
- [121] T. Li, M. Ceccarelli, T. Essomba, M. A. Laribi, and S. Zeghloul, “Analysis of human biped obstacle overcoming by motion capture system,” *Robot. Alpe--Adria--Danube Reg. 2012 (RAAD 2012), Int. Work.*, pp. 85–92, 2012.
- [122] J. Majernik and S. Republic, “Normative Human Gait Databases,” vol. 2, no. 3, pp. 69–74, 2013.
- [123] A. L. Hof, “Scaling gait data to body size,” *Gait Posture*, vol. 3, no. 4, pp. 222–223, 1996.
- [124] B. W. Stansfield, S. J. Hillman, M. E. Hazlewood, and J. E. Robb, “Regression analysis of gait parameters with speed in normal children walking at self-selected speeds,” *Gait Posture*, vol. 23, no. 3, pp. 288–294, 2006.

- [125] F. E. Zajac, R. R. Neptune, and S. A. Kautz, “Biomechanics and muscle coordination of human walking: Part I: Introduction to concepts, power transfer, dynamics and simulations,” *Gait Posture*, vol. 16, no. 3, pp. 215–232, 2002.
- [126] J. Hidler, W. Wisman, and N. Neckel, “Kinematic trajectories while walking within the Lokomat robotic gait-orthosis,” *Clin. Biomech.*, vol. 23, no. 10, pp. 1251–1259, Dec. 2008.
- [127] D. A. Winter, *Biomechanics and Motor Control of Human Movement*. John Wiley & Sons, 2009.
- [128] V. Racic, A. Pavic, and J. M. W. Brownjohn, “Experimental identification and analytical modelling of human walking forces: Literature review,” *J. Sound Vib.*, vol. 326, no. 1, pp. 1–49, 2009.
- [129] J. J. Craig, *Introduction to robotics Mechanics and Control*, Third Edit. Upper Saddle River: Pearson Education International, 2005.
- [130] S. Kawamura, H. Kino, and C. Won, “High-speed manipulation by using parallel wire-driven robots,” *Robotica*, vol. 18, no. 1, pp. 13–21, Jan. 2000.
- [131] J. dit Sandretto, “Étalonnage des robots à câbles, identification et qualification,” Diss. PhD thesis, Université de Nice-Sophia Antipolis, 2013.
- [132] X. Tang, “An Overview of the Development for Cable-Driven Parallel Manipulator,” *Adv. Mech. Eng.*, vol. 2014, pp. 1–9, 2014.
- [133] “CableBOT- Parallel Cable Robotics for Improving Maintenance and Logistics of Large-Scale Products.” Available at: <http://www.cablebot.eu/en/> [Accessed March 6, 2016] .
- [134] SKYCAM LCC, “SkyCam.” Available at: skycam.tv [Accessed March 6, 2016].
- [135] I. Ebert-Uphoff and P. A. Voglewede, “On the connections between cable-driven robots, parallel manipulators and grasping,” in *IEEE International Conference on Robotics and Automation, 2004. Proceedings. ICRA '04. 2004*, 2004, no. c, pp. 4521–4526 Vol.5.
- [136] A. Riechel and I. Ebert-Uphoff, “Force-feasible workspace analysis for underconstrained, point-mass cable robots,” in *IEEE International Conference on Robotics and Automation, 2004. Proceedings. ICRA '04. 2004*, 2004, pp. 4956–4962 Vol.5.
- [137] S. Krut, O. Company, and F. Pierrot, “Force performance indexes for parallel mechanisms with actuation redundancy, especially for parallel wire-driven manipulators,” *Intell. Robot. Syst., 2004.(IROS 2004). Proceedings. 2004 IEEE/RSJ International Conference on. Vol. 4. IEEE, 2004*.
- [138] P. Bosscher, A. T. Riechel, and I. Ebert-Uphoff, “Wrench-feasible workspace generation

- for cable-driven robots,” *IEEE Trans. Robot.*, vol. 22, no. 5, pp. 890–902, Oct. 2006.
- [139] E. Stump and V. Kumar, “Workspaces of Cable-Actuated Parallel Manipulators,” *J. Mech. Des.*, vol. 128, no. 1, p. 159, 2006.
- [140] S. Bouchard, C. Gosselin, and B. Moore, “On the Ability of a Cable-Driven Robot to Generate a Prescribed Set of Wrenches,” *J. Mech. Robot.*, vol. 2, no. 1, p. 011010, 2010.
- [141] X. Diao and O. Ma, “Workspace Determination of General 6-d.o.f. Cable Manipulators,” *Adv. Robot.*, vol. 22, no. June 2013, pp. 37–41.
- [142] C. B. Pham, S. H. Yeo, G. Yang, and I.-M. Chen, “Workspace analysis of fully restrained cable-driven manipulators,” *Rob. Auton. Syst.*, vol. 57, no. 9, pp. 901–912, 2009.
- [143] W. Bin Lim, G. Yang, S. H. Yeo, and S. K. Mustafa, “A generic force-closure analysis algorithm for cable-driven parallel manipulators,” *Mech. Mach. Theory*, vol. 46, no. 9, pp. 1265–1275, Sep. 2011.
- [144] M. Gouttefarde, D. Daney, and J.-P. Merlet, “Interval-Analysis-Based Determination of the Wrench-Feasible Workspace of Parallel Cable-Driven Robots,” *IEEE Trans. Robot.*, vol. 27, no. 1, pp. 1–13, Feb. 2011.
- [145] J. Pusey, A. Fattah, S. Agrawal, and E. Messina, “Design and workspace analysis of a 6–6 cable-suspended parallel robot,” *Mech. Mach. Theory*, vol. 39, no. 7, pp. 761–778, Jul. 2004.
- [146] A. Fattah and S. K. Agrawal, “On the Design of Cable-Suspended Planar Parallel Robots,” *J. Mech. Des.*, vol. 127, no. 5, p. 1021, 2005.
- [147] L. Xu, J. Chen, and S. Jiang, “Design and workspace optimization of a 6/6 cable-suspended parallel robot,” in *2010 International Conference on Computer Application and System Modeling (ICCASM 2010)*, 2010, no. Iccasm, pp. V10–610–V10–614.
- [148] M. Hiller, S. Fang, S. Mielczarek, R. Verhoeven, and D. Franitza, “Design, analysis and realization of tendon-based parallel manipulators,” *Mech. Mach. Theory*, vol. 40, no. 4, pp. 429–445, Apr. 2005.
- [149] A. Alikhani, S. Behzadipour, A. Alasty, and S. A. Sadough Vanini, “Design of a large-scale cable-driven robot with translational motion,” *Robot. Comput. Integr. Manuf.*, vol. 27, no. 2, pp. 357–366, Apr. 2011.
- [150] J. Du, H. Bao, and C. Cui, “Stiffness and dexterous performances optimization of large workspace cable-driven parallel manipulators,” *Adv. Robot.*, vol. 28, no. 3, pp. 187–196, Feb. 2014.
- [151] C. Leclerc and C. Gosselin, “MULTIOBJECTIVE GENETIC ALGORITHM FOR OPTIMIZING CABLE-DRIVEN MECHANISMS-A FLIGHT SIMULATOR

- APPLICATION,” *Trans. Can. Soc. Mech. Eng.*, vol. 33, no. 4, pp. 633–644, 2009.
- [152] T. Bruckmann, L. Mikelsons, and M. Hiller, “A Design-To-Task Approach for Wire Robots,” in *Interdisciplinary Applications of Kinematics*, A. Kecskeméthy, V. Potkonjak, and A. Müller, Eds. Dordrecht: Springer Netherlands, 2012, pp. 83–97.
- [153] B. Ouyang and W. Shang, “Wrench-feasible workspace based optimization of the fixed and moving platforms for cable-driven parallel manipulators,” *Robot. Comput. Integr. Manuf.*, vol. 30, no. 6, pp. 629–635, Dec. 2014.
- [154] M. a. Laribi, L. Romdhane, and S. Zeghloul, “Analysis and dimensional synthesis of the DELTA robot for a prescribed workspace,” *Mech. Mach. Theory*, vol. 42, no. 7, pp. 859–870, Jul. 2007.
- [155] F. Hao and J.-P. Merlet, “Multi-criteria optimal design of parallel manipulators based on interval analysis,” *Mech. Mach. Theory*, vol. 40, no. 2, pp. 157–171, Feb. 2005.
- [156] R. L. Williams and P. Gallina, “Planar cable-direct-driven robots: design for wrench exertion,” *J. Intell. Robot. Syst.*, vol. 35, no. 2, pp. 203–219, 2002.
- [157] Q. J. Duan and X. Duan, “Workspace Classification and Quantification Calculations of Cable-Driven Parallel Robots,” *Adv. Mech. Eng.*, vol. 2014, pp. 1–9, 2014.
- [158] M. M. Aref and H. D. Taghirad, “Geometrical workspace analysis of a cable-driven redundant parallel manipulator: KNTU CDRPM,” in *Intelligent Robots and Systems, 2008. IROS 2008. IEEE/RSJ International Conference on*, 2008, pp. 1958–1963.
- [159] L. W. Wang, B. Y. Liu, and J. W. Han, “Survey of Box-Based Algorithms for Collision Detection,” *J. Civ. Aviat. Univ. China*, vol. 25, no. 4, 2007.
- [160] J.-P. Merlet, “Interval analysis and reliability in robotics,” *Int. J. Reliab. Saf.*, vol. 3, no. 1–3, pp. 104–130, 2009.
- [161] E. Loh and G. W. Walster, “Rump’s example revisited,” *Reliab. Comput.*, vol. 8, no. 3, pp. 245–248, 2002.
- [162] S. M. Rump, *Algorithms for verified inclusions: theory and practice*. 1988.
- [163] E. Hansen and G. W. Walster, *Global optimization using interval analysis: revised and expanded*, vol. 264. CRC Press, 2003.
- [164] L. Jaulin, *Applied interval analysis: with examples in parameter and state estimation, robust control and robotics*, vol. 1. Springer Science & Business Media, 2001.
- [165] R. E. Moore, F. Bierbaum, and K.-P. Schwietz, *Methods and applications of interval analysis*, vol. 2. SIAM, 1979.
- [166] M. Fiedler, J. Nedoma, J. Ramik, J. Rohn, and K. Zimmermann, *Linear Optimization Problems with Inexact Data*. Boston: Springer US, 2006.

- [167] R. H. Byrd, M. E. Hribar, and J. Nocedal, “An Interior Point Algorithm for Large-Scale Nonlinear Programming,” *SIAM J. Optim.*, vol. 9, no. 4, pp. 877–900, 1999.
- [168] S. Rump, “INTLAB — INTerval LABoratory,” in *Developments in Reliable Computing SE - 7*, T. Csendes, Ed. Springer Netherlands, 1999, pp. 77–104.
- [169] Igus, “igus® Drive module.” Available at: http://www.igus.eu/wpck/8945/drive_unit_Drive_module [Accessed March 6, 2016].
- [170] A. Taherifar, M. R. Hadian, M. Mousavi, A. Rassaf, and F. Ghiasi, “LOKOIRAN - A novel robot for rehabilitation of spinal cord injury and stroke patients,” in *International Conference on Robotics and Mechatronics, ICRoM 2013*, 2013, pp. 218–223.
- [171] V. Camomilla, T. Bonci, R. Dumas, L. Chèze, and A. Cappozzo, “A model of the soft tissue artefact rigid component,” *J. Biomech.*, vol. 48, no. 10, pp. 1752–1759, 2015.

List of Figures

Figure 1: Planes of the human body [20].	11
Figure 2: Types of angular movements [18][19].	12
Figure 3: Anatomy of the lower limb [18].	13
Figure 4: A typical synovial joint (the knee joint) [19].	13
Figure 5: Main divisions of the nervous system [22].	15
Figure 6: The brain and its main parts [19].	16
Figure 7: Main functions of the different areas of the brain [23].	16
Figure 8: The spinal cord [24].	17
Figure 9: Illustration of stroke causes [23]: a) Ischemic stroke, and b) Hemorrhagic stroke.	18
Figure 10: Therapist-assisted training [27]: (a) Overground BWS training, and (b) BWSTT.	21
Figure 11: (a) The new LOPES system [65], (b) The Alex prototype [70], and (c) Diagram of the ARTHuR gait trainer [69].	24
Figure 12: (a) Experimental setup of the PAM/POGO [71], (b) Lokomat system (picture courtesy of Hocoma AG [84]), and (c) ReoAmbulator (picture courtesy of Motorika Ltd. [85]).	25
Figure 13: (a) the Electromechanical Gait Trainer [90], (b) The HapticWalker walking simulator [90], and (c) the gait robot G-EO [94].	27
Figure 14: (a) Experimental setup of the STRIN-MAN system [100], and (b) Concept of the SMART-STRING system [100].	29
Figure 15: Description of the CaLT gait trainer [103].	30
Figure 16: Mechanical description of the proposed gait training machine.	31
Figure 17: Common body weight support systems [46]: (a) Static BWS: a simple winch, (b) Passive dynamic BWS with adjustable counterweight, (c) Passive dynamic BWS with elastic spring, and (d) Active dynamic BWS with force-control loop.	32
Figure 18: prototype of the leg's orthosis.	33
Figure 19: Walk events of the right limb (in gray) during a gait cycle [20].	36
Figure 20: Timing of single and double support periods [20].	37
Figure 21: Right leg (in gray) at [20]: (a) Initial contact, and (b) Opposite toe off.	37
Figure 22: Right leg (in gray) at [20]: (a) Heel rise, (b) Opposite initial contact, and (c) Toe off.	38
Figure 23: Right leg (in gray) at [20]: (a) Feet adjacent, and (b) Tibia vertical.	39
Figure 24: Distance parameters of the gait cycle with reference to feet footprints [106].	39
Figure 25: Basic Vicon MX configuration.	41
Figure 26: The experimental setup.	41
Figure 27: Calibration wand of the Vicon system.	41
Figure 28: Marker placement model.	42
Figure 29: Identification of the right Hip Joint Center using geometric sphere fitting.	44
Figure 30: Angle definitions for the lower limb.	45
Figure 31: Angular trajectories of the lower limb in function of time.	46
Figure 32: Angular trajectories of the lower limb against percentage of one gait cycle.	46
Figure 33: Vertical displacement of the pelvis against percentage of one gait cycle.	46
Figure 34: Ground reaction of both feet in function of time.	47
Figure 35: Normalized ground reaction during a gait cycle.	48
Figure 36: Human body 4 segment kinematic model for treadmill walking.	51
Figure 37: External loads acting on the lower limb and kinematic specifications.	51
Figure 38: Body segment lengths expressed as portion of the body height [127].	52
Figure 39: Free-body diagrams of body segments	53

Figure 40: Curve of α coefficient.	54
Figure 41: Simplified SimMechanics model.....	57
Figure 42: Unloading force F_{un} during the on-ground walking.	59
Figure 43: Upper body force F_{ub} during the on-ground walking.	59
Figure 44: Ground reaction force R_{gr} during the on-ground walking.	60
Figure 45: Foot force F_{ft} during the on-ground walking.	60
Figure 46: Thigh force F_{th} during the on-ground walking.	60
Figure 47: Footlifter force F_{lr} during the on-ground walking.	60
Figure 48: Variation of the actuation wrench (F_{cdr}, M_{cdr}) during the on-ground walking.	61
Figure 49: Variation of the actuation wrench (F_{cdr}, M_{cdr}) during the off-ground walking.....	62
Figure 50: Example of a CDPM: 7 cables Falcon Robot [130].	65
Figure 51: actuation system of cables [131].....	65
Figure 52: Applications for CDPMs: (a) Maintenance: CABLEBOT [133], and (b) Video recording: Skycam [134].	66
Figure 53: Kinematic diagram of a CDPM.	68
Figure 54: Cable/cable collision detection.	69
Figure 55: Cable/end-effector collision detection.	70
Figure 56: Cable/workpiece interference.	70
Figure 57: Complex shape of the exact solution of the interval linear system [163].....	75
Figure 58: A 3-DOF planar robot and its desired workspace $[q]$	76
Figure 59: Computation algorithm of feasible set of boxes for a specific workspace.	81
Figure 60: Example of a 3-DOF planar robot.	82
Figure 61: Example of a 6-DOF spatial robot.....	84
Figure 62: Bisection of the desired workspace: (a) Into 66 boxes, and (b) Into 264 boxes....	86
Figure 63: Geometrical specifications of the CDLM.....	91
Figure 64: Algorithm of workspace and external wrench evaluation.	92
Figure 65: the required translational workspace P evaluated as a set of boxes.....	93
Figure 66: Cable/end-effector collision detection.....	94
Figure 67: Algorithm of generation of feasible and collision-free configurations.....	94
Figure 68: Design parameters of the CDLM: $A_{1y}, A_{2y}, A_{3y}, A_{4y}, A_{1x}/A_{4x}$ and A_{2x}/A_{3x}	95
Figure 69: Algorithm of generation of the optimal design.....	96
Figure 70: Curves of cable tensions: (a) On-ground walking, and (b) Off-ground walking....	96
Figure 71: determination of maximum tension for Cable 4.....	97
Figure 72: Maximum cable tensions for: (a) The optimal configuration, and (b) A non-optimal configuration.....	98
Figure 73: Maximum linear velocity of the cables.....	98
Figure 74: Simulated cables power.....	99
Figure 75: Length variation curves of cables for the optimal design.....	99
Figure 76: Cable drive unit [169].....	100
Figure 77: Diagram of the body weight support system.....	102
Figure 78: The CAD Design of the CDLT.....	104
Figure 79: Inside the BWSD.....	104

List of Tables

Table 1: sagittal angular range of motion during flexion/extension motion trials[107].	42
Table 2: Local coordinates of the right Hip Joint Center using different algorithms.	45
Table 3: Inertia and length data [127].	53
Table 4: Dynamic simulation data	58
Table 5: The required workspace for planar CDPM example.	82
Table 6: Design parameters specifications for the planar CDPM example	83
Table 7: Feasible mechanical configurations for the planar CDPM example.	83
Table 8: The required workspace for spatial CDPM example.	85
Table 9: Design parameters specifications for spatial CDPM example.	85
Table 10 : New feasible configurations for the case of planar CDPM.	86
Table 11: Orientation and external wrench of a box $[b_0]$ centred at $(x,y)=(-0.14,0.46)$.	93
Table 12: Design parameters specifications.	95
Table 13: Maximum and average requirements of cable actuation system.	100
Table 14: Maximum and mean requirement for the servo motors.	101

Contribution to the development of an experimental device based on a robotic platform for gait rehabilitation

Abstract

This thesis focuses on the development of a gait training machine based on a Cable-Driven Parallel Manipulator. Persons suffering from neurological injuries such as Spinal Cord Injury and Stroke, may lose their motor functions including the ability to walk. These injured patients can relearn walking through intense and task-oriented rehabilitation therapy, which consists in simulating the gait movement. The proposed training machine is called the Cable-Driven Leg Trainer (CDLT). It includes a Body Weight Support Device to control the position of the trunk and a Cable-Driven Leg Manipulator to drive the lower limb during the walking movement. A gait analysis is carried out using an optical motion capture system and a force platform in order to get the kinematics and the dynamics of a normal gait. Using this information, an inverse dynamic study of a treadmill walking within the CDLT is achieved. Moreover, an algorithm of designing cable robots for a desired workspace using interval analysis is investigated. Interval analysis is a method used to provide a reliable computing, which guarantees a singularity free workspace. Using the developed models, a design study of the CDLT is conducted. All the actuation mechanisms of the CDLT are selected. Finally, a CAD model of the gait training machine is presented.

Key-words: Gait training, Cable-driven parallel manipulator, interval analysis, design optimization.

Contribution au Développement d'une Plateforme Robotisée pour le control et la rééducation fonctionnelle de la marche humaine

Résumé

Cette thèse porte sur le développement d'une machine de rééducation fonctionnelle de la marche humaine basée sur un robot parallèle à câbles. Les personnes atteintes par des troubles neurologiques tels que les traumatismes médullaires et les attaques cérébrales, peuvent perdre leurs fonctions motrices, y compris la capacité à marcher. Une rééducation intensive permet une récupération des aptitudes motrices de la marche, qui consiste à simuler le mouvement de la marche. La machine proposée comprend un système de décharge corporel pour contrôler la position du tronc et un robot à câbles pour entraîner le membre inférieur au cours du mouvement de la marche. Une analyse quantitative de la marche est réalisée à l'aide d'un système de capture de mouvement et une plate-forme de forces afin d'obtenir la cinématique et la dynamique d'une marche normale. En utilisant cette information, une étude dynamique inverse d'une marche au sein de la machine est effectuée. En outre, un algorithme pour la conception des robots à câbles pour un espace de travail désiré en utilisant l'analyse par intervalles est développé. L'analyse par intervalles est une méthode utilisée pour fournir des calculs fiables et qui garantit un espace sans singularité. En utilisant tous les résultats précédents, une étude de conception de la machine de rééducation est menée. Tous les mécanismes d'actionnement sont dimensionnés et des composants appropriés sont choisis. Finalement, un modèle CAO de la machine est présenté.

Mots-Clés: rééducation de la marche, robots parallèles à câbles, analyse par intervalles, optimisation de conception.